Improvement of critical current density in MgB2 by optimizing process parameters and chemical doping

Yun Zhang
University of Wollongong

Institute for Superconducting and Electronic Materials

Improvement of critical current density in MgB_2 by optimizing process parameters and chemical doping

Yun Zhang

This thesis is presented as part of the requirements for the award of the Degree of Doctor of Philosophy of the University of Wollongong

May 2009

DECLARATION

I, Yun Zhang, declare that this thesis, submitted in partial fulfillment of the requirements for the award of Doctor of Philosophy, in the Institute for Superconducting & Electronic Materials (ISEM), Faculty of Engineering, University of Wollongong, Australia, is wholly my own work unless otherwise referenced or acknowledged. This document has not been submitted for a qualification at any other academic institution.

Yun Zhang

May, 2008

ACKNOWLEDGEMENTS

I would like to express my deep gratitude to my supervisors, Prof. S. X. Dou and Dr. S. H. Zhou, for their continuous academic guidance, encouragement, and support during my PhD study in the Institute for Superconducting and Electronic Materials at the University of Wollongong.

I thank Dr. T. Silver for her kind help in proofreading and correcting the English in the manuscripts of my journal articles and this thesis.

I would also like to express my appreciation to Prof. H. K. Liu, Prof. X. L. Wang, A/Prof. A. V. Pan, Dr. J. Horvat, Dr. D. Q. Shi, Dr. Y. Zhao, Dr. Y. Zeng, and Dr. K. Konstantinov for their contributions to measurements and for useful discussions and valuable suggestions.

My special thanks to all my colleagues at ISEM including Mr. X. Xu, Mr. W. X. Li, and all the members and technicians at the Faculty of Engineering, especially Mr. R. Kinnell, Mr. G. Tillman, and Mr. N. Mackie, for their friendly help and assistance in using the facilities.

I would also like to acknowledge the University of Wollongong for providing my UPA scholarship and the Research Student Centre at the University of Wollongong, who managed my scholarship, for their enthusiastic support.

Finally I wish to thank my husband and my son for their patience and support. In particular, without my husband's encouragement, I really would not have been able to continue my academic work. My son was born at the very beginning of my PhD study, and he has made it easy to combine motherhood with my work.

ABSTRACT

The discovery of superconductivity in MgB_2 in January 2001 has triggered enormous interest around the world. MgB_2 has evolved as a promising superconductor for the next generation of superconductor applications, due to not only its higher critical temperature (T_c = 39 K), low material cost, and good weak-link tolerance, but also its rich multiple-band structure. However, several issues exist that urgently need to be solved, such as its low upper critical field (H_{c2}) and rapid decrease in critical current density (J_c) under magnetic field compared to Nb-based superconductors. High $J_c(H)$ performance is crucial for the application of this material in the so-called "strong electrical application" field. Therefore, the objective of this thesis is to increase J_c of bulk polycrystalline MgB_2 via studying the influence of the boron precursor powder and the nominal Mg/B mixing ratio and efforts to further enhance J_c by doping with two types of sources: carbon sources (such as SiC and sucrose) and oxygen sources (such as TiO_2/SiO_2 and processing atmospheres with different oxygen content).

The control of the boron powder is one of most promising methods to enhance J_c at high fields without significant decrease of the self-field J_c. The particle size, purity, and form of the starting boron powders play an important role in the superconducting properties of MgB_2. It has been proved the precursor B powder is very important to critical current density of MgB_2. In terms of the influence of boron precursor on the superconducting properties of MgB_2, J_c values for MgB_2 made from ball-milled high purity boron powders with crystalline phase are at least two times higher than for a comparable MgB_2 sample made from ball-milled amorphous boron powder and a factor of 40 higher

than typical values of standard MgB_2 samples. The possible mechanism proposed to account for this difference is H_{c2} enhancement caused by the increased disorder.

Nano-particle SiC is a very effective dopant to improve the in-field J_c of MgB_2. However, J_c at lower field become lower than the undoped one. It would be desirable to maintain a high low-field J_c while improve the high field J_c. In order to solve this issue, the influence of Mg content was investigated in a series of undoped and SiC-doped MgB_2 samples with systematic variation of the nominal Mg/B ratio (x:2). It has been found that in the undoped MgB_2 samples J_c increases with x to a maximum value at x = 1.1 and then decreases. The higher J_c at x = 1.1 is attributed to the better connectivity caused by smaller amounts of impurities. In the SiC-doped samples, it has been found that the sample with x = 1.15 exhibits the best J_c performance for all fields from 0 – 8.5 T, including the self-field, and its T_c is higher than for the sample with x = 1. The enhancement of J_c is attributed to the improved connectivity and the increased disorder. The optimized Mg/B ratio (1.15:2) also diminishes the interband scattering caused by the Mg or B vacancies and, in turn, increases T_c.

Carbonhydrates such as sucrose can decompose at high emperature. The resulting carbon from the decomposition can be used as carbon source to dope into MgB_2. This kind of carbon is very reactive and can be incorporated into MgB_2 easier. A comprehensive study of the effects of carbohydrate doping on the superconductivity of MgB_2 has been conducted. Doping with sucrose at varying rates and annealing temperatures results in an optimal J_c value in $MgB_{2-x}C_x$ at x = 0.2 and 850 ^oC. At 5 K and 6 T, the x = 0.2 sample shows one order of magnitude improvement compared to pure sample. It has been found that sucrose doping causes a small depression in T_c and

high resistivity, while H_{c2} performance is improved. The reason for the enhancement of H_{c2} is likely to be increased disorder caused by C substitution for B and/or diffusion of C atoms in the MgB_2 lattice as interstitial atoms.

TiO_2/SiO_2 additions lead to improved J_c values. J_c values are the highest at the doping ratio of 10 wt% at 5 K and 20 K, and at the doping ratio of 5 wt% at 30 K, when the sintering temperature is fixed at 750 ^oC. When the doping ratio is fixed at 5 wt%, the sample with the sintering temperature of 750 ^oC has the best J_c for 5 K and 20 K, while the sample with the sintering temperature of 850 ^oC exhibits the highest J_c at 30 K. In addition, it has been found that the addition of TiO_2/SiO_2 nanoparticles results in a small depression in T_c, while the H_{c2} and irreversibility field (H_{irr}) performances are improved. The enhancement of H_{c2} and H_{irr} can be attributed to the existence of precipitates induced by the TiO_2/SiO_2 doping.

The effect of processing atmosphere on microstructure and superconducting properties was studied for MgB_2 samples made using the *in situ* reaction technique under argon atmosphere with three different purities, ultra-high, high, and welding grade. The critical temperature, T_c, decreases by 0.5 K while the FWHM, the resistivity and the amount of MgO show an increase in the welding Ar processed sample. The J_c, H_{irr} and H_{c2} for the welding Ar processed sample are improved in comparison with the samples treated in ultra-high and high purity argon. Transmission electron microscope (TEM) examination revealed that the sample processed in welding grade argon possessed small grains, a high density of defects, and larger crystalline strains, which act as effective pinning centres. These results verify the dual reaction model where the MgB_2 formation and the reaction between oxygen and precursor take place simultaneously, resulting in

an optimal doping effect. The $J_c(H)$ behaviour for samples treated at 800^oC for 60 hours in the sealed Fe tube shows little difference among the three different Ar atmospheres. The optimal J_c and flux pinning properties in MgB_2 can be achieved by using readily available and economical welding grade Ar as the protective atmosphere instead of using ultra-high or high purity Ar. The effects of the sintering time on the superconductivity of MgB_2 with sintering in the welding grade Ar atmosphere have been investigated. The sample sintered for 30 min exhibits the highest J_c at high fields. The reason can be attributed to the improved connectivity and the increased H_{c2}.

Overall, the works in this thesis are mainly on material process and characterization. I have studied many factors such as precursor powder, process parameters, dopants that have strong effects on J_c. The results are useful for future MgB_2 fabrications.

TABLE OF CONTENTS

DECLARATION ii

ACKNOWLEDGEMENTS iii

ABSTRACT v

TABLE OF CONTENTS ix

LIST OF FIGURES xiii

LIST OF TABLES xviii

1. INTRODUCTION 1

1. 1 The History of superconductors 1

1. 2 Fundamental Phenomena of Superconductivity 3

1. 3 Brief review of theories on superconductivity 4

1. 4 Type I and type II superconductors 6

1. 5 Flux pinning mechanism in type-II superconductors 8

1. 6 Applications of superconducting materials 10

1.6.1 Low-T_c superconducting Materials 11

1.6.1 High-T_c Superconducting Materials 12

1. 7 Magnesium Diboride 12

1.7.1 Discovery and properties of MgB_2 13

1.7.2 Pairing mechanism and two gaps in MgB_2 14

1.7.3 Preparation of MgB_2 materials 15

1.7.4 Fabrication of MgB_2 17

1.7.5 Grain Connectivity 19

1.7.6 Chemical doping in MgB_2 19

1.7.7 Potential of MgB_2 for applications 23

1. 8 Aim and outline of the thesis 24

2 Experiments Procedures 27

2. 1 Equipments 27

2.1.1 Horizontal Tube furnance 27

2.1.2 Ball-milling machine 28

2.1.3 X-ray Diffractometry 29

2.1.4 Scanning Electron Microscopy and transmission electron microscopy 29

2.1.5 Magnetic properties measurement 31

2.1.6 Four-Point Transport Measurement 36

2.1.7 Raman spectroscopy 37

2. 2 Experiment procedures 38

3 Ball-milled boron precursor powders 41

3. 1 Influence of ball-milled crystalline boron precursor powders on T_c and J_c .. 42

3.1.1 Properties of boron precursor powders 42

3.1.2 Sample preparation 44

3.1.3 XRD Analysis 45

3.1.4 SEM observation 48

3.1.5 T_c and J_c 50

3. 2 Influence of different sintering temperatures 55

3.2.1 Sample preparation 55

3.2.2 XRD analysis 55

3.2.3 Resistivity Versus Temperature 58

3. 3 Summary 62

4 Norminal Mg/B mixing ratio 64

4. 1 Optimization of nominal Mg/B mixing ratio in pure MgB_2 65

4.1.1 Sample preparation 65
4.1.2 XRD analysis 66
4.1.3 T_c, resistivity and J_c 69
4. 2 Effect of nominal Mg/B mixing ratio in SiC-doped MgB_2 bulk..... 73
4.2.1 Sample preparation 73
4.2.2 XRD analysis 74
4.2.3 T_c and Raman spectra study 77
4.2.4 Resistivity and connectivity 81
4.2.5 SEM observation 82
4.2.6 H_{c2} and J_c 83
4. 3 Summary 88
5 Sucrose ($C_{12}H_{22}O_{11}$) doping 90
5. 1 Influence of carbon doping level 90
5.1.1 Sample preparation 90
5.1.2 Optimization of carbon doping level 91
5.1.3 Optimization of sintering temperature 93
5. 2 Analysis of H_{c2} and resistivity 95
5.2.1 Sample preparation 95
5.2.2 XRD analysis 96
5.2.3 Resistivity and H_{c2} 98
5. 3 Summary 103
6 Co-doping of Nano-sized TiO_2/SiO_2 Particles 104
6. 1 Sample preparation 104
6. 2 XRD analysis 105
6. 3 T_c and J_c 110

6. 4 Resistivity and H_{c2} 113

6. 5 Summary 115

7 Effect of Processing Atmosphere 117

7. 1 Optimal processing atmosphere 118

7.1.1 Sample preparation 118

7.1.2 Superconducting properties 119

7. 2 Optimal sintering time in MgB_2 bulk sintered in welding grade Ar 126

7.2.1 Sample preparation 126

7.2.2 XRD analysis 127

7. 3 Summary 133

8 Conclusions 135

REFERENCES 138

PUBLICATIONS 167

LIST OF FIGURES

Figure 1.1 Evolution of T_c with time 2

Figure 1.2 T_c-H_c-J_c plot showing the relationship of the three critical parameters of a superconductor 4

Figure 1.3 Magnetisation and resistivity as a function of applied magnetic field for (a) type I and (b) perfect type II superconductor at constant temperature below T_c 7

Figure 1.4 Vortex lattice in the mixed state of a type-II superconductor 8

Figure 1.5 The various markets in which superconductors are expected to make a contribution 11

Figure 1.6 Crystal structure of MgB_2 14

Figure 1.7 Values of the two gaps in MgB_2 extracted from the scanning tunnelling spectroscopy as a function of temperature 15

Figure 1.8 Transport J_c at 4.2 K in magnetic fields up to 18 T for 5 at.% C-doped MgB_2 tapers sinted at various temperatures. The J_c values of an undoped tape heated at 800^{o}C are also included as a standard 22

Figure 2.1 Horizontal tube furnance with gas end-caps includes vacuum system and atmosphere controlled apparatus 27

Figure 2.2 Schematic diagram of the heat treatment for the preparation of MgB_2 samples 28

Figure 2.3 Fritsch Pulverisette 7 ball-milling machine 29

Figure 2.4 The JOEL JSM-6460A Analytical SEM 30

Figure 2.5 Schematic illustration of beam's path through the column 31

Figure 2.6 Model 6000 Physical Property Measurement System (PPMS) 33

Figure 2.7 Magnetic property measurement system (MPMS) 34

Figure 2.8 Magnetic hysteresis loop showing the width of the magnetic hysteresis loop (ΔM) 36

Figure 2.9 The specialized sample puck for transport measurement 37

Figure 2.10 The HORIBA Jobin Yvon system 38

Figure 3.1 X-ray diffraction patterns for different starting boron powders 43

Figure 3.2 X-ray diffraction patterns (square symbols) and refined profiles (solid lines) for the three samples. The lowest trace in each panel shows the difference between the measured and refined profiles 45

Figure 3.3 FEG-SEM images of high-purity crystalline boron powder with/without ball-milling: low and high magnification images (a,c) of as-supplied crystalline boron powder and (b,d) crystalline boron powder after ball milling 49

Figure 3.4 FEG-SEM images of samples; Sample A; (b) Sample B; (c) Sample C . 50

Figure 3.5 Magnetic susceptibility as a function of temperature for the MgB_2 samples. The inset shows the critical temperature as a function of the *a*-axis lattice parameter 51

Figure 3.6 J_c curves for MgB_2 samples with different B powders 52

Figure 3.7 XRD patterns for the different samples 56

Figure 3.8 Resistivity versus temperature for the four samples 59

Figure 3.9 ρ_{40K} versus microstrain 60

Figure 3.10 T_c versus ρ_{norm} 60

Figure 3.11 Temperature dependence of H_{c2} 61

Figure 3.12 H_{c2} versus microstrain 62

Figure 4.1 Powder XRD traces of Mg_xB_2 samples with x = 0.9, 1, 1.1, 1.2, and 1.3 66

Figure 4.2 Magnetic susceptibility plotted against temperature 69

Figure 4.3 Resistivity versus temperature for the samples 71

Figure 4.4 Magnetic field dependence of critical current density in Mg_xB_2 at the temperatures of 5 K and 20 K 71

Figure 4.5 Self-field J_c at 20 K vs. A_F 73

Figure 4.6 H_{c2} at 20 K vs. microstrain 73

Figure 4.7 X-ray diffraction patterns for samples 75

Figure 4.8 Normalized Raman spectra with three-peak Gaussian fitting 79

Figure 4.9 ω_2 peak frequency against x 80

Figure 4.10 FEG-SEM images; a - sample A; b - sample B; c - sample C; d - sample D 83

Figure 4.11 Temperature dependence of H_{c2} 84

Figure 4.12 H_{c2} against average microstrain and $I_{\omega3}/I_{\omega2}$ 85

Figure 4.13 Critical current density $J_c(H)$ at 5 K and 20 K 86

Figure 4.14 J_c at 20 K and 5 T against α_1 (bottom panel) and J_c at 20 K and 0 T against α_2 (top panel) 88

Figure 5.1 Magnetic AC susceptibility for $MgB_{2-x}C_x$ as a function of temperature for different carbon doping content 91

Figure 5.2 J_c as a function of applied magnetic field for all sucrose-doped samples of $MgB_{2-x}C_x$ at 5 K and 20 K 92

Figure 5.3 Critical current density at 20 K and 4 T as a function of *x* 93

Figure 5.4 Magnetic AC susceptibility as a function of temperature for the pure MgB_2 and sucrose-doped $MgB_{1.8}C_{0.2}$ sintered at various temperatures 93

Figure 5.5 $J_c(H)$ curves for pure MgB_2 and sucrose-doped $MgB_{1.8}C_{0.2}$ sintered at various temperatures 95

Figure 5.6 Powder XRD patterns of sucrose-doped MgB_2 samples sintered at the temperatures of 850°C (sample A) and 1050°C (sample B). Undoped MgB_2 was sintered at 850°C as a reference. The inset shows an enlargement of the area containing the (002) and (110) MgB_2 peaks 96

Figure 5.7 SEM images of undoped (a) and sucrose-doped (b) MgB_2 samples 98

Figure 5.8 Resistivity as a function of temperature for the undoped and doped samples 99

Figure 5.9 ρ_{40K} vs. A_F (a), and T_c vs. ρ_{norm} (b) 100

Figure 5.10 Temperature dependence of normalized H_{c2} for the undoped and doped samples 101

Figure 5.11 H_{c2} vs. microstrain (a), and H_{c2} vs. lattice parameter *a* (b) 102

Figure 6.1 Powder XRD patterns of a doped sample (5wt% TiO_2) at various sintering temperatures 105

Figure 6.2 Powder XRD patterns of MgB_2 samples with various doping ratios sintered at 750°C 106

Figure 6.3 Lattice constants of the samples for various sintering temperatures and various doping ratios 108

Figure 6.4 Magnetic susceptibility plotted against temperature for various doping ratios (a) and various sintering temperatures (b) 110

Figure 6.5 T_c as a function of the average lattice constant 111

Figure 6.6 Magnetic field dependence of J_c at the temperatures of 5 K, 20 K, and 30 K for various doping ratios (a) and sintering temperatures (b) 112

Figure 6.7 Resistivities versus temperature for undoped and doped samples. An enlargement of the region around the critical temperature appears in the inset 114

Figure 6.8 Temperature dependence of normalized H_{irr} and H_{c2} for undoped and doped samples 114

Figure 7.1 The J_c – H dependence at 5 K and 20 K for MgB_2 pellet samples processed at 800^{o}C under three different Ar atmospheres in sealed Fe tube 120

Figure 7.2The the normalised J_c versus H at 20 K for MgB_2 pellet samples processed at 700^{o}C under three different Ar atmospheres: UA, HA and WA samples. The inset is the J_c – H curves at 5 K and 20 K for these three corresponding samples ... 121

Figure 7.3 The resistivity versus temperature for samples UA, HA and WA. The inset is the normalised resistivity to the room temperature resistivity versus temperature 122

Figure 7.4 The H_{irr} and H_{c2} curves determined from resistivity measurements for the samples, UA, HA and WA 123

Figure 7.5 FEG-SEM images for samples WA (a), HA (b) and UA (c) which were processed at 700 C for 30 min 124

Figure 7.6 TEM images from the samples HA (a) and WA (b), and the high resolution TEM images showing the high density of defects in the sample WA (c) and the lattice distortion in WA (d) 125

Figure 7.7 Powder XRD patterns of MgB_2 samples 128

Figure 7.8 Resistivity versus temperature 129

Figure 7.9 Temperature dependence of H_{c2} and H_{irr}. The inset shows the dependence of H_{c2} and H_{irr} on the microstrain 130

Figure 7.10 $J_c(H)$ curves at 5 K and 20 K for MgB_2 samples. The inset shows J_c at 20 K and 4.87 T as a function of $A_F \cdot H_{c2}$ for the three samples 131

Figure 7.11 FEG-SEM images for (a) sample A, (b) sample B, and (c) sample C .. 133

LIST OF TABLES

Table 1.1 Pinning forces for different pinnig centers 9

Table 1.2 List of superconducting parameters of MgB_2 13

Table 1.3 Comparison of magnetic and transport $J_c(H)$ at 4.2/5 K for different carbon doping sources. All the $J_c(H)$s were determined by the magnetization and 8 T unless stated 20

Table 1.4 Basic superconducting properties of the practical supercondors 24

Table 3.1 FWHM of indexed peaks of XRD patterns for two types of boron powders 43

Table 3.2 Calculated refinable parameters for the three samples 46

Table 3.3 Parameters and properties for all samples..... 57

Table 4.1 Refined parameters IN Mg_XB_2..... 67

Table 4.2 Magnetic susceptibility plotted against temperature..... 70

Table 4.3 Calculated refinable parameters..... 77

Table 4.4 Properties of samples 78

Table 5.1 Parameters and properties for all samples..... 97

Table 6.1 Weight fraction of each phase in the samples..... 107

Table 6.2 Resistivity properties 115

Table 7.1 Basic parameters of samples processed under different Ar atmospheres and 700^{o}C for 30 min..... 119

Table 7.2 Parameters for the three samples 128

1 Introduction

1.1 The History of Superconductors

Superconductivity is a phenomenon which occurs in certain materials and is characterized by the absence of electrical resistivity. It was first observed in mercury by Kamerlingh-Onnes in 1911 [1]. At the temperature of 4.19 K, he observed that the resistivity abruptly disappeared. Initially, Onnes called the phenomenon "*supraconductivity*" (1913). For this research, he was awarded the Nobel Prize in Physics in 1913. In the years to follow, many other metallic elements, alloys, and intermediate compounds were found to exhibit superconductivity with transition temperatures (T_c) of less than 23 K. However, in 1986, a higher T_c, above 30 K, was observed in the Ba-La-Cu-O system [2]. Following this, the Y-B-Cu-O system was reported for the first time to show a superconducting phase above 92 K, which is higher than the boiling point of liquid nitrogen [3]. In a short while, the Tl-Ba-Cu-O [4] and the Bi-Sr-Ca-Cu-O [5] systems were found to superconduct at 125 K and 110 K, respectively. Later on, Hg-Ba-Ca-Cu-O was also shown to be superconducting at 134 K [6]. It is believed that it is the quasi two-dimensional Cu-O layers that are the key to the origin of the high T_c values. In 2001, superconductivity at 39 K was discovered in magnesium diboride, MgB_2 [7]. Figure 1.1 shows the evolution of discoveries in the superconductor field. The discovery of superconductivity in MgB_2 has triggered

enormous interest around the world. MgB_2 has evolved as a promising superconductor for the next generation of superconductor applications, such

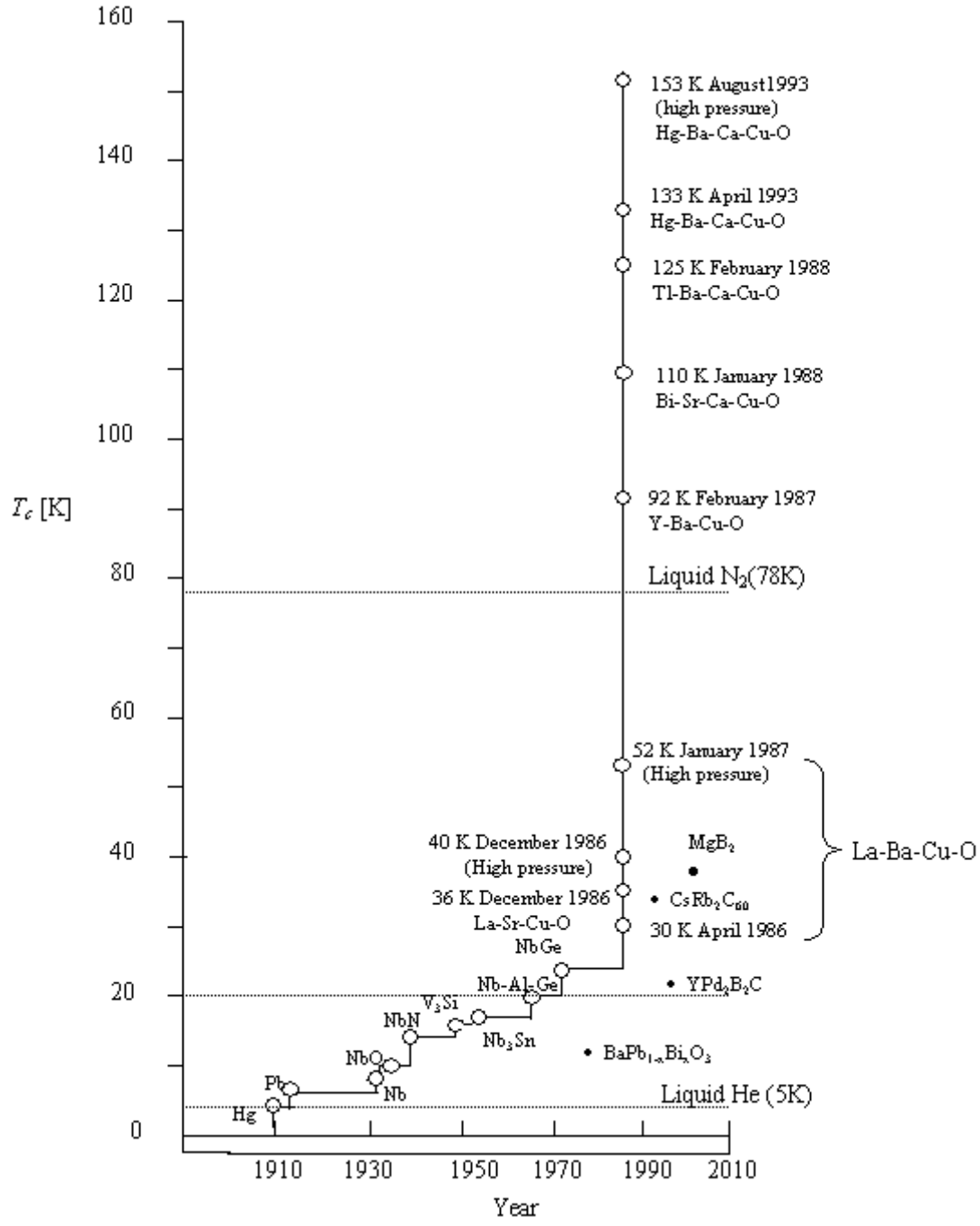

Figure 1.1 Evolution of T_c with time.

as in magnets, transformers, and electronic devices. Due to the T_c of 39 K, MgB_2 can be used in applications around the 20-25 K temperature range, above the range of current

low temperature superconductors (LTS; e.g., NbTi and Nb_3Sn). In this range, expensive liquid helium can be avoided, and more economical liquid hydrogen or cryocoolers can be used. MgB_2 also has a higher self-field critical current density (J_c) and a higher upper critical field (H_{c2}), after alloying, than NbTi and Nb_3Sn. High temperature superconductors (HTS), on the other hand, allow for a higher operating temperature. However, due to thermal instability, 20-25 K is generally regarded as the optimal operating temperature. In that sense, MgB_2 is attractive, because it avoids the limitations of HTS, including weak-links at grain boundaries, large anisotropy, high texture requirements, and high cost.

1.2 Fundamental Phenomena of Superconductivity

There are 3 important parameters for identification and applications of superconductors: the critical temperature, T_c, the critical magnetic field, H_c, and the critical current density, J_c. The temperature at which the transition from the normal to the superconducting state occurs is called the transition temperature, T_c. It is most notable because it results in perfect conduction of electricity. A superconductor also exhibits perfect diamagnetism when it is cooled below T_c in the presence of a relatively weak magnetic field. This effect, called the Meissner Effect [8], is a defining phenomenon of superconductivity. There exists a maximum magnetic field, i.e. the critical field, H_c, above which superconductivity disappears. However, a superconductor can only withstand a certain amount of current before losing its superconducting properties. This maximum current is called the critical current, I_c, and is often expressed in term of current per unit area, i.e. critical current density, J_c. H_c and T_c are intrinsic properties, whereas J_c is dependent upon extrinsic properties. The T_c, H_c, and J_c can be represented

in a three-dimensional critical space, as shown in Figure 1.2. Superconductivity can only be preserved below this surface.

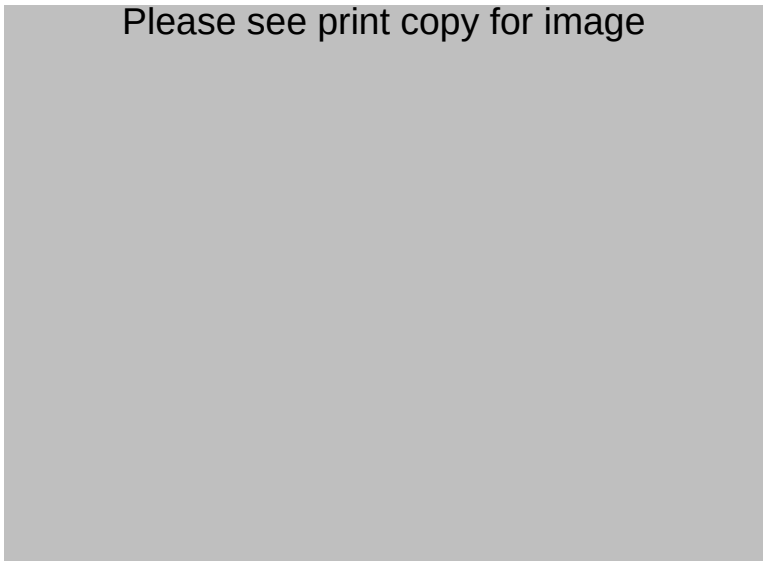

Figure 1.2 T_c-H_c-J_c plot showing the relationship of the three critical parameters of a superconductor[9].

1.3 Brief Review of Theories of Superconductivity

Following the discovery of the Meissner effect, this defining characteristic of superconductivity was explained by the brothers Fritz and Heinz London [10], who established that the flux density B(x) at a point at a distance x from the surface of the superconductor is given by

$$B(x) = B(0)\exp(-x/\lambda_L) \qquad (1.1)$$

where λ_L is the London penetration depth and B(0) is the flux density at the surface. The London penetration depth characterizes the typical distance to which a magnetic field penetrates into a superconductor. Typical values are between 50 and 500 nm. Deep inside a superconductor, the magnetic field is zero (Meissner effect). However, there are a number of superconductor properties which can not be explained by the London theory. The important assumptions made in the London theory, that the penetration depth λ_L is independent of both the strength of the applied magnetic field and the specimen dimensions, are not strictly true, especially in a strong magnetic field or for a sample having a high aspect ratio. In 1950, Ginzburg and Landau developed a phenomenological theory of superconductivity [11] which defines 2 parameters: a coherence length ξ and a penetration depth λ. In a perfectly pure superconductor, the coherence length is an intrinsic property of the material, denoted by ξ_0. If impurities are present, the coherence length is normally reduced. Thus, the actual coherence length in an impure material is written as ξ. The ratio $\kappa = \lambda/\xi$ is known as the Ginzburg–Landau parameter, which does not depend on temperature when close to T_c. In 1957, Bardeen, Cooper and Schrieffer (BCS) [12] showed that superconductivity could be well described by pairs of conduction electrons of opposite momenta coupling together through a weak attractive interaction. The pair interaction produces a gap, 2Δ, in the energy levels of the electrons and allows a net reduction in the free energy of the superconductor by forming electron pairs, known as Cooper pairs. The Frohlich [13] electron-phonon interaction provides a mechanism for attractive interaction between the electrons by coupling them through exchange of virtual phonons. The energy gap, 2Δ, varies with temperature, and above T_c, the gap goes to zero, and pairing is destroyed. The BCS theory has been successful in explaining essentially all of the phenomena

associated with the superconducting state, such as specific heat, critical fields, tunnelling, and others.

1.4 Type I and Type II Superconductors

Abrikosov [14] showed that the Ginzburg-Landau theory predicted two distinct behaviours for superconductors in an applied magnetic field (see Figure 1.3). According to the response to magnetic field, superconductors can be divided into 2 classes: type I superconductors and type II superconductors. $\kappa = 1/\sqrt{2}$ is the critical value separating the two classes. A superconductor is type I if $\kappa < 1/\sqrt{2}$, while it is type II if $\kappa > 1/\sqrt{2}$. κ is an increasing function of impurity concentration, so that the alloys always exhibit type II behavior. A type I superconductor exhibits a Meissner effect at fields below H_c. At fields greater than H_c, the type I superconductor reverts to the normal state and regains its normal state resistance. In a type II superconductor, the Meissner effect exists at fields below the lower critical field (H_{c1}). As the field is increased beyond H_{c1}, the penetration of magnetic flux becomes favourable, and quantized flux lines (vortices) are formed parallel to the applied field. When the field increases further, up to the upper critical field (H_{c2}), the superconductivity disappears. The region between H_{c1} and H_{c2} is called the mixed state. H_c in any type I superconductor is about 2000 Gauss (0.2 Tesla), but in type II materials, superconductivity can persist to several hundred thousand Gauss (H_{c2}).

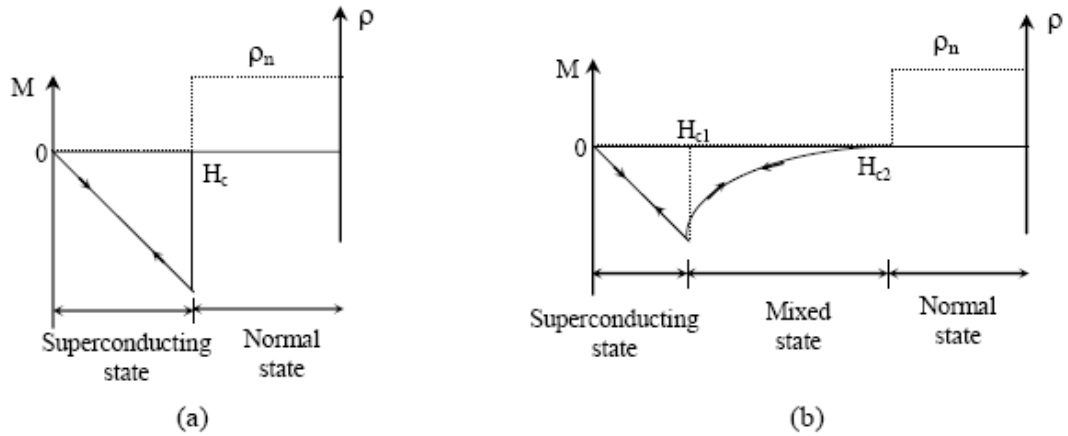

Figure 1.3 Magnetisation and resistivity as functions of applied magnetic field for (a) type I and (b) perfect type II superconductor at a constant temperature below T_c.

In the mixed state, vortices, consisting of a normal core with a flux quantum surrounded by a circulating supercurrent, are maintained by the circulation of the persistent current in a direction opposite to the surface screening current, generating a magnetic field in the opposite direction to the applied field, as depicted in Figure 1.4. The quantum of magnetic flux in a normal core is given by:

$$\Phi_0 = h/2e = 2.0678 \times 10^{-15} \text{ Weber} \qquad (1.2)$$

where h is Planck's constant and e the charge of an electron. The radius of the normal core is ξ. A vortex lattice is formed by the interactions among the vortices. With increasing flux density or temperature, the normal cores are packed more and more closely to each other and overlap eventually. At this point, superconductivity is lost, and the material is returned to the normal state.

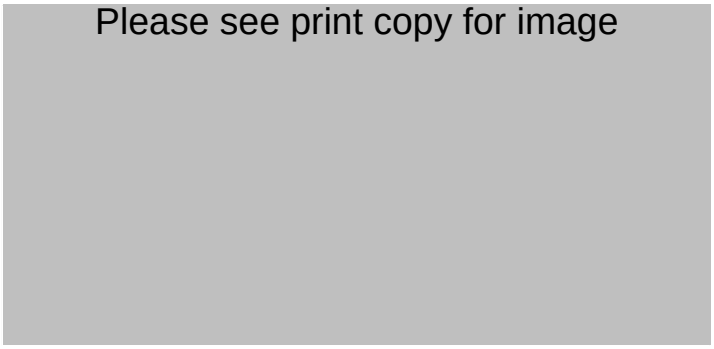

Figure 1.4 Vortex lattice in the mixed state of a type-II superconductor [15].

1.5 Flux Pinning Mechanism in Type-II Superconductors

In the mixed state of an ideal type II superconductor, the magnetization is completely reversible. In a hard superconductor, however, the presence of lattice defects pins the vortices. The vortices are no longer free to move, and the magnetization is highly irreversible. Therefore, the hard supercoductor can sustain a large amount of supercurrent. When the supercurrent reaches a certain critical density (J_c), the magnetization saturates. It have been deduced that J_c is limited by the Lorentz force [16]. J_c will be reached when the pinning force is balanced out by the Lorentz force. The relationship between J_c and the strength of the pinning force per unit volume (F_p) at an applied field (B) can be expressed by [17]

$$J_c(B) \times B = -F_p(B) \tag{1.3}$$

Dew-Hughes created an excellent model to calculate the pinning force (F_p) [18]. According to the Dew-Hughes's model, pinning centres can be classified by comparing the dimensions of the pinning centres with the inter-flux-line spacing (d). Point pins are regions whose dimensions in all directions are less than d, surface pins have two dimensions greater than d, while volume pins have all dimensions larger than d. d

decreases with increasing applied field (B) according to the relationship $d = 1.07(\varphi_0/B)^{1/2}$, where φ_0 is the superconducting flux quantum, $\varphi_0 \approx 2.07\times10^{-}15$ Wb. The pinning forces for different pinning centers, derived by Dew-Hughes, are listed in Table 1.1. $\Delta\kappa$ pinning corresponds to a small fluctuation in κ in the superconductor, arising from changes in the normal state resistivity, due to composition fluctuations or non-uniform distribution of dislocations. Normal pinning means that the pinning centers are non-superconducting particles.

A curve of the normalized volume pinning force F_p/F_{max} against the reduced magnetic field ($h = H/H_{c2}$ or $h = H/H_{irr}$) is often used to clarify the pinning mechanism. The Dew-Hughes model indicates that an expression $F_p/F_{max} = Ah^p(1-h)^q$ can be used to describe the relationship between F_p/F_{max} and h. Different values of p and q represents different pinning mechanisms. A is related to the size and distribution of the pinning centers. If p = 1 and q = 2 (or the peak of the curve is located at h = 0.33), the pinning mechanism is core normal point pinning; if p = 0.5 and q = 2 (or peak at h = 0.2), the pinning mechanism is core normal surface pinning; if p = 0 and q = 2 (no peak), the pinning mechanism is core normal volume pinning. The curve of p = 0.5 and q = 2 (or peak at h = 0.2) has the best fit to most experimental results of MgB_2. It has been concluded that surface pinning is the dominant pinning mechanism. Therefore, the grain boundaries are often considered as the most effective pinning centers in MgB_2 [19, 20].

Table 1.1 Pinning forces for different pinning centers [18].

Geometry of pin	Type of centre	Pinning force F_p
Volume	Normal	$\frac{\mu_0 S_V H_{c2}^2 (1-h)^2}{5.34\kappa^2}$

	$\Delta\kappa$	$\frac{\mu_0 S_V H_{c2}^2 h(1-h)\Delta\kappa}{2.67\kappa^3}$
Surface	Normal	$\frac{\mu_0 S_V H_{c2}^2 h^{1/2}(1-h)^2}{4\kappa^2}$
	$\Delta\kappa$	$\frac{\mu_0 S_V H_{c2}^2 h^{3/2}(1-h)\Delta\kappa}{2\kappa^3}$
Point	Normal	$\frac{\mu_0 V_f H_{c2}^2 h(1-h)^2}{4.64a\kappa^2}$
	$\Delta\kappa$	$\frac{\mu_0 V_f H_{c2}^2 h^2(1-h)\Delta\kappa}{2.32a\kappa^3}$

where $h = H/H_{c2}$, H is the applied field, S_v is the surface area per unit volume projected in the direction of the Lorentz force, V_f is the volume fraction of the superconductor, and a is the average dimension of pins.

1.6 Applications of Superconducting Materials

According to June 2002 estimates by the Conectus Consortium, the worldwide market for superconductor products is projected to grow to near US $5 billion by the year 2010 and to US $38 billion by 2020. Figure 1.5 [21] gives a rough outline of the various markets in which superconductors are expected to make a contribution.

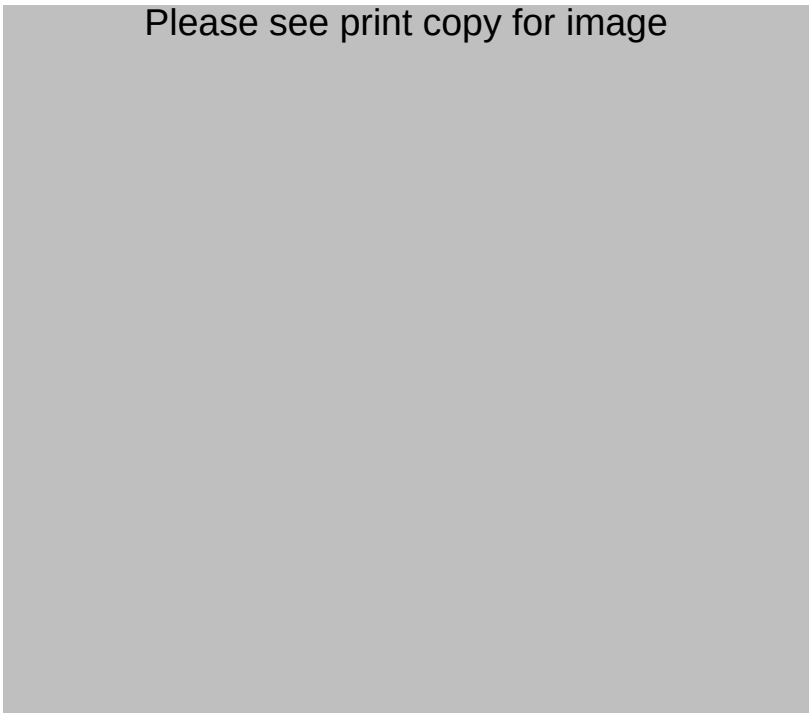

Figure 1.5 The various markets in which superconductors are expected to make a contribution [21].

1.6.1 Low-T_c Superconducting Materials

The low-temperature superconductors (LTS), in particular NbTi and Nb_3Sn, which have T_c of 9 K and 18 K, respectively, [22] have been the materials of choice for large-scale applications since the 1960s. Examples include magnetic resonance imaging (MRI), nuclear magnetic resonance (NMR), and magnets for high-energy physics accelerators and plasma fusion devices. NbTi is widely used in low field applications such as MRI instruments, and Nb_3Sn is used in high field applications such as NMR. NbTi-based superconductors, in which the Ti content varies from 46 to 50 wt%, are ductile, have high strength, and are easy to make into wires [23]. NbTi has $T_c \approx 9$ K [22], H_{c2}(4.2 K) $\approx 10 - 12$ T [24, 25], and very high J_c of more than 3×10^5 A cm^{-2} at 5 T, 4.2 K and 1.5×10^5 A cm^{-2} at 4.2 K, 8 T [26]. J_c can be improved significantly by chemical doping

with elements such as Fe and Ta [27, 28]. NbTi cannot be used for fields above 9 T because its thermal stability is reduced by the low T_c, even though its advantages, such as high strength, ductility, high J_c, and relatively low cost, are obvious [23].

Nb_3Sn is a brittle material, quite sensitive to strain, and not easy to make into wires. Multifilamentary Nb_3Sn is thus expensive and difficult to wind, and hence these magnets cost more than NbTi magnets. Nb_3Sn has a T_c of 18 K [22], H_{c2} of 23–29 T at 4.2 K [29-32], and high critical current density of 3×10^5 A cm^{-2} at 12 T and 4.2 K [33, 34]. The high energy physics research community, the NMR magnet industry, and fusion projects are the main customers for Nb_3Sn conductors.

1.6.2 High-T_c Superconducting Materials

The high-temperature superconductors (HTS), which were discovered in the late 1980s, have high T_c and H_{c2} values compared to the LTS materials. The most important and commercially interesting HTS are BSCCO (Bi-2223 and Bi-2212) and YBCO (Y123) [23]. Bi-2223 has a T_c of 110 K [5] , Bi-2212 has a T_c of ~ 85 K [5], and the T_c of YBCO is ~ 92 K [3]. Superconductors made from HTS materials are known as first-generation HTS wires or conductors, which are principally directed at electric power applications [35]. However, there are several disadvantages, such as high anisotropy, poor field performance at high temperatures, and weakly connected grain boundaries, that hinder practical applications.

1.7 Magnesium Diboride

1.7.1 Discovery and Properties of MgB_2

MgB_2 compound was first synthesised in 1954 [36], but only in 2001 was superconductivity at 39 K discovered by the Akitmitsu group [7]. Up to the present, MgB_2 has the highest T_c among the intermetallic superconductors. A list of the superconducting parameters of MgB_2 is presented in Table 1.2 [37]. MgB_2 has an AlB_2-type hexagonal structure [7], and the structural arrangement can be described as an alternate stacking of boron honeycomb planes and magnesium triangular planes, as shown in Figure 1.6. The structure of MgB_2 is held together by covalent B-B and ionic B-Mg bonding. The crystal structure of MgB_2 remains hexagonal under high pressure. The lattice parameters and *c*/*a* ratio are decreased monotonically by applying pressure up to 40 GPa, with no structural transitions [38]. The anisotropy in the bonding of MgB_2 corresponds to differences in the bond strengths; the B-B bonds are more rigid than the Mg-B bonds.

Table 1.2 List of superconducting parameters of MgB_2 [37].

Parameter	**Values**
Critical temperature	T_c = 39 - 40 K
Hexagonal Lattice Parameters	a = 0.3086 nm
	c = 0.3524 nm
Theoretical density	ρ = 2.55 g cm^{-3}
Resistivity near Tc	$\rho_{(40\ K)}$ = 0.4 - 16 $\mu\Omega$ cm
Upper critical field	$H_{c2} \parallel ab$ (0) = 14 - 39 T
	$H_{c2} \parallel c$ (0) = 2 - 24 T
Lower critical field	H_{c1} (0) = 27 - 48 mT
Irreversibility field	H_{irr} (0) = 6 -35 T
Coherence lengths	ξ_{ab} (0) = 3.7 -12 nm
	ξ_c (0) = 1.6 - 3.6 nm
Penetration depths	λ(0) = 85 -180 nm
Energy gap	Δ(0) = 1.8 -7.5 meV

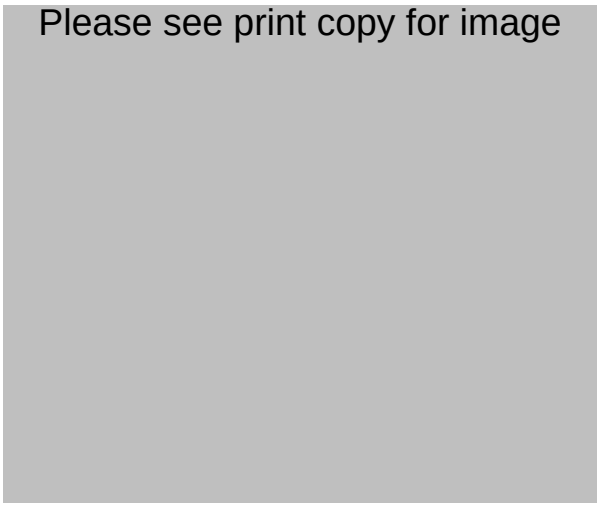

Figure 1.6 Crystal structure of MgB_2 [7].

1.7.2. Pairing Mechanism and Two Gaps in MgB_2

MgB_2 is a conventional phonon-mediated BCS superconductor [37], i.e. it becomes superconducting when electrons form Cooper pairs via the electron-phonon interaction. The most direct evidence for a phonon-mediated mechanism is the isotope effect, in which T_c decreases when the isotopic mass of the superconductor increases [39]. However, MgB_2 is by no means an ordinary superconductor. The boron honeycomb layer dominates the electronic structure, which is derived from σ bonding within the hexagonal boron planes to form the 2-D σ band and from the π bonding orbitals, which extend both in-plane and out-of-plane to form the 3-D π band. This partially covalent structure of the MgB_2 crystal gives rise to the Fermi surface with its two σ and π conduction bands. The two gaps arise from the existence of the two bands, the σ and π bands of the boron electrons [40]. Normally in a superconductor below T_c, there exists one temperature-dependent energy gap $\Delta(T)$ such that a minimum energy of $2\Delta(T)$ is needed to break a Cooper pair into two quasiparticles [39]. Two such gaps exist in MgB_2, one with $\Delta(0) \approx 2$ meV and another with $\Delta(0) \approx 7$ meV [41, 42]. The values of

the two gaps extracted from scanning tunnelling spectroscopy are plotted as function sof temperature in Figure 1.7 [43].

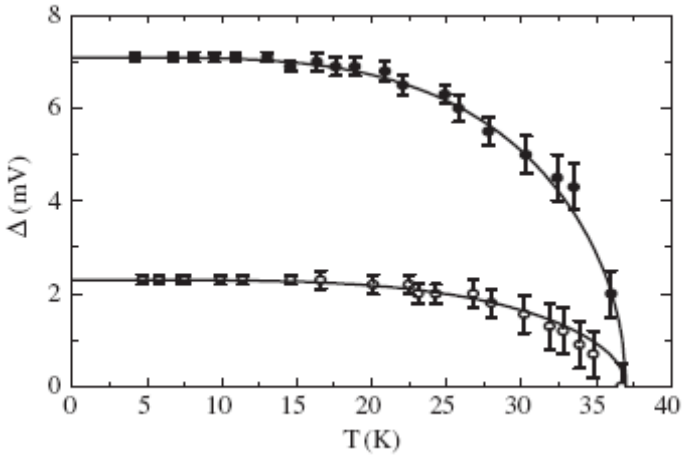

Figure 1.7 Values of the two gaps in MgB_2 extracted from scanning tunnelling spectroscopy as a function of temperature.

1.7.3. Preparation of MgB_2 materials

(a) The purity and non-stoichiometry of the starting powder

High purity starting powders play very important roles in the superconducting properties of MgB_2, such as J_c and T_c. Higher J_c and T_c can be obtained by using high purity starting powders. In commercial MgB_2, the impurities include MgO and MgB_4 [44-46], which may dirty the grains and grain boundaries. Therefore, there are different qualities of commercial MgB_2 powders available from suppliers such as Alfa Aesar. In *in-situ* reacted MgB_2, the starting powders of Mg or B are also contaminated with oxygen, in forms such as MgO impurity in commercial Mg powder [47] and B_2O_3

impurity in boron powder. Impurities such as Si, C, metal impurities [48-50], and H_3BO_3 [51] can also be found.

In general, the wires fabricated from commercial MgB_2 powder have lower J_c compared to *in-situ* reacted MgB_2 wires [52, 53]. However, higher J_c can also be obtained by using commercial MgB_2 powder reduced to a smaller particle size by ball milling [54]. This improvement may be explained by the smaller MgB_2 grains, which increase grain boundary pinning. Variation of T_c of ~ 1 K has been observed in a wide range of samples synthesised using different boron forms and purities [49, 50, 55]. The greater reactivity of amorphous boron powder compared to the crystalline form and a smaller particle size of B [50] or Mg [47] enhance the reaction rate, hence enhancing J_c due to increased superconducting volume of MgB_2 and more grain boundary pinning.

In addition, the nominal Mg/B mixing ratio in the starting powder could be another key factor leading to increased J_c. Mg deficiency will always occur during annealing due to the low melting point of magnesium (650°C) and its high vapor pressure. In fact, the existence of secondary phases such as MgO or MgB_4 [48, 49, 56, 57] can imply Mg deficiency in MgB_2 samples. Phase separation between Mg-vacancy rich (non-superconducting) and Mg-vacancy poor (superconducting) regions in Mg deficient samples has been observed [58, 59]. The amount of Mg vacancies varies depending on sample preparation conditions (1 - 10% Mg vacancy) [48, 57, 60, 61].

(b) Reaction conditions

In order to reduce the MgO impurity content, it is necessary for the synthesis of MgB_2 to be conducted in an inert gas atmosphere or in vacuum. Ar gas is one of the choices for gas

protection during synthesis of MgB_2. According to the different purities, there are three commercial grades of Ar gas, that is, ultra-high purity Ar, high purity Ar, and welding grade Ar. Even under ultra-high purity Ar protection, the formation of MgO is inevitable due to very small amounts of residual oxygen that are present in the gas. In addition, some starting powders are already oxidised during production and storage. At the melting point of Mg, an extremely low oxygen partial pressure of 10^{-60} atm is required to prevent the formation of MgO, and this may vary in the range of $10^{-50} – 10^{-25}$ atm at higher annealing temperatures of 900°C – 1400°C [62]. At ambient atmosphere, the melting point of Mg (650^{o}C) is much lower than that of B (2076^{o}C). Therefore, annealing below and above 650^{o}C will lead to solid-solid and liquid-solid reactions, respectively. The latter yields larger grain sizes than the former due to grain growth at the higher annealing temperature [63, 64].

1.7.4 Fabrication of MgB_2

(a) Preparation of bulk MgB_2

Preparation of bulk MgB_2 is significantly critical for research progress in this material. Polycrystalline samples of MgB_2 are prepared through the conventional solid state reaction using the reaction *in-situ* [48-50] and *ex-situ* processes [44-46]. For *in-situ*, the precursor powders are weighed out according to the nominal atomic ratio and well mixed through grinding with a mortar and pestle. The powders are pressed into pellets using a uniaxial hydraulic press. The pellets are sealed in Fe tubes, and then sintered at different temperatures, ranging from 600^{o}C to 1000^{o}C [65]. A wide range of sintering times have been used, from a few minutes to a few hours, most commonly 30 min. Heat treatment is carried out in flowing Ar under ambient pressure using a tube furnace. This is followed by a furnace cooling to room temperature. For *ex-situ*, the commercial

MgB_2 powder acts as the precursor powder, followed by similar steps to the *in-situ* process mentioned above.

(b) Preparation of wire and tape MgB_2

Powder-in-tube (PIT) process. Preparing and developing superconducting wires and tapes is essential for practical applications such as applications in the cable and magnet industries. The first MgB_2 wire was fabricated by Canfield *et al.* [66] via magnesium vapour infiltration into tungsten-core boron filaments. However, for practical applications, a conductive and malleable sheath is required to provide cryogenic stabilisation and structural support. MgB_2 is a relatively tough and hard phase, and so cannot easily be plastically deformed. Therefore, the best way to obtain a filamentary configuration is to start with powders that are packed in metallic tubes by a method known as the powder-in-tube process (PIT). The PIT process remains one of the most promising and commonly used techniques for the development of low-cost MgB_2 conductors [67, 68]. The procedure mainly consists of three steps: preparing the precursor powder and packing the powder into a metal tube, a mechanical deformation process to make the green wire or tape, and heat treatment. There are excellent review articles on the properties of MgB_2 wires and tapes [69, 70].

(c) Effects of the sheath material

Using the proper metal as a sheath material has been found to be critical in preparing high performance MgB_2. A number of sheath materials have been used: iron [54, 70-84], copper [67, 69, 81, 85-94], silver [67, 95], nickel [96-98], niobium [68, 99], and

tantalum [68, 100]. In addition multi-layers of metals or metallic alloys, such as stainless steel (SS) [101-103], carbon steel (CS) [85], NbZr [78], Cu/Ni [85, 104], and Cu/Ta [105, 106] have been reported by many groups. Iron is so far the most suitable sheath and has only 1-3 μm of interface layer at temperatures below 850°C, but the layer can increase up to 30 μm at 1100°C [107].

1.7.5 Grain Connectivity

Compared to the HTS superconductors [108, 109], MgB_2 does not show any weak links, therefore grain boundaries are highly transparent to current flow [110, 111]. However, formation of oxide phases such as BO_x and MgO at the grain boundaries leads to increased resistivity [112]. The thickness of the BO_x layers is around 2 nm [113], which means that they could act as Josephson junctions, and the size of MgO particles can vary between 10 nm and 500 nm [114]. Such oxide phases or other defects in the grain will also decrease the electron mean free path, resulting in increased intragrain resistivity. The grain connectivity can be further worsened by voids due to the high volatility of Mg. The obtained sample density is normally around half of the theoretical density or less, even in some doped samples [115]. By compacting the sample by using hot isostatic pressing (HIP) [116-118] and high pressure sintering [119, 120], J_c can be increased as a result of enhanced grain connectivity or flux pinning by defects. In addition, Muranaka *et al*. [121] showed that J_c is also increased systematically by increased sample density resulting in improved grain connectivity.

1.7.6. Chemical doping in MgB_2

There are several aims for chemical doping into MgB_2. First of all, element substitution for Mg or B is the key aim, from which changes in the electronic state, lattice parameters, and crystallinity are expected to occur. Secondly, inclusions of impurity particles with relatively small grain size are expected to be effective pinning sites. Finally, chemical doping is expected to suppress the grain growth of MgB_2.

(a) Metal doping

With a view to substitution for Mg in MgB_2, many types of metal dopants, such as Al [122], Ti [123], and Zr [124] have been reported to form metal borides having the AlB_2 structure. So far, only Al substitution on Mg sites has been confirmed [122]. Berenov *et al.* have successfully improved the J_c at lower fields at 20 K, while T_c remained unchanged. Ti [123, 125] and Zr [124] do not substitute into the MgB_2 phase but change the sample microstructure dramatically, forming thin TiB_2 or ZrB_2 layers instead.

(b) Carbon source doping

In terms of substitution for B in MgB_2, compared with Be, O, F, and Si [121], carbon is the most effective dopant for improving H_{irr} and J_c. Carbon doping can be easily performed by the addition of B_4C [126-128], carbon [129-135], carbon nanotubes [136-145], nanodiamonds [145, 146], NbC [147], SiC [47, 101, 115, 127, 129, 136, 143, 148-172], or organic compounds [163, 173-177]. A comparison of magnetic and transport $J_c(H)$ at 4.2/5 K and 8 T for different carbon doping sources is shown in Table 1.3.

SiC doping. So far, SiC is the most popular dopant because the carbon can not only significantly enhance J_c in high fields with only a small depression in T_c [178], but be doped into MgB_2 at low temperatures (600°C) [129]. Soltanian *et al. [151]* found that compared to samples sintered at higher temperature, SiC doped samples sintered at a lower temperature have a very fine and firm grain structure. It is believed that a relatively low sintering temperature results in a higher concentration of impurity precipitates, larger resistivity, higher J_c, and lower T_c values. It is the huge local strains produced by nanoprecipitates and the grain boundary structure that is the dominant mechanism responsible for higher H_{c2} near T_c. However, there is different dominant mechanism for higher H_{c2} in the low temperature zone when samples are sintered at higher temperature, that is, higher impurity scattering due to carbon substitution.

Table 1.3 Comparison of $J_c(H)$ at 4.2/5 K for different carbon doping sources. All the $J_c(H)$s were determined by the magnetization, and measurements were at 8 T unless otherwise stated.

Carbon source	Type	Reference	J_c at 4.2/5 K (A/cm^2)	Reaction/substitution temperature
SiC	Bulk	[115]	2.5×10^4	Low T
	Wire	[115]	Transport 4.1×10^4	
	Tape/Fe	[101, 168]	Transport 3×10^4	
	Tape/Fe	[47]	Transport 6×10^4	
	Tape/Fe	[179]	2×10^4	
	Strand (1 m)	[170]	Transport 2×10^5	
Carbohydrates	$C_4H_6O_6$ Bulk	[174]	1×10^4	
	Sugar Bulk	[180]	1.5×10^4	
	$C_{18}H_{36}O_2$ Wire/Fe	[173]	Transport 3×10^4 (9 T)	
	$C_4H_2O_3$ Wire/Fe	[181]	Transport 2×10^4	
	$C_4H_4O_4$ Tape/Fe	[182]	Transport 8×10^3 (9 T)	
Hydrocarbon	$C_{16}H_{10}$ Wire/Fe	[183]	Transport 2×10^4	

	C_6H_6 Tape/Fe	[177]	Transport 3.2 x 10^4	
B_4C	Bulk	[184]	> 8 x10^5 (2 T)	High T
	Bulk	[126, 185]	2 x10^5 (2 T)	
C	Bulk	[186]	3 x 10^3	
	Bulk	[187]	7 x 10^4	
	Tape/Fe	[134]	Transport 4.4 x 10^4	
CNT	Wire/Fe	[142, 188, 189]	1 x 10^4	
	Wire/Fe	[136]	1.2 x 10^4 (7 T)	

Carbohydrate and hydrocarbon doping. Carbohydrates and hydrocarbons are the other types of C source from which carbon can be doped into MgB_2 at low temperatures [177, 190, 191]. The merits of carbohydrate and hydrocarbon doping are obvious. For example, compared to the nanoscale materials, these kinds of materials are much cheaper, and the agglomeration of particles caused by doping with undissolved materials can be avoided. A uniform structure can also be achieved because they dissolve and decompose at low temperatures. On the other hand, disadvantages of organic species also exist. For example, the liquid state hydrocarbons, such as benzene, ethyl toluene, thiophene, etc., are not suitable because of the difficulty in controlling the exact carbon content, and also because of the toxicity [177]. Moreover, adding oxygen-rich carbohydrates risks introducing more MgO impurity, which may enhance the vortex pinning, but also strongly degrades the connectivity.

Nano-carbon and carbon nanotube (CNT) doping. Higher processing temperatures are necessary for most of the other carbon sources besides SiC and organic species, which leads to grain growth and worse pinning. However, comparable results were also obtained with nanoscale carbon powder [132] and carbon nanotubes [144]. Carbon sources which do not induce secondary phases seem to be favourable in principle,

because any precipitates potentially decrease the connectivity [192]. It should be noted that the reported substitutions at boron sites are effective for improving critical current properties at high magnetic fields, whereas substitutions at magnesium sites are effective in enhancing J_c at low magnetic fields only [121]. Many groups that have studied the effects of carbon doping on MgB_2 have shown that low annealing temperatures and short sintering times result in an incomplete reaction and hence lower carbon solubility in MgB_2. Ma *et al*. [132] investigated the effect of nanoscale C doping on J_c and B_{irr} of Fe-sheathed MgB_2 tapes with different sintering temperature from 600°C to 950°C, as shown in Figure 1.8. They found that the J_c values of doped samples increased systematically with increasing sintering temperatures. Their tape sintered at 950°C revealed the highest J_c values: at 4.2 K, the transport J_c reached 2.11×10^4 A cm^{-2} at 10 T. Kim *et al*. [144] studied the doping effects of single-walled and multi-walled carbon nanotubes on the T_c, lattice parameters, J_c, microstructure, and H_{c2} of MgB_2/Fe wire. They found that the J_c in 12 T and 4.2 K for their single-walled carbon nanotube doped wire sintered at 900°C increased by a factor of 35 compared to that of the undoped wire.

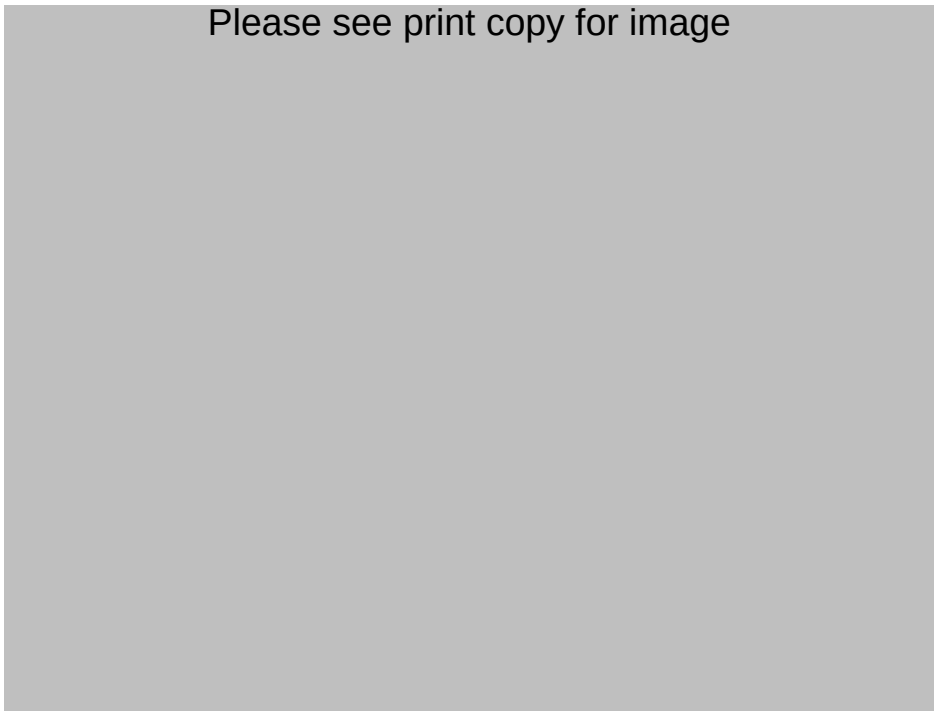

Figure 1.8 Transport J_c at 4.2 K in magnetic fields up to 18 T for 5 at% C-doped MgB_2 tapes sintered at various temperatures. The J_c values of an undoped tape sintered at 800^{o}C are also included as a standard [132].

Other compound doping. Besides the element substitution for Mg or B, other types of compound doping which are aimed at introducing effective pinning sites or suppressing the grain growth of MgB_2 have been widely reported. These compounds include oxides such as MgO [46, 193, 194], Al_2O_3 [195, 196], Fe_2O_3 [197], SiO_2 [101, 198], TiO_2 [199], ZrO_2 [200], Y_2O_3 [201], Fe_3O_4 [202], and Dy_2O_3 [203], silicides such as WSi_2 [149, 204], $ZrSi_2$ [149, 204], and Mg_2Si [149], Bi-2212 [205], Nb_xB_2 [206], ZrB_2 [204], and Mg_2Cu [207].

1.7.7 Potential of MgB_2 for applications

MgB_2 is a promising superconductor for high magnetic field applications [24, 208, 209]. Unlike high-T_c superconductors, where J_c drops sharply across the grain boundaries, grain boundaries in MgB_2 do not significantly degrade J_c and even serve as pinning centers [110, 210]. Doping or alloying with carbon or SiC have been shown to significantly enhance H_{c2} [211] and pinning [212]. On the economic side, MgB_2 conductors also benefit from the low raw material costs of both B and Mg, which will be several times less than those of Nb-based superconductors, even for materials of appropriate purity [209]. Also, the T_c at 39 K allows practical operation above 20 K using cryocoolers, while Nb-based superconductors have to be cooled to 4.2 K [213, 214]. MgB_2 devices and circuits can be operated above 20 K, and a 20 K cooler requires much less input power, is much lighter, and costs much less than a 4 K cooler

with the same cooling power [215]. Thus, the next generation MRI instruments must be made of MgB_2 coils instead of NbTi coils, operating in the 20 – 25 K range without liquid helium for cooling. In addition, other MgB_2 devices such as bolometers and neutron detectors have also been explored [216]. In fact MgB_2 has potential as the next generation high field magnetic material and as a strong competitor for the currently used NbTi and Nb_3Sn conductors. Besides the magnet applications, MgB_2 conductors have potential uses in superconducting transformers, rotors, and transmission cables at temperatures of around 25 K, at fields of 1 T. The basic MgB_2 superconducting properties are listed in Table 1.4 and compared to the LTS, NbTi and Nb_3Sn, and the HTS, Bi2223 and YBCO [23].

Table 1.4 Basic superconducting properties of the practical superconductors [23].

Material	T_c (K)	Anisotropy	Critical current density at 4.2 K J_c (A cm^{-2})	H_{c2} at 4.2 K (T)	H_{irr} at 4.2 K (T)	Coherence Length, ξ(O) (nm)	Penetration depth λ(O) (nm)
NbTi	9	Negligible	~10^6	11-12	10-11	4-5	240
Nb_3Sn	18	Negligible	~10^6	25-29	21-24	3	65
MgB_2	39	1.5-5	~10^6	15-20	6-12	4-5	100-140
Bi2223	110	50-200	~10^7	>100	0.2 (77 K)	1.5	150
YBCO	92	5-7	~10^6	>100	5-7 (77 K)	1.5	150

1.8 Aim and outline of the thesis

Although MgB_2 exhibits higher critical temperature (T_c = 39 K) compared to the LTS, low material cost, good weak-link tolerance, and has a rich multiple-band structure, several issues still exist that urgently need to be solved, such as its low H_{c2} and rapid decrease in J_c under magnetic field compared to Nb-based superconductors. High $J_c(H)$

performance is crucial for the application of this material in the so called "strong electrical application" field. Therefore, the aim of this thesis is to increase J_c of bulk polycrystalline MgB_2 via studying the influence of the boron precursor powder and the nominal Mg/B mixing ratio, and to further enhance J_c of the MgB_2 superconductor by doping with two sources: a carbon source (such as SiC or sucrose) and an oxygen source (such as TiO_2/SiO_2 or different amounts of oxygen introduced from the processing atmosphere).

The outline of the thesis is as follow:

1) Chapter 1 reviews the history and basic theories of superconductivity and the research on MgB_2.
2) Chapter 2 introduces the equipment and experimental procedures used in this thesis.
3) Chapter 3 investigates the effect of ball-milled boron precursor powder on the superconducting properties of MgB_2.
4) Chapter 4 investigates the effects of the nominal Mg/B mixing ratio on the superconducting properties of undoped and SiC-doped MgB_2.
5) Chapter 5 investigates the effects of sucrose doping on the superconducting properties of MgB_2.
6) Chapter 6 investigates the effects of co-doping with TiO_2/SiO_2 on the superconducting properties of MgB_2.
7) Chapter 7 investigates the effects of the oxygen processing atmosphere on the superconducting properties of MgB_2.
8) Chapter 8 contains the conclusions.

Based on the research in this thesis, 10 first-authored journal papers and one first-authored conference paper have been published or accepted.

2 Experimental Procedures

This chapter introduces the equipment used to fabricate the samples and examine the magnetic and microstructural properties, and the experimental procedures themselves.

2.1 Equipment

2.1.1 Horizontal tube furnace

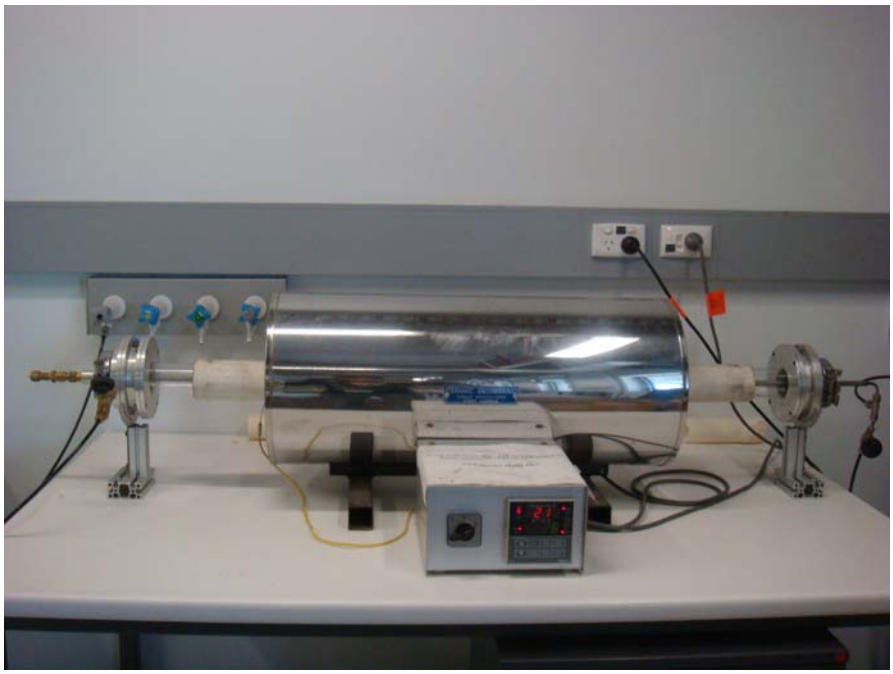

Figure 2.1 Horizontal tube furnace with gas end-caps includes vacuum system and controlled atmosphere apparatus.

A horizontal tube furnace was used to heat-treat MgB_2 samples. Our tube furnace (as shown in Figure 2.1) with gas end-caps includes a vacuum system and controlled atmosphere apparatus. Its length is ~ 700 mm, and the heated length is ~ 640 mm. The maximum temperature is 1100°C. A temperature profile for the preparation of MgB_2 bulk samples is shown in Figure 2.2.

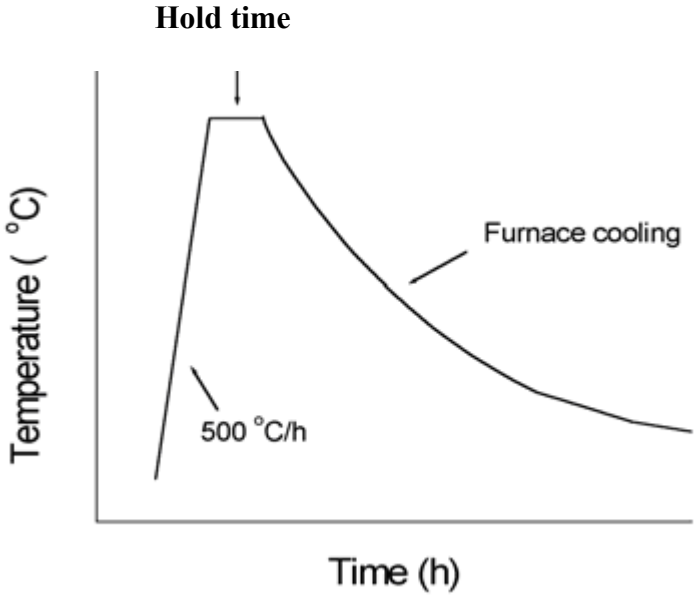

Figure 2.2 Schematic diagram of the heat treatment for the preparation of MgB_2 samples.

2.1.2 Ball-milling machine

The ball-milling machine used is a Fritsch Pulverisette 7, as shown in Figure 2.3. During the milling the sample is placed inside a grinding bowl along with the grinding balls. The grinding bowls are fastened onto the so-called sundial and counter-rotated around the centre of this disk. By beating, crushing, and grinding, the sample is effectively comminuted. The maximum possible speed is approximately 1100 rpm. The grinding duration down to the nanoscale also is drastically reduced.

Figure 2.3 Fritsch Pulverisette 7 ball-milling machine.

2.1.3 X-ray diffractometry

X-ray diffraction (XRD) was used to examine the microstructure, phase formation, weight fraction of each phase, lattice constants of MgB_2, grain size, and microstrain. The two XRD instruments used in this thesis were a Philips PW1730 model diffractometer using Cu Kα radiation with a wavelength of 1.541838 Å and an MAC MO3XHF model diffractometer using Cu Kα radiation with a wavelength of 1.5405 Å.

2.1.4 Scanning electron microscopy and transmission electron microscopy

Scanning electron microscope images were obtained from a JOEL JSM-6460A Analytical Scanning Electron Microscope (SEM) (Figure 2.4) and a high resolution JOEL JSM-7500FA field emission gun SEM (FEG-SEM). Figure 2.5 shows the beam's path through the electron gun column under SEM operation. The former of these instruments observes specimen at magnifications from 5 to 300,000 with a resolution of 3 nm under an accelerating voltage from 0 to 30 kilovolts. The latter observes specimens at magnifications up to 1,000,000× with a resolution of 1 nm. To obtain better imaging, samples were coated with gold.

Figure 2.4 The JOEL JSM-6460A Analytical SEM.

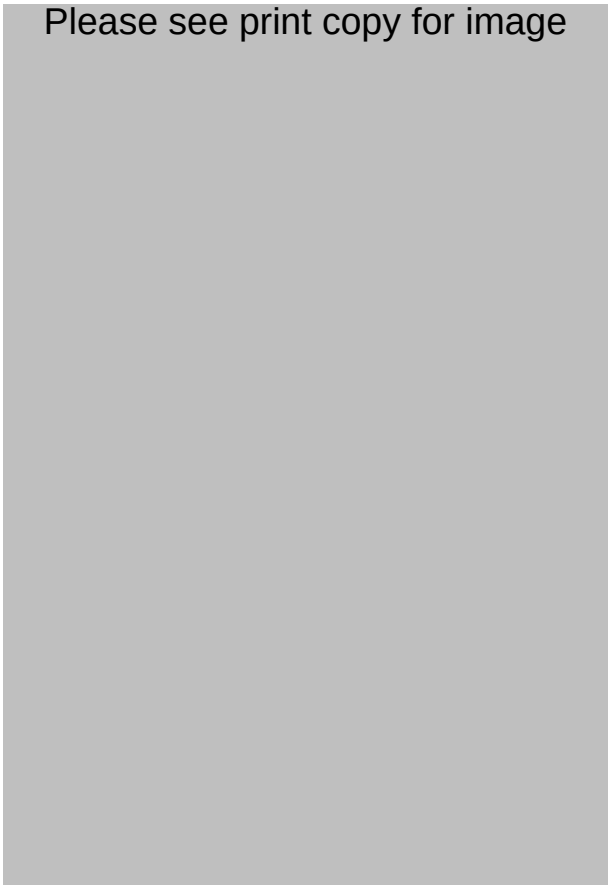

Figure 2.5 Schematic illustration of the beam's path through the column [217].

Transmission electron microscopy studies were conducted by Dr. X. Z. Liao at the School of Aerospace, Mechanical & Mechatronic Engineering, University of Sydney. At the University of Sydney, a JEOL 3000F high resolution transmission electron microscope (HRTEM) was used. The samples were prepared by mechanical grinding followed by Ar ion milling of the MgB_2 pellets. In order to minimise damage to the sample, it was kept cold in a liquid nitrogen cooled stage, as well as being protected by using a low sputtering angle and a low ion milling current/voltage.

2.1.5 Magnetic properties measurement

(a) Physical properties measurement system

The Physical Properties Measurement System (PPMS) is a type of laboratory equipment that can be adapted to measure T_c, J_c, H_{c2}, and the irreversibility field, H_{irr}. The model 6000 PPMS shown in Figure 2.6 has the following features:

- Large (one-inch bore) sample chamber
- Front-panel control or Windows™-based software
- Interchangeable sample holders with 12 pre-installed electrical leads
- Nitrogen-jacketed dewar option, which reduces typical helium consumption by up to 30 % over non-jacketed dewars
- The size of the transverse magnet system is ± 7 Tesla
- The size of the longitudinal magnet system is ± 9 Tesla, and the resolution is 0.3 Oe to 1 Tesla, 3.0 Oe to 9 Tesla
- The temperature control range is from 1.9 to 400 Kelvin with an accuracy of ± 0.5 %
- AC susceptibility frequency range: 10 Hz to 10 kHz, field amplitude: 2 mOe to 15 Oe, sensitivity: 2 x 10^{-8} emu at 10 kHz
- DC magnetization sensitivity: 2.5 x 10^{-5} emu

Figure 2.6 Model 6000 Physical Properties Measurement System (PPMS).

(b) Magnetic properties measurement system

The magnetic properties measurement system (MPMS) is specified for experimental and materials characterization tasks that require the highest detection sensitivities over a broad temperature range and in applied magnetic fields to seven Tesla. The MPMS is designed to be a primary research tool in the complicated study of magnetism in matter. The magnetic signature of a material reflects its intrinsic spin and orbital angular momentum. The model 6000 MPMS shown in Figure 2.7 has the following features:

- Temperature control system is precise, with control of the sample temperature in the range of 2 K (-271^{o}C) to 400 K (127^{o}C). This requires controlling the heat flow into the sample space and the active control of gas to provide cooling power.

- Magnet control system: current from a power supply is set to provide magnetic fields from 0 T to ±7 T. The magnet can be operated in either persistent or non-persistent modes, and several charging options can be selected.
- Superconducting SQUID amplifier system: the SQUID detector is the heart of the magnetic moment detection system. It provides reset circuitry, auto-ranging capability, a highly balanced second-derivative sample coil array, and electromagnetic interference (EMI) protection.

Figure 2.7 Magnetic properties measurement system (MPMS).

- Sample handling system: the ability to step and rotate the sample smoothly through the detection coils without transmitting undue mechanical vibration to the SQUID is of primary importance. This facility allows for varied scan lengths and options as to how data are acquired for a given measurement.

- Computer operating system: all operating features of the MPMS are under automated computer control. The user interface at the PC console provides the option of working under standard sequence controls or diagnostic controls which will invoke individual functions.

(c) AC susceptibility

MgB_2 is well characterized by the combination of AC susceptibility (ACS) and DC magnetization in terms of its electromagnetic properties. In the AC susceptibility measurements, the sample will be located in a system consisting of primary and secondary coils. The primary coils produce an excitation field set to an amplitude of 0.1 Oe and a frequency of 117 Hz. The sample is placed in the secondary pick-up coils, where the change of the induction voltage across the coils due to the superconducting shielding current can be detected by the lock-in amplifier.

(d) DC magnetization measurements

DC magnetization measurements are carried out on MgB_2 samples using the PPMS and MPMS. In order to measure the absolute value of the DC magnetization, a DC field is applied to the sample, and the sample is moved through the entire detection coil. The pick-up coil detects a waveform signal versus the position of the sample. The DC magnetization is then extracted by fitting the detected signal with the known waveform signal. The magnetic J_c is derived from the half-width of the magnetization difference between the descending branch (M^+) and ascending branch (M^-) of the magnetization loop (Figure 2.8), using the following critical state model formula: $J_c = k\Delta M/d$**,** where k

= 12w/(3w-d) is a geometrical factor and $\Delta M = (|M^+| + |M^-|)/2/V_{l\times w\times d}$, with l, d and w being the sample length, thickness, and width, respectively, that determine the sample volume V.

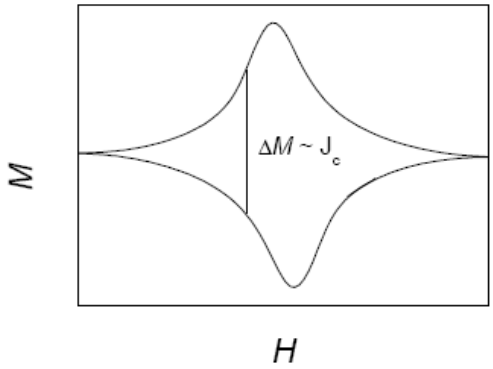

Figure 2.8 Magnetic hysteresis loop with the width ΔM indicated.

2.1.6 Four-point transport measurement

Transport measurements of MgB_2 samples are carried out using the so-called four probe technique. This method consists of attaching four contacts to the sample. The two outermost contacts are for the current (I), and the two inner contacts are for the voltage (V), as shown in Figure 2.9. This specialized sample puck connects to a 12-pin connector pre-wired to the system electronics in the sample chamber. As the current passes through the sample, a voltage is generated which is proportional to the resistivity. At the normal-superconducting transition, the voltage drops down to a level which is lower than the noise level of the measuring instrument. In the case of critical current (I_c) measurements, the standard value of 1 μV/cm is used as a criterion for I_c. Therefore, I_c is arbitrarily defined as the value of the current which produces a voltage drop of 1 μV

between two voltage contacts separated by 1 cm. Contacts between the wires and sample are made using silver paste in order to make low resistance contacts.

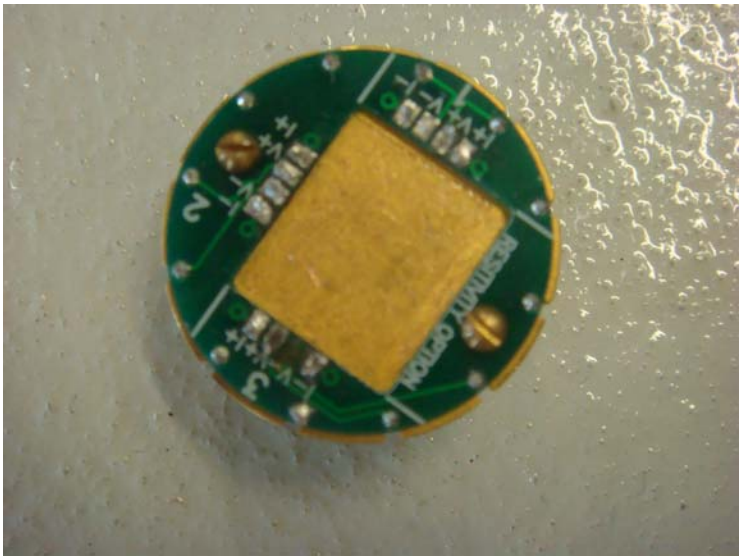

Figure 2.9 The specialized sample puck for transport measurements.

2.1.7 Raman spectroscopy

Raman spectroscopy is a vibrational technique for identification and analysis of molecular species. It is one of the fastest growing techniques in molecular spectroscopy. Raman spectroscopy is based on the detection and processing of the scattered radiation produced by a molecule when it is irradiated with a monochromatic laser light. Raman measurements are carried out using a HORIBA Jobin Yvon system in this work, as shown in Figure 2.10. The Raman scattering is measured at ambient temperature by a confocal laser Raman spectrometer with a 100× microscope. A 632.8 nm wavelength Ar+ laser is used for excitation. The system is calibrated with a standard SiO_2 single crystal before measurement. Several spots are selected on the same sample to collect the Raman signals in order to make sure that the results are consistent.

Figure 2.10 The HORIBA Jobin Yvon system.

2.2 Experimental Procedures

This section gives a brief decription of the experimental procedures which were used to prepare MgB_2 samples and examine their supercoducting properties and microstructural properties. More details will be explained in the individual chapters.

If necessary, the boron precursor powders are ball-milled first. Toluene is used as the ball-milling medium because it can prevent the oxidation of boron powder during the ball-milling process and there are no apparent substitution effects. The ball-milling process is normally carried out for 4 h with a rotation speed of 160 rpm under air. MgB_2 pellets are prepared by a solid-state reaction. Boron powders are mixed according to designed mixing ratios, ground, and pressed with magnesium powders. In some cases, dopants are added into the precursor powders. All samples are sintered at a set

temperature for a predetermined period. The heating rate is controllable. All MgB_2 materials are processed in a protective atmosphere such as Ar.

Magnetic measurements are conducted in PPMS and MPMS. Magnetic hysteresis loops are measured at various temperatures in fields up to 9 Tesla. The critical current density is calculated from the magnetization hysteresis loops, based on the dimensions of the samples. H_{c1} is measured at the field from which the magnetic hysteresis curve starts to deviate from linearity. The magnetic susceptibility as a function of temperature is measured in an applied field of H = 1 Oe for zero field cooled samples. T_c is defined as the temperature corresponding to the onset of diamagnetism, and the transition width (ΔT_c) is defined as the temperature variation between 10% and 90% of the full drop in the magnetic susceptibility. The resistivity is recorded as a function of temperature and magnetic field, using a four probe resistance technique. The connectivity (A_F) is estimated from the equation, $A_F = \Delta\rho_{ideal}/(\rho_{300K}-\rho_{40K})$, using the measured resistivity as a function of temperature. ρ_{40K} and ρ_{300K} are the resistivities at 40 K and 300 K, respectively. $\Delta\rho_{ideal}$ is the ideal change in resistivity from 300 K to 40 K for a fully connected sample. The normalized resistivity ρ_{norm} is calculated by $\rho_{norm}= \rho_{40K}/(\rho_{300K} - \rho_{40K})$. H_{c2} and H_{irr} are obtained from the respective fields at 90% and 10% of the normal state resistivity.

The Raman scattering is measured at ambient temperature by a confocal laser Raman spectrometer (HORIBA Jobin Yvon) with a 100× microscope. A 632.8 nm wavelength Ar+ laser is used for excitation, with the laser power maintained at about 20 mW. Several spots are selected on the same sample to collect the Raman signals in order to make sure that the results are consistent.

All samples are characterized by XRD. The XRD patterns are collected over a 2θ range from 20° to 80° with a step of 0.01° and a scanning speed of 0.5^{o}/min. The scanning is performed twice. The Rietveld refinement method is then performed to analyse the XRD measurements. The refinable parameters include the weight fraction of each phase (MgB_2, MgO, and so on), the lattice constants of MgB_2, the grain size, and the microstrain. FEG-SEM is used to observe the morphology of the agglomerates and pores in the MgB_2 samples. HRTEM is adopted to characterize grain morphology and locations of intra- and inter-granular impurities.

3 Ball-milled Boron Precursor Powders

The control of the boron powder is one of most promising methods to enhance J_c at high fields without significant decrease of the self-field J_c [55, 218-220]. The particle size, purity, and form of the starting boron powders play an important role in the superconducting properties of MgB_2. Ribeiro *et al.* found that there was a monotonic improvement in the critical temperature (T_c) from 38 K to 39 K as the boron purity was increased from 98% to 99.99% [49, 221]. Xu and his co-workers used both ball-milled low-purity crystalline boron powders [222] and ball-milled high-purity amorphous boron powders [176]. The estimated J_c was found to be 5×10^3 A/cm^2 at 8 T and 5 K in the latter. The improved performance was attributed to the small grain size and better reactivity induced by the small ball-milled boron particles. Chen *et al.* have also reported on the influence of the purity and form of the boron precursor on J_c of MgB_2 [50]. They used as-supplied boron powders. They found that using high-purity boron powder led to a high J_c and that samples made from crystalline boron powders had around an order of magnitude lower J_c than samples made from amorphous precursors. To further improve the J_c, it is necessary to determine the optimized combination of the particle size, purity, and form of the precursor boron powders. The use of high-purity boron powders with crystalline phase in combination with ball milling might be an effective method to not only overcome the poor reactivity of crystalline boron, but also introduce small grain size and high density, resulting in strong flux pinning and good connectivity of the MgB_2. In this work, we used high-purity (99.999%) crystalline boron

powder processed by ball-milling as one of the starting powders in order to produce "clean" MgB_2 with small grain size.

In Section 3.1 a systematic study of the grain size, microstrain, density, lattice parameters, phase fractions, J_c, and T_c of samples made from ball-milled crystalline boron are presented in comparison with MgB_2 samples made from as-supplied and ball-milled high purity amorphous boron powders. At 5 K and 8 T, the J_c value was 9.1×10^3 Acm^{-2}, which is two times higher than for the sample with ball-milled amorphous boron powders, and a factor of 40 higher than for the sample made from as-supplied amorphous boron powders. This result is also higher than for most doped samples, except for SiC and carbon-nanotube (CNT) doped samples [223, 224].

In Section 3.2, the effect of the sintering temperature on the transport properties and the critical current density in the samples made from ball-milled boron powders is investigated. A systematic study based on x-ray diffraction (XRD) analysis and on measurements of resistivity and H_{c2} is presented in comparison with MgB_2 reference samples made from as-supplied high-purity crystalline boron powder.

3.1 Influence of ball-milled crystalline boron precursor powders on T_c and J_c [225]

3.1.1 Properties of boron precursor powders

Figure 3.1 shows the XRD patterns of crystalline boron precursor powders with/without ball milling and of amorphous boron precursor powder. As expected, crystalline boron

powders without ball milling have a crystalline structure with space group $R\bar{3}m$. After ball milling, the crystalline phase still remains in the powders. Broadening of the peaks can be observed in the ball-milled crystalline boron powders. The full widths at half maximum (FWHMs) are shown in Table 3.1.

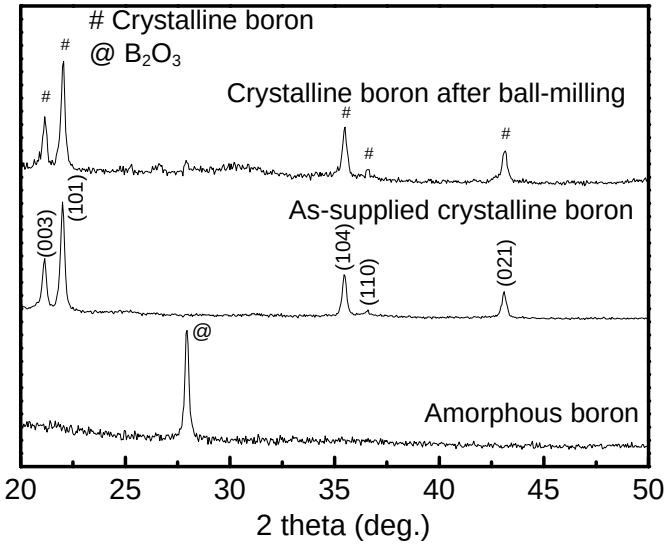

Figure 3.1 X-ray diffraction patterns for different starting boron powders.

Table 3.1 FWHM of indexed peaks of XRD patterns for two types of boron powders.

Powders	FWHM (degrees)			
	(003)	(101)	(104)	(021)
Boron with ball-milling	0.415	0.25	0.335	0.345
Boron without ball-milling	0.28	0.245	0.26	0.315

FWHMs of the indexed peaks (003), (101), (104), and (021) are increased from 0.28º, 0.245º, 0.26º, and 0.315º to 0.415º, 0.25º, 0.335º, and 0.345º, respectively, after ball milling. This indicates that the boron crystals have become smaller and/or they have higher microstrain after ball milling. In addition, the obvious irregular background in the trace of the ball-milled crystalline boron powder demonstrates that nanosized crystals

are present to some extent. Since the ball milling process does not significantly affect the XRD patterns of the amorphous powders, only as-supplied amorphous boron powders are shown in Figure 3.1. The trace exhibits the characteristics of typical amorphous phase, and a B_2O_3 peak appears. B_2O_3 may have been introduced during fabrication of the amorphous powders. A high B_2O_3 peak does not mean a large amount of oxygen, since the measurement was conducted for low-intensity amorphous powder. However, compared with the crystalline powders shown in Figure 3.1, without any measurable boron oxide, it can be concluded that the amorphous boron powder contains more oxygen than the crystalline boron powder.

3.1.2 Sample preparation

As-supplied amorphous boron powders (99%) and as-supplied crystalline boron powders (99.999%) were ball-milled with toluene. Toluene was used as the ball-milling medium because it can prevent the oxidation of boron powder during the ball milling process and there are no apparent substitution effects [176]. The ball-milling process was carried out over 4 h with a rotation speed of 160 rpm under air. MgB_2 pellets were prepared by a solid-state reaction. Boron powders were stoichiometrically mixed, ground, and pressed with magnesium (99%) powder. All samples were sintered at the temperature of 650^{o}C for 30 min under high-purity argon gas. The heating rate was 5^{o}C per minute. MgB_2 samples made from as-supplied amorphous boron powders were also fabricated for comparison by applying the same process. The samples made from as-supplied amorphous B powders, ball-milled amorphous boron powders, and ball-milled crystalline boron powders are termed samples A, B, and C in Section 3.1, respectively.

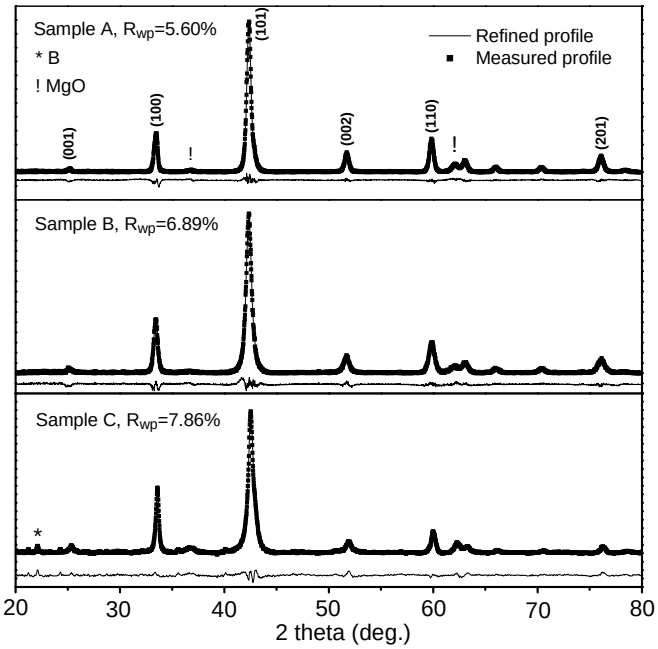

Figure 3.2 X-ray diffraction patterns (square symbols) and refined profiles (solid lines) for the three samples. The lowest trace in each panel shows the difference between the measured and refined profiles.

3.1.3 XRD Analysis

The XRD patterns for MgB_2 samples with different boron powders are represented in Figure 3.2 by solid square symbols. All samples seem to be well developed MgB_2 with some MgO impurity. In sample C, a peak of un-reacted crystalline boron at $2\theta \approx 22.1^{o}$ can be observed, although the amount is very small. The starting boron and magnesium powders were stoichiometrically mixed. The formation of MgO by the reaction of boron powder and oxygen trapped in the sealed tube and in the starting boron powders results in insufficient magnesium to react with the boron and the residual crystalline boron in sample C. Crystalline boron peaks can not be observed for samples A and B due to the amorphous nature of the boron precursor powders. However, it is believed that there

should be a small amount of amorphous boron present in samples A and B for the same reason as in sample C.

The Rietveld refinement method was performed to analyse the XRD measurements, using the Reflex modules in the MS Modeling software package. The refinable parameters include the weight fraction of each phase, the lattice constants of MgB_2, grain size, and microstrain. Since the amount of remnant boron in the samples was small, boron was not taken into account in the refinement. The refined curves are shown in Figure 3.2 by solid lines. The lower curve in each panel of Figure 3.2 represents the difference between the measured profile and the refined profile. A measure of similarity (R_{wp}) between the measured diffraction pattern and the refined diffraction pattern is also shown in Figure 3.2. A low R_{wp} indicates good agreement between the measured and calculated data. R_{wp}s for samples A, B, and C are 5.6%, 6.89%, and 7.86%, respectively. These low values indicate that the refined results are acceptable.

Table 3.2 Calculated refinable parameters for the three samples.

	Sample A	Sample B	Sample C
Weight fraction of MgB_2 (%)	92.98	94.91	88.74
Weight fraction of MgO (%)	7.02	5.09	11.26
Lattice parameter *a* (Å)	3.087	3.084	3.086
Lattice parameter *c* (Å)	3.530	3.526	3.523
Grain size along *a*-axis (nm)	244.0	78.3	89.3
Grain size along *c*-axis (nm)	150.6	36.7	28.9
Average grain size (nm)	197.3	57.5	59.1
Microstrain along *a*-axis (%)	0.101	0.099	0.288
Microstrain along *c*-axis (%)	0.148	0.280	0.661
Average microstrain (%)	0.125	0.190	0.475

The calculated refinable parameters are shown in Table 3.2. Sample B from ball-milled amorphous boron powders has the smallest fraction of MgO, while sample C from ball-milled crystalline boron powders exhibits the largest amount of MgO. The fraction of MgO in sample A from the as-supplied amorphous boron powders is between the above two values. It can be seen from the XRD traces shown in Figure 3.1 that the amorphous boron powders have a relatively larger amount of oxygen than the crystalline boron powders. However, less MgO exists in samples A and B than in sample C. Ref. [50] reported that 99.99% amorphous boron powders resulted in less MgO impurity than 99% crystalline boron powders. They explained that the size of the precursor powders affects the fraction of impurities that are formed. In our case, crystalline boron powder and amorphous boron powder have a similar size after ball-milling. Combining our results and the observations in Ref. [50] demonstrates that the form of the precursor powders may also significantly influence the reaction of boron and magnesium. The amorphous boron powders can rapidly react with the magnesium powders, while the reaction between the crystalline boron powders and magnesium powders is slower. Therefore, there is more MgO impurity in sample C. Comparing the MgO fractions in samples A and B shows that the particle size plays an important role in the reaction of magnesium and boron. A smaller particle size enhances the reaction. It allows MgB_2 to be formed at a lower sintering temperature. These observations are consistent with those in Refs. [50, 222].

Lattice parameters *a* and *c* in all the samples are greater than the ideal values (a = 3.083 Å and c = 3.521 Å). This indicates that a large amount of vacancies exist in the samples. A deficiency of magnesium atoms in the MgB_2 samples due to the formation of MgO could be responsible for the vacancies. Sample A has the largest *a* parameter and the

largest *c* parameter. Sample B exhibits the smallest *a* parameter, while sample C has the smallest *c* parameter.

The grain sizes and microstrains along the two lattice axes (*a* and *c*) were also evaluated. The average values were obtained by arithmetically averaging the values along the two lattice axes. The grain size along the *a*-axis is greater than that along the *c*-axis for all three samples. Samples B and C have similar average grain sizes, which are smaller than that of sample A. This can be attributed to the ball-milling processes for samples B and C. The microstrains in the samples also exhibit anisotropic behaviour, namely, the microstrain along the *c*-axis is larger than that along the *a*-axis. The ratios of the microstrain along the *a*-axis to the microstrain along the *c*-axis are 1.47, 2.83, and 2.3 for samples A, B and C, respectively. The anisotropic microstrain is caused by the anisotropic elastic modulus along the different axes. A smaller elastic modulus along the *c*-axis results in a larger strain [226]. The average microstrain increases from sample A to sample B, and then to sample C.

3.1.4 SEM observations

FEG-SEM images of the as-supplied boron powder and ball-milled boron powder are shown in Figure 3.3(a)-(d). Figure 3.3(a) and (c) contains low magnification and high magnification images for the as-supplied boron powder, while Figure 3.3(b) and (d) shows low magnification and high magnification images for the ball-milled boron powder, respectively. It can be observed that the particles of the as-supplied crystalline powder are larger than those of the ball-milled one (~100-200nm). FWHMs of the indexed peaks of the XRD patterns for both boron powders are shown in Table 3.1. The

ball-milled boron powder exhibits larger FWHMs than the as-supplied boron powder. A larger FWHM in general indicates a small particle size in the material. This is consistent with the SEM observations.

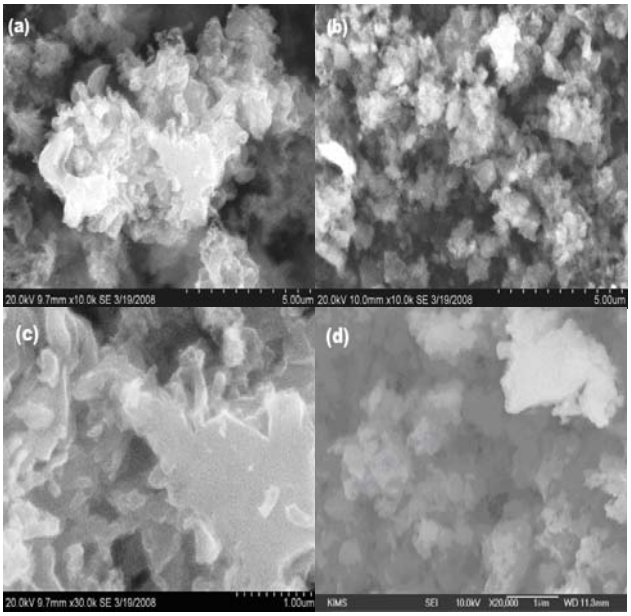

Figure 3.3 FEG-SEM images of high-purity crystalline boron powder with/without ball-milling: low and high magnification images of (a,c) as-supplied crystalline boron powder and (b,d) crystalline boron powder after ball milling.

Figure 3.4 shows FEG-SEM images of samples A, B, and C. The pores can be observed in all the samples. It can be seen from Figure 3.4 that sample C is denser than samples A and B, which is consistent with the density measurements (1.19 g/cm^3, 1.18 g/cm^3, and 1.35 g/cm^3 for samples A, B, and C, respectively). This indicates that sample C has better connectivity than samples A and B. Image analysis software (Image-Pro Plus) was used to quantitatively determine the average particle sizes in the three images. The measured particle sizes are 202 nm, 112 nm, and 108 nm for samples A, B, and C, respectively. The particle size of sample A is close to the grain size determined by the

XRD refinement method, while the particle sizes in samples B and C are larger than the grain sizes measured by the XRD refinement method. This indicates that the particles of sample A consist of single crystals, while the particles of samples B and C are agglomerates.

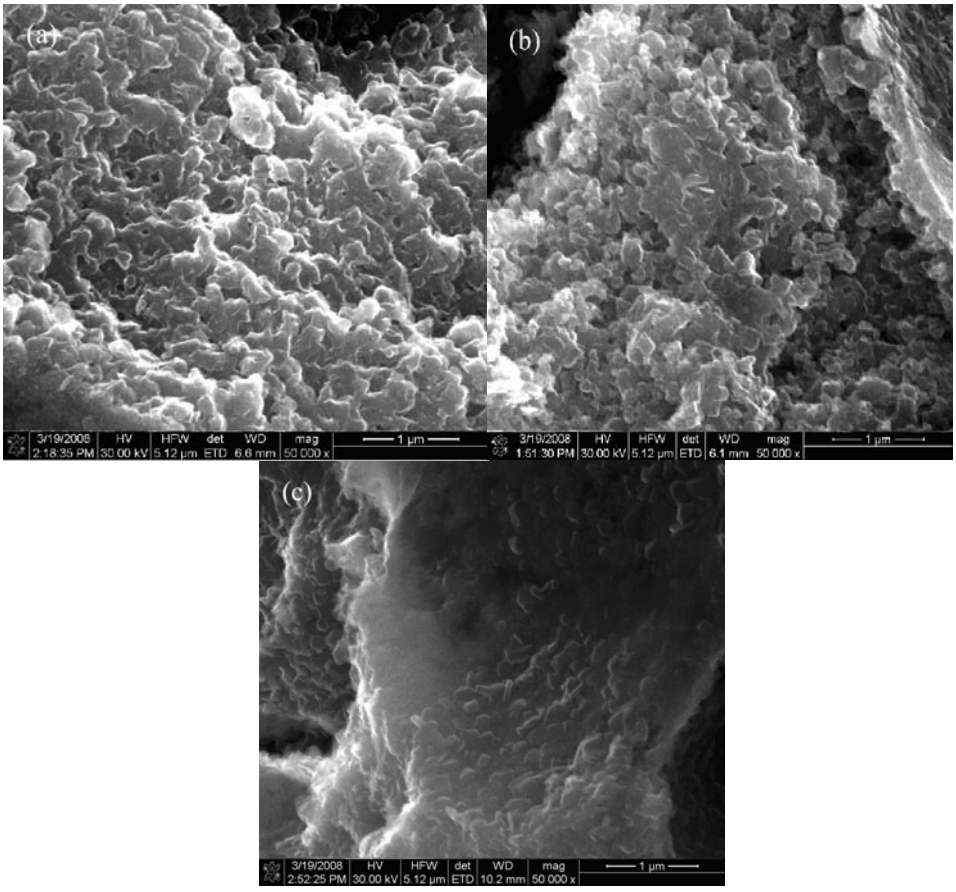

Figure 3.4 FEG-SEM images of samples: (a) Sample A; (b) Sample B; (c) Sample C.

3.1.5 T_c and J_c

Figure 3.5 presents the magnetic susceptibility as a function of temperature in an applied field of H = 1 Oe for zero field cooled samples. The magnetic susceptibility for the field cooled condition is not displayed in the figure, since the values are very close to zero.

This demonstrates that the flux pinning force in all the samples is quite large. T_c decreases from sample A to sample C, and then further decreases to sample B. The inset figure shows T_c against lattice parameter *a* for the three samples.

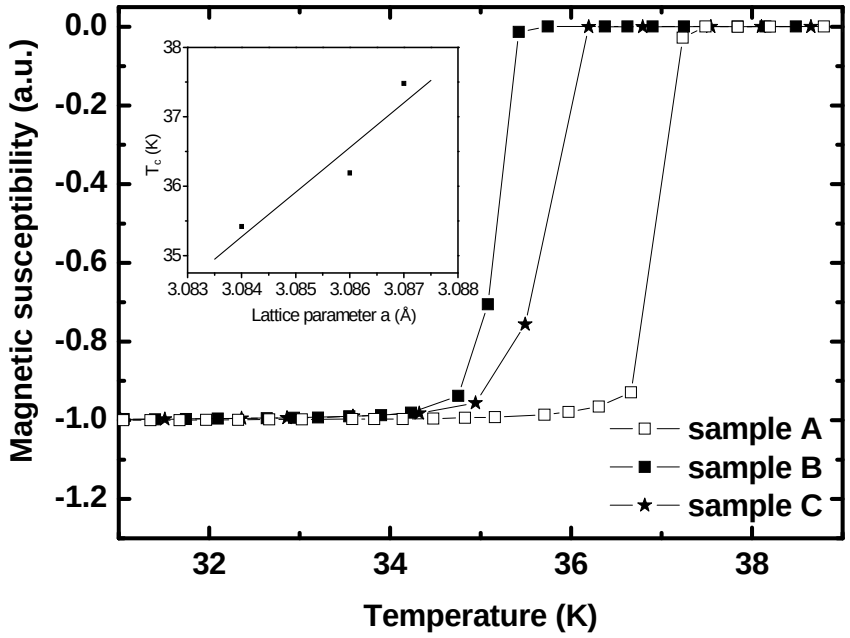

Figure 3.5 Magnetic susceptibility as a function of temperature for the MgB_2 samples. The inset shows the critical temperature as a function of the *a*-axis lattice parameter.

It is clear that T_c decreases with decreasing lattice parameter *a*. A decrease in the lattice parameters, especially the *a* parameter, reduces the electronic density of states (DOS) at the Fermi level and hardens the optical E_{2g} phonons [192]. The reduction in the DOS and the hardening of the E_{2g} phonons depress T_c. Lattice parameter *a* for clean (ideal) MgB_2 is 3.083 Å. It is expected that clean MgB_2 has a high T_c at around 39 K. Extrapolation of the trend line in the inset predicts a T_c of about 34.5 K at a = 3.083 Å, which is smaller than the expected T_c for clean MgB_2. The reason is that a = 3.083 Å in the figure does not correspond to clean MgB_2. Defects in MgB_2 may change the lattice parameters. Some defects (such as vacancies) expand the lattice, while other defects

(such as interstitial atoms and some substitution atoms) compress the lattice parameters. The lattice parameters in our samples are larger than the ideal parameters, since there are a large amount of vacancies in the samples. If a certain amount of interstitial atoms or/and substitution atoms can be introduced in these samples, the increased lattice parameter *a* may be reduced to *a* = 3.083 Å, namely the extrapolation point in the figure. The extrapolated sample is not clean MgB_2. It is affected by not only defects expanding the lattice, but also defects compressing the lattice. Therefore, T_c in the extrapolated sample is smaller than that in a clean sample due to the increased amount of defects.

ΔT_cs are 0.52 K, 0.58 K, and 1.02 K for samples A, B, and C, respectively. The small ΔT_cs in samples A and B demonstrate that the defects are homogeneously distributed on the scale of the coherence length [227]. Sample C exhibits a higher ΔT_c, suggesting that the distribution of defects is more inhomogeneous. This is due to the crystalline structure of the boron precursor powder used in sample C. Chen *et al.* [50] also observed larger ΔT_cs for crystalline boron precursor samples than for amorphous boron precursor samples.

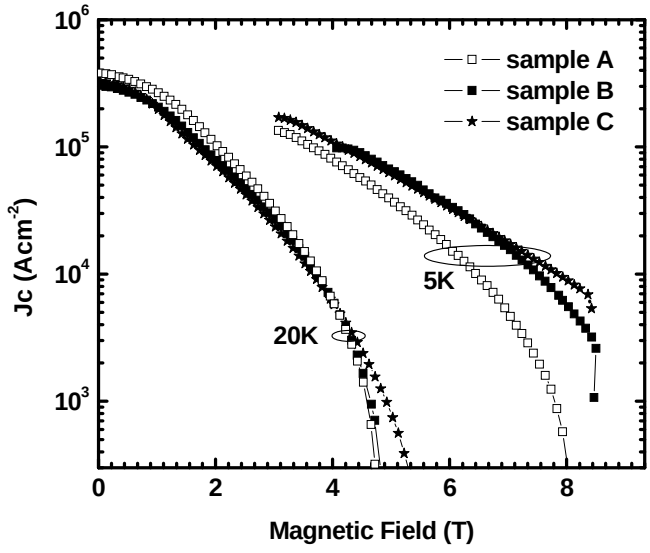

Figure 3.6 J_c curves for MgB_2 samples made from different B powders.

J_c as a function of magnetic field is shown in Figure 3.6. It can be seen that the J_c performance in sample C shows a significant improvement at high field at both 5 K and 20 K. At 5 K and 8 T, the J_c value is 9.1 x 10^3 Acm^{-2}, which is two times higher than for sample B, and a factor of 40 higher than for sample A. At 20 K and high fields, J_c is increased from sample A to sample B, and then to sample C. The J_c improvement at high fields should be mainly attributed to the enhancement of H_{c2}. It is well known that the grain boundary pinning is the major pinning mechanism at high fields in MgB_2. The contribution to J_c due to the surface pinning on grain boundaries can be calculated from $\frac{\mu_0 S_v (H_{c2}-H)^2}{4\kappa^2 H_{c2}^{1/2} H^{1/2}}$ [18], where S_v is the grain boundary surface area per unit volume, κ the Ginzburg-Landau parameter, and H the applied field. It can be seen from this equation that J_c at high fields near H_{c2} is predominantly determined by H_{c2} [192]. Higher H_{c2} leads to higher J_c at high fields near H_{c2}. Since H_{c2} and the irreversibility field (H_{irr}) are closely related to each other, we replace H_{c2} by H_{irr}, for which the values at 20 K for samples A, B and C are 4.77 T, 4.86 T, and 5.56 T, respectively. This gives a good explanation of the J_c improvement from sample A to sample B, and then to sample C at high fields. H_{c2} is affected by the disorder induced by any defects in MgB_2. Disorder reduces the mean free path and, in turn, increases H_{c2}. Microstrain is a measure of the disorder. The higher microstrain in sample C, shown in Table 3.2, is suggestive of higher disorder and a higher H_{c2}. Smaller grain size (more grain boundary) and a larger amount of MgO impurity in sample C, as listed in Table 3.2, may be the causes for higher disorder and higher H_{c2}.

At zero field and 20 K, J_cs of samples A, B, and C are ~ 380905 Acm^{-2}, 304312 Acm^{-2}, and 328764 Acm^{-2}, respectively. J_c of sample A is higher than for the other samples, while sample C has a higher J_c than sample B. At zero field, the inter-flux-line spacing (d) tends to infinity. According to the Dew-Hughes model [18], all the defects act as point pinning centres at zero field, and the self-field J_c linearly increases with H_{c2} and decreases with κ^2 [18]. The self-field J_c is also proportional to the connectivity [192]. Since it is difficult to determine κ due to the two-band contribution, we calculated an effective κ instead of the real κ by solving the equation: $\frac{\ln(\kappa)+0.5}{2\kappa^2}=\frac{H_{c1}}{H_{c2}}$ [192]. H_{c2} was replaced by the value of H_{irr}, and H_{c1} was measured as the field from which the magnetic hysteresis curve starts to deviate from linearity. The calculated effective κs are 7.4, 8.3, and 9.9 for samples A, B, and C, respectively. κ is enhanced from sample A to sample B, and then to sample C. This trend is same as for H_{c2}. The reason is because both κ and H_{c2} increase with disorder. However, κ^2 changes faster than H_{c2}. This indicates that as the disorder increases, the negative influence of κ^2 on the self-field J_c is more important than the positive influence of H_{c2}. The connectivity can be estimated by the effective cross-sectional area (A_F), defined as $A_F = \Delta\rho_{ideal}/(\rho_{300K}-\rho_{40K})$ [112]. $\Delta\rho_{ideal}$ is the ideal change in resistivity from 300 K to 40 K for a fully connected sample. It is set to be 7.3 μΩcm according to Ref. [228]. ρ_{40K} and ρ_{300K} were obtained from the resistivity measurements. The A_Fs for samples A, B, and C are 0.23, 0.15, and 0.2, respectively. It can be found that sample A has the best connectivity and sample B has the worst. We calculate a combined parameter, $\alpha = A_F\frac{H_{c2}}{\kappa^2}$, to represent the total influence of the relevant factors (H_{c2}, κ and A_F) on the self-field J_c. The values of α are 0.148, 0.088, and 0.112 for samples A, B, and C, respectively, which produces a very good linear relationship between α and the self-field J_c. This clearly indicates that the

self-field J_c is mainly determined by the connectivity and the disorder. The latter influences the self-field J_c via H_{c2} and κ.

3.2 Influence of different sintering temperatures [229]

3.2.1 Sample preparation

The precursor powders and ball milling process are same as in Section 3.1. As-supplied crystalline boron powders (99.999%) were ball-milled in toluene. The ball milling process was carried out for 4 h with a rotation speed of 160 rpm under air. MgB_2 pellets were prepared by a solid-state reaction. Boron powders were stoichiometrically mixed, ground, and pressed with magnesium (99%) powder. The samples were sintered at the temperatures of 650°C, 850°C, and 1050°C for 30 min under high-purity argon gas. They are defined as samples A, B, and C in Section 3.2, respectively. The heating rate was 5°C per minute. An MgB_2 reference sample prepared from as-supplied crystalline boron powders was also fabricated under the same conditions and sintered at 650°C.

3.2.2 XRD analysis

The XRD patterns for the reference sample and samples A, B, and C are presented in Figure 3.7. All the samples seem to be well developed MgB_2 with some MgO impurity. In the reference sample, peaks of un-reacted crystalline boron at $2\theta = 21.08°$ and 22.1º can be observed, as well as un-reacted magnesium powder. Un-reacted magnesium powder disappears in sample A, and the amount of un-reacted boron is very much smaller. This indicates that the crystalline boron has a better reaction with magnesium

powder after ball milling due to the smaller particle size. As the sintering temperature is increased to 850°C, the un-reacted boron powder disappears. MgB_4 peaks can be detected in sample C, which was made at the high sintering temperature of 1050°C. Because the starting boron and magnesium powders were stoichiometrically mixed, the formation of MgO by reaction of magnesium powder and oxygen trapped in the sealed tube results in insufficient magnesium to form MgB_4.

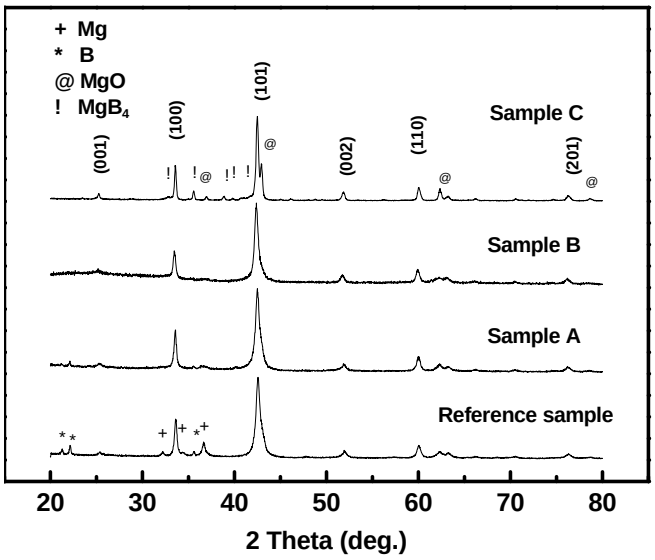

Figure 3.7 XRD patterns for the different samples.

The Rietveld refinement method was performed to analyze the XRD measurements. The refinable parameters include the weight fraction of each phase, the lattice constants of MgB_2, the grain size, and the amount of microstrain. Since the amount of remnant boron in the samples is small, boron is not taken into account in the refinement. A low R_{wp} indicates good agreement between the measured and calculated data. R_{wp}s for the reference sample and samples A, B, and C are 9.57%, 5.6%, 6.89%, and 7.86%, respectively. These low values indicate that the refined results are acceptable. The calculated lattice parameters and the strains along the two lattice axes (*a* and *c*) are

shown in Table 3.3. It can be seen that the reference sample has the largest lattice parameter *a* and the smallest lattice parameter *c*. For samples A, B, and C, lattice parameter *a* decreases with the sintering temperature, while lattice parameter *c* increases from sample A to sample B, and then decreases to sample C. The microstrains in all the samples exhibit anisotropic behavior, namely, the microstrain along the *c*-axis is larger than that along the *a*-axis. The anisotropic microstrain is caused by the anisotropic elastic modulus along the different axes. The smaller elastic modulus along the *c*-axis results in a larger strain [226]. The reference sample has the largest average microstrain, while the average microstrain decreases from sample A to sample B, and then to sample C.

Table 3.3 Parameters and properties for all samples.

Samples	Lattice Parameters (Å)		Microstrain (%)		
	a	*c*	*a*	*c*	Average
Reference	3.088	3.519	0.223	0.765	0.494
A	3.086	3.523	0.288	0.661	0.4745
B	3.085	3.527	0.179	0.359	0.269
C	3.079	3.521	0.162	0.25	0.206

Samples	T_c (K)	J_c (5K, 8T) (Acm^{-2})	ρ_{40k} ($\mu\Omega cm$)	ρ_{300k} ($\mu\Omega cm$)	A_F	ρ_{norm}
Reference	36.5	1906.8	60.47	103.35	0.170	1.410
A	36.2	9100.4	56.07	91.83	0.204	1.568
B	37.2	7316.4	46.62	87.38	0.179	1.144
C	37.6	20.1	30.13	68.73	0.189	0.781

From Table 3.3, we can see that T_c for the ball-milled sample sintered at 650°C is slightly depressed compared to the reference sample. In addition, as the sintering temperature increases, T_c increases. It is clear that T_c increases with decreasing lattice parameter *a* and with decreasing average microstrain. A decrease in the lattice

parameters, especially the *a* parameter, reduces the electronic density of states (DOS) at the Fermi level and hardens the optical E_{2g} phonons [192]. The reduction in the DOS and the hardening of the E_{2g} phonons depress T_c. Table 3.3 also shows that the J_c value at 5 K and 8 T for sample B is 9100 Acm^{-2}, which is four times higher than for the reference sample. This non-compositional performance increase can be mainly attributed to the smaller grain size in sample A. Sample A was fabricated from ball-milled, nanosized boron particles, which induced small grain sizes in the sample. As the grain size decreases, the density of grain boundaries increases, and in turn, enhances the pinning force and J_c. J_c behavior in sample C is very poor, primarily due to the amount of MgB_4 impurity. MgB_4 appears as a large second phase, which would act only as a current blocking phase, resulting in depression of J_c. Sample A exhibits a slightly higher J_c than sample B. The reason may be due to the higher H_{c2} in sample A, as shown in Figure 3.11.

3.2.3 Resistivity versus Temperature

The resistivity (ρ) results are shown in Figure 3.8. It can be observed that the resistivity drops dramatically with increasing sintering temperature. The two 650^{o}C samples (the reference sample and sample A) have relatively higher resistivities. The reference sample resistivity is slightly higher than for sample A. The values of ρ_{40K} and ρ_{300K} were collected from Figure 3.8 and are listed in Table 3.3. The reference sample exhibits the largest ρ_{40K} and ρ_{300K}. With increasing sintering temperature from sample A to sample B, and then to sample C, both ρ_{40K} and ρ_{300K} decrease. These ρ_{40K}s are higher than for single crystal (5.3 μΩcm [230]) and for dense filaments made by chemical vapor deposition (CVD) (0.38 μΩcm [66]). The reason can be attributed to poor connectivity

in the studied samples. The XRD patterns in Figure 3.7 show that a large amount of MgO exists in the samples. MgO is mainly present in the grain boundaries as an insulator, which reduces the effective cross-sectional area of the samples and increases the resistivity. The effective cross-sectional area (A_F) can be estimated from the equation, $A_F = \Delta\rho_{ideal}/(\rho_{40K}-\rho_{300K})$, which was proposed by Rowell [112]. $\Delta\rho_{ideal}$ is the ideal change in resistivity from 300 K to 40 K for a fully connected sample. It is set to be 7.3 μΩcm, according to Ref. [228]. The calculated A_F values are displayed in Table 3.3. It can be seen that the A_Fs are around 0.19, indicating poor connection in the samples. The poor connectivity is responsible for the high resistivity.

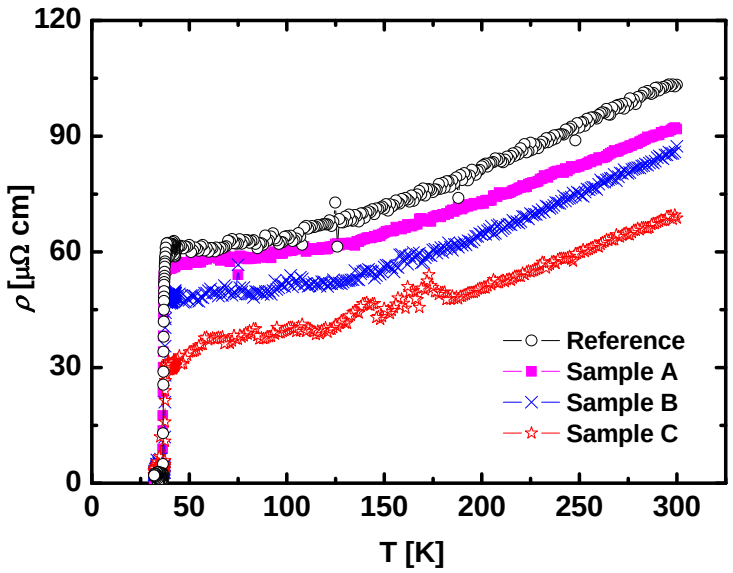

Figure 3.8 Resistivity versus temperature for the four samples.

A_F varies within a small range from 0.17 to 0.204, which cannot be used to explain the big variation of ρ_{40K} from 30.13 μΩcm to 60.47 μΩcm. There needs to be another factor influencing the resistivity. ρ_{40K} is plotted against the average strain in Figure 3.9. It is clear that ρ_{40K} linearly increases with microstrain. The lattice strain is an important parameter for quantifying disorder [192]. ρ_{40K} is close to the temperature-independent

residual resistivity, ρ_0, which originates from electron scattering at defects [192]. This implies that disorder is the major factor affecting ρ_0. The disorder also influences T_c and the normalized resistivity ($\rho_{norm}= \rho_{40K}/(\rho_{300K} - \rho_{40K})$) [192]. T_c versus ρ_{norm} is plotted in Figure 3.10. The solid line represents the trend, and a good linear relationship can be observed. This further indicates that disorder is responsible for the variation of the resistivity in the studied samples.

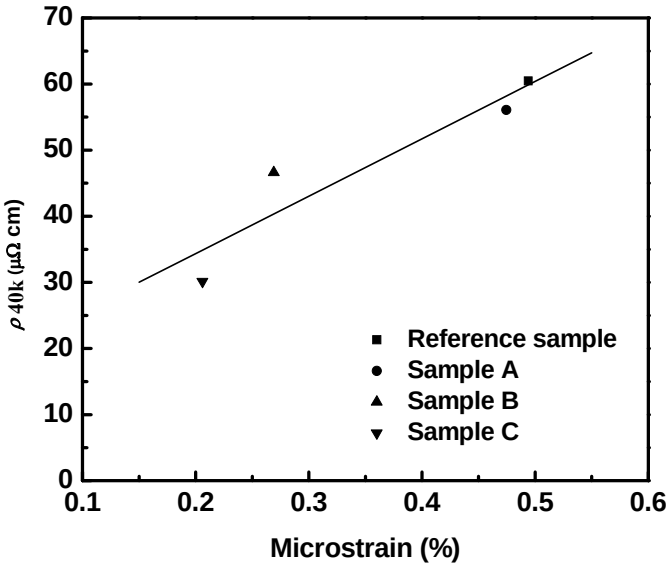

Figure 3.9 ρ_{40K} versus microstrain.

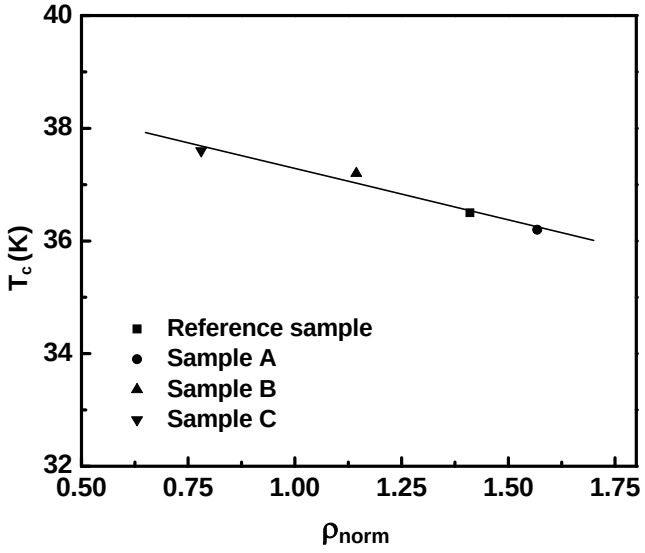

Figure 3.10 T_c versus ρ_{norm}.

Figure 3.11 presents the temperature dependence of H_{c2}, which is defined by 90% of the normal state resistivity. H_{c2} shows a concave temperature dependence. As the temperature increases, H_{c2} decreases. The reference sample has the largest H_{c2}, and sample C has the lowest H_{c2}, while samples A and B have similar H_{c2} values. The reason is due to differences in the coherence length (ξ) that are caused by disorder. Figure 3.12 shows H_{c2} at 22.5 K against microstrain. It is clear that H_{c2} linearly increases with microstrain. A low microstrain indicates less lattice distortion inside the MgB_2 grains and thus a larger mean free path (l) of the superconducting electrons. This will increase the coherence length (ξ) due to the relation: $\frac{1}{\xi} = \frac{1}{\xi_0} + \frac{1}{l}$, where ξ_0 is the value of ξ for the pure superconductor. According to $H_{c2} = \Phi_0/(2\pi\mu_0\xi^2)$, where Φ_0 is the superconducting flux quantum and μ_0 is the magnetic permeability, H_{c2} will decrease as ξ increases.

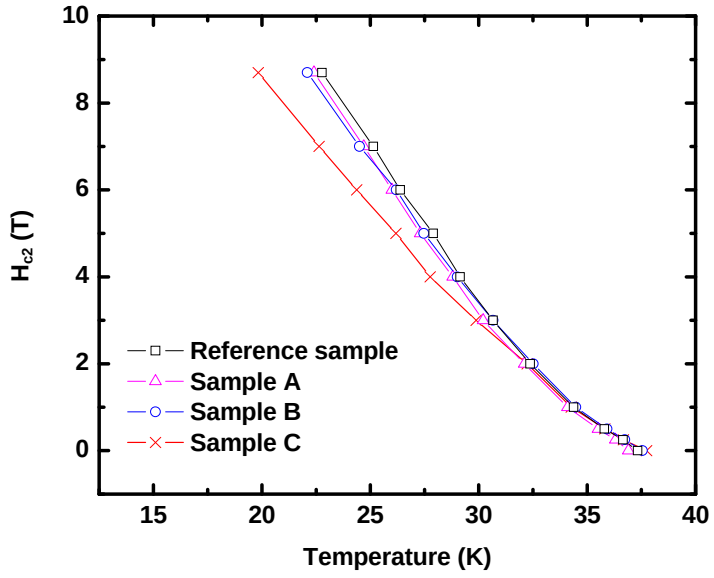

Figure 3.11 Temperature dependence of H_{c2}.

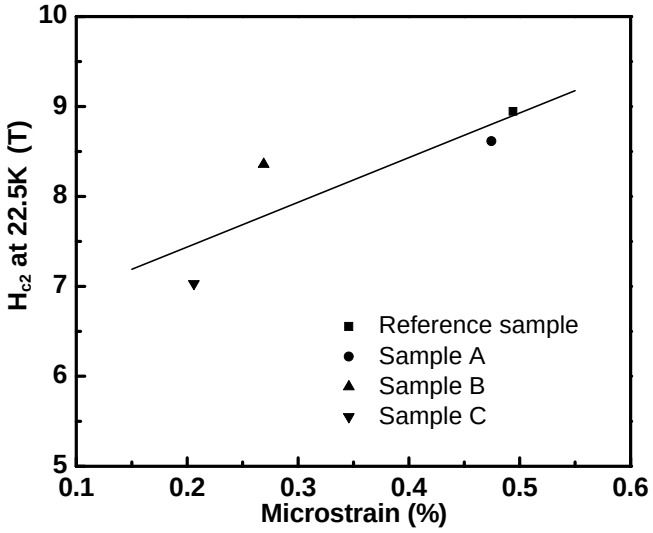

Figure 3.12 H_{c2} versus microstrain.

3.3 Summary

To improve the J_c of MgB_2 and to determine the optimized combination of the particle size, purity, and form of the precursor boron powders, high-purity (99.999%) boron powders with crystalline phase were processed by ball milling and used as precursor powders. A systematic study of the grain size, microstrain, density, lattice parameters, phase fractions, J_c, and T_c has been presented in comparison with MgB_2 samples made from as-supplied and ball-milled high purity amorphous boron powders. It has been found that the J_c of the MgB_2 that was made from these precursors was 9.1×10^3 Acm^{-2} at 5 K and 8 T, which is two times higher than for the sample made from ball-milled amorphous boron powders, and a factor of 40 higher than for the sample from as-supplied amorphous boron powders. Significant improvement in J_c at high fields is attributed to the H_{c2} enhancement caused by the increased disorder. The effect of the sintering temperature on the transport properties in the samples made from ball-milled

high purity boron powders and as-supplied boron powders was also investigated. It was found that the resistivity of the samples made from the ball-milled boron powder is lower than that of the sample from the as-supplied boron powder. As the sintering temperature increases, both resistivity and H_{c2} in the samples made from the ball-milled boron powders decrease. Poor connectivity and large strain are responsible for the high resistivity.

4 Nominal Mg/B Mixing Ratio

It has been found that the stoichiometry of MgB_2 significantly affects the superconducting properties. Unfortunately, discrepancies on this topic still exist. Jiang *et al.* [231] reported that slightly Mg-deficient samples showed higher J_c in high fields, whereas samples with stoichiometric Mg or a slight excess of Mg exhibited better J_c in low fields. The reason for higher J_c in high fields was attributed to the enhanced grain boundary pinning caused by the smaller grain size. Perner *et al.* [232] found that the best T_c and J_c were obtained for an Mg surplus of 5wt%. Chen *et al.* [233] reported that nominally Mg-deficient samples had enhanced in-field J_c values compared to samples prepared in an Mg excess environment. They attributed this to the increased structural disorder.

Susner *et al.* [234] have concluded that the Mg/B ratio significantly affects the microstructure, H_{irr}, and J_c. They also investigated the influence of SiC additions to the higher excess Mg compositions (around 15 %). It has been found that 5 mol% SiC doping yielded a transport J_c at 4.2 K and 8 T of 5×10^4 A/cm^2, with a H_{irr} of 21 T (100 A/cm^2 criterion). Recent results showed that a 10 wt.% Mg excess in the Mg-B system can improve the J_c values over the entire range (0 - 8.5 T) of measurement fields [235]. This stimulated an idea that SiC doping in MgB_2 with Mg excess may be effective in improving the microstructure and J_c performance of MgB_2 in both low and high fields. So, systematic studies on the effects of the nominal mixing ratio of Mg to B in SiC-doped MgB_2 are necessary and urgent.

In Section 4.1, I systematically investigate the effects of the nominal mixing ratio of Mg to B, which is varied from 0.9:2 to 1.3:2, on the superconducting properties of Mg_xB_2. The Mg:B mixing ratio for ideal MgB_2 is 1:2. A detailed analysis of the fraction of each phase, the lattice parameters, microstrain, T_c, H_{c2}, J_c, and connectivity has been conducted. It was found that the sample with x = 1.1 exhibits the highest J_c in all fields at 5 K and 20 K. A clear correlation between J_c and connectivity indicates that the good connectivity in the sample with 10% Mg excess caused the J_c enhancement in both low fields and high fields.

In Section 4.2, the effects of the nominal Mg/B ratio (x:2), varying from 1:2 to 1.2:2, in 10 wt.% SiC-doped MgB_2 samples on the superconductivity, Raman spectra, current transport properties, and flux pinning mechanisms of MgB_2 are investigated systematically. The results show that the sample with 15 wt% Mg excess in 10 wt% SiC-doped MgB_2 exhibits the best performance. J_c is improved at all fields. The reason can be attributed to the improved connectivity and the increased disorder. Compared with other SiC-doped MgB_2 samples, T_c in the sample with 15 wt% Mg excess has also been enhanced due to the increased e-ph coupling caused by the lower interband scattering.

4.1 Optimization of nominal Mg/B mixing ratio in pure MgB_2 [236]

4.1.1 Sample preparation

Mg_xB_2 samples with x = 0.9, 1, 1.1, 1.2, and 1.3 were prepared by solid state reaction. Mg powder (1-11 μm) and amorphous boron powder (99%) were used as the starting

materials. The powders were carefully mixed by grinding in a mortar and pressed into pellets 13 mm in diameter and about 2.5 mm thick. The pellets were sealed into Fe tubes. The sealed tubes were then heated in a tube furnace under pure Ar gas and sintered at 800°C for 60 h prior to cooling to room temperature.

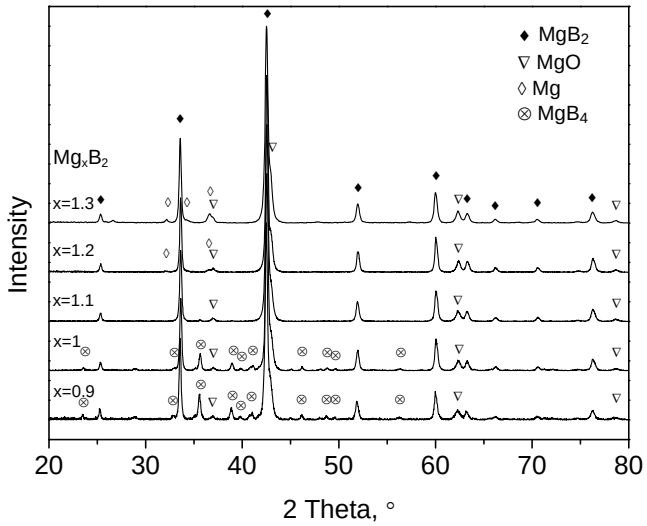

Figure 4.1 Powder XRD traces of Mg_xB_2 samples with x = 0.9, 1, 1.1, 1.2, and 1.3.

4.1.2 XRD analysis

Figure 4.1 shows the powder XRD patterns of Mg_xB_2 samples with x = 0.9, 1, 1.1, 1.2, and 1.3. All the major peaks of the MgB_2 hexagonal structure (space group P6/mmm) can be identified, indicating that the samples mainly consisted of the desired MgB_2 phase. Besides MgB_2, the impurity MgO was present in all the samples. Two strong peaks of the MgO phase are located at $2\theta \approx 42.96^{\circ}$ and $2\theta \approx 62.28^{\circ}$. Another two weaker peaks at $2\theta \approx 36.80^{\circ}$ and $2\theta \approx 78.54^{\circ}$ can also be observed in the XRD patterns. MgO impurity could be formed by reactions during the sintering process. The reacting oxygen could be introduced from the air trapped in the tubes and also from oxygen in the

starting boron powers. For the samples with x < 1.1, MgB_4 was detected. MgB_4 exists due to a deficiency of magnesium, which is caused by evaporation of the magnesium and formation of MgO. At x = 1.1, MgB_4 disappears, and only MgO impurities can be observed. When x further increases to 1.2, magnesium metal becomes excessive. Therefore, two major peaks of magnesium metal are displayed in the XRD patterns of $Mg_{1.2}B_2$ and $Mg_{1.3}B_2$ at $2\theta \approx 36.62^{\circ}$ and $2\theta \approx 32.12^{\circ}$.

Table 4.1 Refined parameters in Mg_XB_2.

Samples	R_{wp}(%)	Weight fraction (%)				Lattice Parameters (Å)		Microstrain (%)
		MgB_2	MgO	MgB_4	Mg	a	c	
$Mg_{0.9}B_2$	7.48	69.03	7.06	23.91		3.085	3.526	0.201
MgB_2	5.87	73.2	7.53	19.27		3.084	3.525	0.167
$Mg_{1.1}B_2$	6.05	90.03	9.97			3.084	3.525	0.216
$Mg_{1.2}B_2$	6.38	88.73	10.4		0.87	3.085	3.523	0.185
$Mg_{1.3}B_2$	6.202	85.07	12.67		2.25	3.084	3.519	0.229

Rietveld refinement was performed to analyze the XRD measurements. The refinable parameters include the weight fraction of each phase, the lattice parameters of MgB_2, and the percentage of microstrain. A measure of similarity (R_{wp}) between the measured diffraction patterns and the simulated diffraction patterns is shown in Table 4.1. A low R_{wp} indicates good agreement between the measured and simulated data. All the R_{wp} values are below 7.5%. This indicates that the calculated results are acceptable. The calculated weight fraction of each phase in the samples is also listed in Table 4.1. It was found that the weight fraction of pure MgB_2 phase increased from x = 0.9 to x = 1.1, and then decreased. There are large differences in the weight fraction of MgB_2 phase in the samples, varying from 69.03% to 90.03%. The weight fraction of MgO increases with x. A large amount of MgB_4 phase exists in MgB_2 and $Mg_{0.9}B_2$. Its weight fraction increases with decreasing x. It seems that the existence of MgB_4 significantly reduces

the weight fraction of MgB_2 phase. A small amount of Mg appears in the samples with sufficient Mg precursor powder ($Mg_{1.2}B_2$ and $Mg_{1.3}B_2$). Its fraction increases with x.

The calculated in-plane lattice constant (*a*) in the samples is nearly the same. The inter-plane lattice constant (*c*) decreases from 3.526 Å to 3.519 Å with increasing x. Lattice constant *c* of $Mg_{0.9}B_2$ is larger than the value for the ideal MgB_2 structure (*c* = 3.521 Å). This indicates that a large amount of vacancies exist in the sample. This can be attributed to the nominal deficiency of magnesium in $Mg_{0.9}B_2$ and the formation of MgO. For the sample with stoichiometric Mg (x = 1), the Mg deficiency and the vacancies still exist, due to the formation of MgO. As the nominal ratio of Mg to B (x:2) increases, the nominal or real deficiency of Mg decreases. Therefore, the vacancies in the samples are reduced, resulting in a decreased *c* parameter, as shown in Table 4.1. In the $Mg_{1.3}B_2$ sample, the magnesium deficiency disappears, and boron becomes more than sufficient. The redundant boron atoms may diffuse into the MgB_2 lattice as interstitial atoms, leading to a smaller lattice parameter *c* than the ideal value (*c* = 3.521 Å).

Table 4.1 also shows that microstrain varies from 0.167% to 0.229%. $Mg_{1.3}B_2$ has the largest microstrain, while MgB_2 exhibits the smallest one. Microstrain does not monotonically vary with the nominal ratio of Mg to B. The reason can be attributed to the effect of the MgB_4 and Mg impurities. The presence of a particular impurity can change microstrain. MgB_4 appears in $Mg_{0.9}B_2$ and MgB_2, and its amount decreases with x, while the metal Mg phase exists in $Mg_{1.2}B_2$ and $Mg_{1.3}B_2$ and the amount of it increases with x. Variation in the amount of these impurities produces a complicated relationship between microstrain and the nominal ratio of Mg to B.

4.1.3 T_c, resistivity, and J_c

Figure 4.2 shows a plot of the magnetic susceptibility against the temperature in an applied field of H = 1 Oe for zero field cooled samples. The magnetic susceptibility for the field cooled condition is not displayed in the figure, since the values are very close to zero. This demonstrates that the flux pinning force in all the samples is quite large. From Table 4.2 it can be seen that T_c is similar for all the samples within a range of 0.5 K, which is consistent with the observations of Chen *et al.* [233]. T_c slightly decreases with x. It also linearly decreases with lattice parameter *c*. A decrease in the lattice parameters reduces the electronic density of states (DOS) at the Fermi level and hardens the optical E_{2g} phonons [192]. The reduction in the DOS and the hardening of the E_{2g} phonons depress T_c. ΔT_c in all the samples is sharp, with a width of ~1 K as shown in Figure 4.2. This indicates that the MgB_2 phase is quite homogeneous.

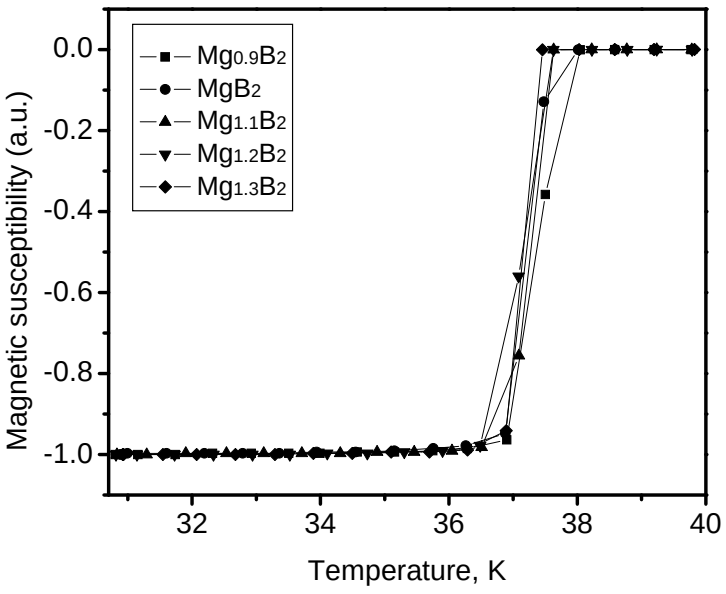

Figure 4.2 Magnetic susceptibility plotted against temperature.

Table 4.2 Properties of Mg_XB_2.

Samples	T_c (K)	J_c at 0T and 20K (Acm^{-2})	J_c at 4.6T and 20K (Acm^{-2})	ρ_{40K} (μΩcm)	ρ_{300K} (μΩcm)	A_F	H_{c2} at 20k (T)
$Mg_{0.9}B_2$	37.88	170399	137	50.38	106.51	0.130	9.24
MgB_2	37.62	228777	147	31.51	70.42	0.188	8.69
$Mg_{1.1}B_2$	37.55	397933	1042	22.48	51.44	0.252	9.4
$Mg_{1.2}B_2$	37.53	374204	226	21.49	53.79	0.226	9.18
$Mg_{1.3}B_2$	37.39	366490	157	23.57	57.87	0.213	9.71

The resistivity (ρ) results are shown in Figure 4.3. It can be observed that the resistivities in the samples with $x \geq 1.1$ are close to each other. The resistivity increases as x decreases from 1.1 to 0.9. The resistivities at 40 K and 300 K (ρ_{40K} and ρ_{300K}) were collected from Figure 4.3 and are listed in Table 4.2. $Mg_{1.2}B_2$ has the smallest ρ_{40K}, while ρ_{300K} in $Mg_{1.1}B_2$ is the smallest. All ρ_{40K}s are higher than for single crystal (5.3 μΩcm, [230]) and for dense filaments made by chemical vapor deposition (CVD) (0.38 μΩcm, [66]). The reason can be attributed to poor connectivity in the studied samples. The XRD traces in Figure 4.1 show the presence of a large amount of MgO in the samples. MgO is mainly present in the grain boundaries as an insulator, which reduces the effective cross-sectional area of the samples and increases the resistivity. The impurity MgB_4 also increases the resistivity in $Mg_{0.9}B_2$ and MgB_2. The presence of Mg metal can reduce the resistivity, since Mg is a good conductor. However, the influence of Mg is not significant because the amount of it is quite small. The effective cross-sectional area (A_F) can be estimated from the equation, $A_F = \Delta\rho_{ideal}/(\rho_{300K}-\rho_{40K})$. It was set to be 7.3 μΩcm according to [228]. The calculated A_F is displayed in Table 4.2. A_F varies from 0.13 to 0.252, indicating poor connection in the samples. It can be noted

from Tables 4.1 and 4.2 that A_F is related to the weight fraction of the MgB_2 phase. This reveals that the poor connectivity is mainly caused by the impurities.

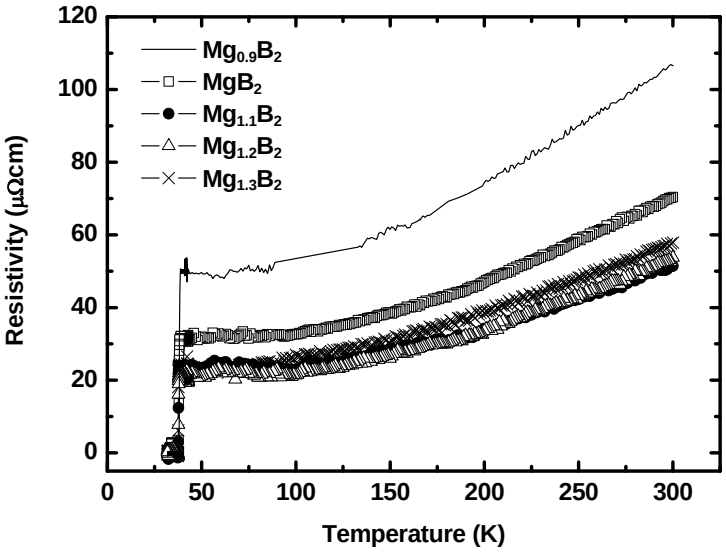

Figure 4.3 Resistivity versus temperature for the samples.

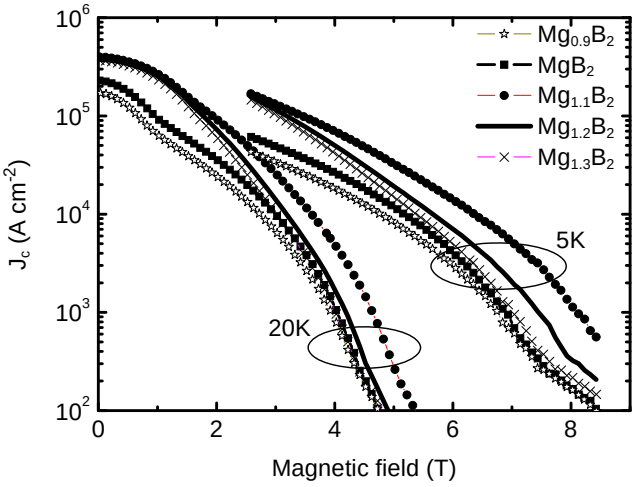

Figure 4.4 Magnetic field dependence of critical current density in Mg_xB_2 at the temperatures of 5 K and 20 K.

The critical current density was calculated from the measured magnetization hysteresis loops, with the calculation based on the Bean model. Critical current densities at 5 K and 20 K are shown in Figure 4.4. J_c in the flux jumping region is not shown in the

figure. It is clear that $Mg_{1.1}B_2$ has the maximum J_c for all fields at both 5 K and 20 K. This means that 1.1:2 is the optimum nominal mixing ratio of Mg to B under current processing conditions. The $Mg_{0.9}B_2$ sample has the lowest J_c. As x increases from 0.9 to 1.1, J_c increases. J_c decreases when x increases from 1.1 to 1.3.

The J_c values at zero field and 20 K (J_{c0}(20 K)) are listed in Table 4.2. The correlation between J_{c0}(20 K) and A_F is shown in Figure 4.5. The solid line represents the trend, as a good linear relationship can be observed. This indicates that the self-field J_c is mainly influenced by the connectivity. J_c at high field (4.6 T) and 20 K is also listed in Table 4.2. J_c at high fields is mainly determined by the H_{c2} and the connectivity [192]. H_{c2} at 20 K, measured at 90% of the normal state resistivity, is shown in Table 4.2. H_{c2} at 20 K as a function of microstrain is presented in Figure 4.6. It is clear that H_{c2} linearly increases with microstrain. H_{c2} is determined by the disorder in MgB_2, whereas microstrain is a measure of the disorder. A lower microstrain is suggestive of a larger mean free path (*l*) of the superconducting electrons. This will increase the coherence length (ξ). According to $H_{c2} = \Phi_0/(2\pi\mu_0\xi^2)$, where Φ_0 is the superconducting flux quantum and μ_0 is the magnetic permeability, H_{c2} will decrease as ξ increases. It was not possible to find a monotonic relationship between H_{c2} and J_c at high field (4.6 T) and 20 K from the results listed in Table 4.2. This implies that another factor besides H_{c2} may play a more important role in J_c at high fields. A comparison of the values of J_c at 4.6 T and 20 K with the connectivity (A_F) shows that J_c increases with A_F. $Mg_{1.1}B_2$ has the largest A_F and highest J_c. Therefore, the connectivity is very likely to be the major reason for the J_c difference at high fields in the studied samples.

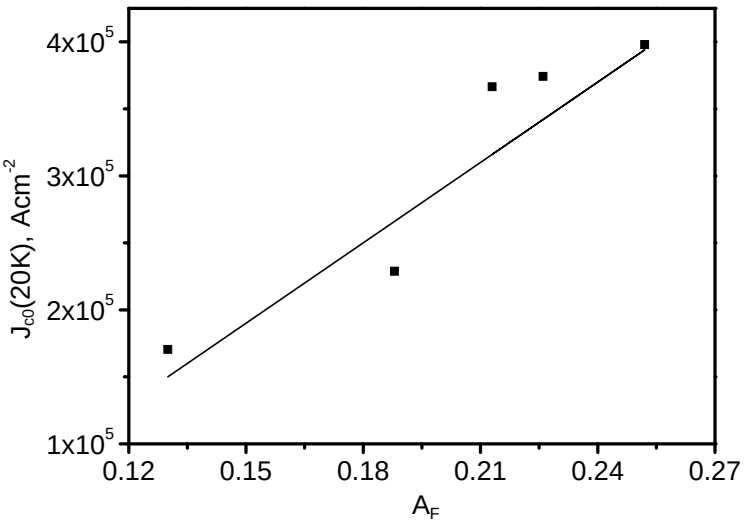

Figure 4.5 Self-field J_c at 20 K vs. A_F.

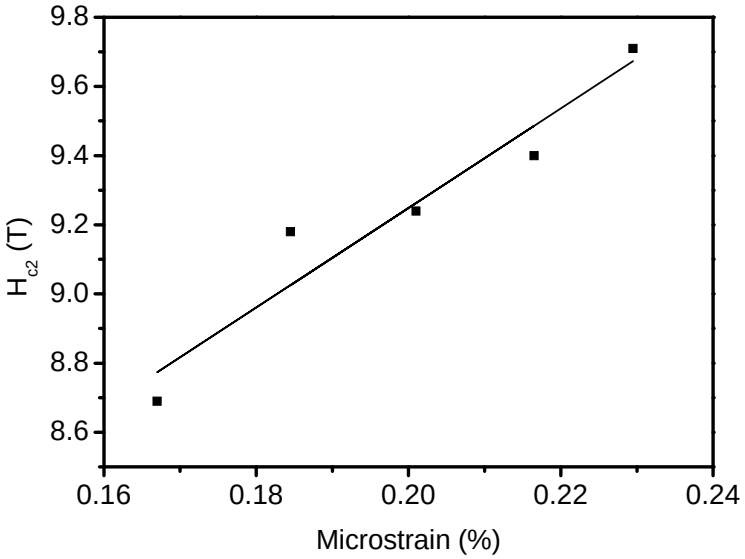

Figure 4.6 H_{c2} at 20 K vs. microstrain.

4.2. Effect of nominal Mg/B mixing ratio in SiC-doped MgB_2 bulk [237]

4.2.1. Sample preparation

It has been found that 10 wt% SiC doping results in the best J_c performance [115, 151]. Therefore, the doping concentration of SiC in this study was fixed at 10 wt.%. The nominal mixing ratio of Mg to B (x:2) varied from 1:2 to 1.2:2. Four Mg_xB_2 samples with x = 1, 1.1, 1.15, and 1.2, which were mixed with 10 wt% SiC, were prepared by solid state reaction. They are termed samples A, B, C, and D in Section 4.2, respectively. A pure MgB_2 sample, made without dopant and by applying the same process, was also fabricated for comparison. It is defined as the reference sample. Mg powder (1-11 μm), amorphous boron powder (99%), and nano-sized crystalline SiC powder (30 nm) were used as the starting materials. The powders were carefully mixed by grinding in a mortar and pressed into pellets 13 mm in diameter and about 2.5 mm thick. The pellets were sealed into Fe tubes. The sealed tubes were then heated in a tube furnace under pure Ar gas and sintered at 800°C for 60 h prior to cooling to room temperature. Higher sintering temperature is expected to improve the connectivity. However, if the temperature exceeds 850^{o}C, MgB_4 maybe formed. Therefore, the sintering temperature is set to be 800^{o}C.

4.2.2 XRD analysis

Figure 4.7 shows the powder XRD patterns of the samples. All the major peaks of the MgB_2 hexagonal structure can be identified, indicating that the samples mainly consist of the desired MgB_2 phase. Besides MgB_2, the impurity MgO exists in all the samples. It is interesting to note that Mg_2Si, which has often been observed in the previous SiC-doped samples [115, 129, 155], could not be detected in our SiC-doped samples (samples A, B, C, and D), while crystalline SiC clearly appears in the XRD patterns. The difference between the current samples and the previous samples is the form of the

SiC powders. Amorphous SiC was used in the previous samples, whereas crystalline SiC was adopted in this study. The XRD pattern in Figure 4.7 indicates that the crystalline SiC powder is not as active as the amorphous in terms of reaction with MgB_2. Therefore, only a small amount of Mg_2Si, which may be below the detectable amount in XRD, is formed, resulting in a large amount of crystalline SiC remaining in the samples.

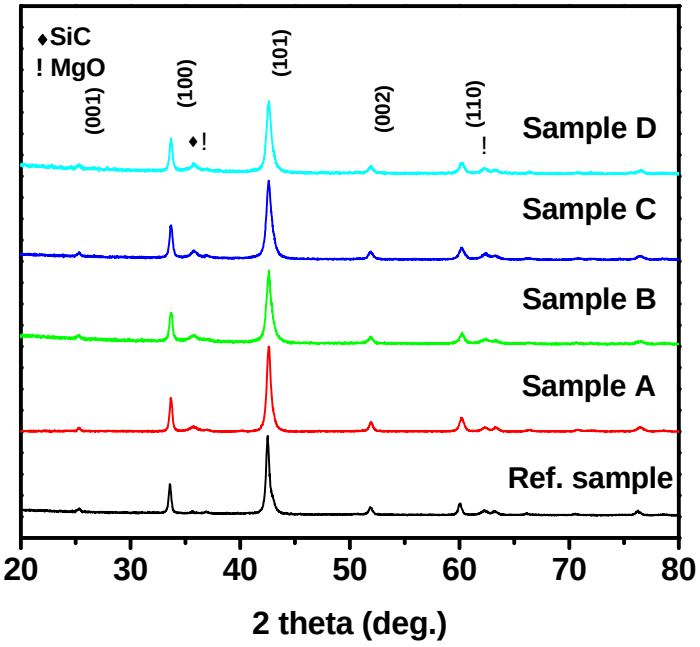

Figure 4.7 X-ray diffraction patterns for the samples.

Rietveld refinement was performed to analyze the XRD measurements. The refinable parameters included the lattice parameters of MgB_2 and the microstrain. The refined results are listed in Table 4.3. The lattice parameters *a* and *c* decrease as x increases from 1 to 1.1, and then increase with x. The reference sample exhibits the highest value of *a*, while its *c* value is lower than for samples C and D. The values of the lattice parameters for ideal MgB_2 are a = 3.083 Å and c= 3.521 Å. It can be seen that lattice parameters *a* and *c* in the reference sample are greater than the ideal values. This indicates that a large amount of vacancies exist in the sample. The starting boron and

magnesium powders in the reference sample were stoichiometrically mixed. The formation of MgO by the reaction of boron powder and oxygen trapped in the sealed tube and in the starting boron powders results in insufficient magnesium to react with boron. The deficiency of magnesium could be responsible for the vacancies. The existence of the vacancies relaxes the lattice around them and increases both the *a* and *c* lattice parameters. When SiC is doped into sample A, lattice parameter *a* becomes smaller than for the reference sample, while lattice parameter *c* remains unchanged. Lattice parameter *a* in sample A is also smaller than the ideal value (*a* = 0.083 Å). This indicates that C atoms have replaced part of the boron atoms. The C-B bond length is about 1.71 Å, which is less than the B-B bond length (1.78 Å) [238]. Since the C-B bond is located in the B plane, the in-plane lattice parameter *a* is decreased, whereas the distance between the B plane and the Mg plane, namely lattice parameter *c*, would not be significantly affected. This phenomenon is often observed in MgB_2 when there is doping with carbon sources [239, 240]. As the mixing ratio of Mg to B (x:2) increases to 1.1:1, the deficiency of magnesium is reduced. This decreases the lattice relaxation caused by the magnesium deficiency and further reduces lattice parameter *a* in $Mg_{1.1}B_2$. However, when x is over 1.15, the magnesium deficiency is completely corrected, and a boron deficiency will be introduced. The boron deficiency also relaxes the lattice and increases *a*. It can be seen that *a* is enlarged when x increases to 1.2. The effect of the boron deficiency on *a* in sample D even compensates for the decrease in *a* caused by the C substitution. Therefore, lattice parameter *a* in sample D is similar to that in the reference sample. In addition, the excess Mg in sample D may be squeezed between the B plane and the Mg plane. Therefore, a significant increase in lattice parameter *c* can be observed in sample D. The unit cell volume of MgB_2 is calculated according the refined lattice parameters *a* and *c*, and is listed in Table 4.3. It can be seen that the reference

sample has a larger unit cell volume than in the doped samples, except for sample D. Among the doped samples, sample B has the smallest unit cell volume.

Table 4.3 Calculated refinable parameters.

Samples	Nominal stoichiometry	Lattice parameters		Volume ($Å^3$)	Strain (%)		
		a (Å)	c (Å)		a-axis	c-axis	Average
Reference	MgB_2	3.087	3.526	29.10	0.345	0.548	0.447
A	MgB_2+10%SiC	3.081	3.526	28.99	0.392	0.628	0.510
B	$Mg_{1.1}B_2$+10%SiC	3.079	3.525	28.94	0.490	0.835	0.663
C	$Mg_{1.15}B_2$+10%SiC	3.082	3.527	29.01	0.461	0.812	0.647
D	$Mg_{1.2}B_2$+10%SiC	3.087	3.532	29.15	0.463	0.694	0.579

The microstrains along the two lattice axes (*a* and *c*) are shown in Table 4.3. The microstrains in the samples exhibit anisotropic behaviour, namely, the microstrain along the *c*-axis is larger than that along the *a*-axis. The anisotropic microstrain is caused by the anisotropic elastic modulus along the different axes. A smaller elastic modulus along the *c*-axis results in a larger strain [226]. The average values are obtained by arithmetically averaging the values along the two lattice axes. As expected, the doped samples have larger microstrain than the reference sample due to C substitution. When x increases, the average microstrain increases from sample A to sample B, and then decreases. This indicates that the nominal Mg/B ratio significantly affects microstrain.

4.2.3 T_c and Raman spectra study

The magnetic susceptibility as a function of temperature in an applied field of H = 1 Oe for zero field cooled samples was measured. The T_c values are displayed in Table 4.4. It can be seen that the reference sample has the largest T_c. As x increases in the doped

samples, T_c increases from sample A to sample C, and then decreases in sample D. Sample C with x = 1.15 exhibits the largest T_c among the doped samples.

Table 4.4 Properties of samples.

Samples	T_c (K)	ρ_{40K} (μΩcm)	ρ_{300K} (μΩcm)	A_F	J_c (20 K, 0 T) (Acm^{-2})	J_c (20 K, 5 T) (Acm^{-2})	κ (20 K)
Reference	37.54	58.6	104.6	0.159	231756	868.4	20.3
A	35.42	128.7	206.5	0.094	201336	2144.3	20.4
B	35.75	99.4	149.0	0.147	242403	3125.5	20.5
C	36.25	76.4	118.7	0.173	326057	4729.0	19.5
D	35.70	94.2	143.6	0.148	309326	3633.7	18.4

In order to analyze the origin of the variation in T_c, Raman spectroscopy was undertaken. Figure 4.8 contains the normalized ambient Raman spectra of all the samples. The Gaussian fittings with three peaks are also shown in Figure 4.8. The ω_1, ω_2, and ω_3 peaks are centered at about 399.1 – 409.3 cm^{-1}, 568.9 – 597.9 cm^{-1} and 702.1 – 779.3 cm^{-1}, respectively. First principles calculations [40, 241, 242] indicated that the high T_c of MgB_2 is due to the electron-phonon (e-ph) coupling between the in-plane boron phonon (E_{2g} mode) and the σ band. The Raman peak of MgB_2 around 600 cm^{-1}, namely the ω_2 peak in Figure 4.8, has been attributed to the E_{2g} mode [243]. The ω_2 peak frequencies are extracted and plotted against x in Figure 4.9. It is clear that the reference sample has a lower ω_2 peak frequency than the doped samples. This can be attributed to the carbon substitution caused by the SiC doping. It is well known that the charge carriers in MgB_2 are holes. The carbon substitution introduces more electrons and therefore reduces the number of holes. This hole-filling effect weakens the e-ph coupling. A theoretical analysis has concluded that the E_{2g} peak frequency increases as the e-ph coupling becomes weaker [244]. Therefore, the doped samples in this study

exhibit higher ω_2 peak frequencies than the reference sample. The same observations have been reported for C-doped and Al-doped MgB_2 [238, 245, 246].

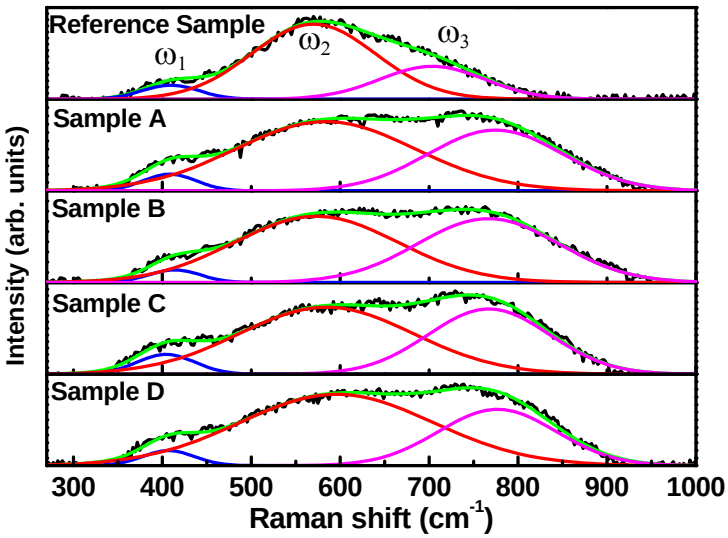

Figure 4.8 Normalized Raman spectra with three-peak Gaussian fitting.

It can be seen from Figure 4.9 that the ω_2 peak frequency decreases as x rises from 1 to 1.15, and then increases for x = 1.2. Since all the doped samples have the same doping concentration (10 wt.%) of SiC, the hole-filling effects should be similar. An additional effect causing the variation of the ω_2 peak frequency may be the interband scattering. There are two major factors affecting the interband scattering: lattice parameters and defects. The σ band is located in the boron plane, while the π band is also centred in the boron plane and extends out towards the Mg plane. Therefore, lattice parameter *a* in the boron plane influences the interband scattering. A decreased lattice parameter *a* will increase the interband scattering. This will harden the E_{2g} phonon and weaken the e-ph coupling. From Table 4.3, we can see that lattice parameter *a* first decreases with x and then increases. This will cause the ω_2 frequency to first increase and then decrease. However, this trend is opposite to the observed ω_2 peak frequencies in Figure 4.9. This

implies that there is another factor playing a more important role on the interband scattering than lattice parameter *a*. The major defects in the studied samples are the vacancies caused by Mg deficiency and B deficiency. An increase in the amount of vacancies will reduce the interband scattering and harden the E_{2g} phonon. We know that the vacancy defects decrease with x for low mixing ratios due to healing of the Mg deficiency and increase with x for high mixing ratios owing to the formation of a B deficiency. Therefore, as x increases, the effect of the vacancy defects depresses the ω_2 frequency to the minimum and then increases it. Figure 4.9 shows that the measured ω_2 frequency follows the same trend as the effect of the vacancy defects. This indicates that the vacancy defects caused by the Mg deficiency and the B deficiency provide a greater contribution to the interband scattering than lattice parameter *a*.

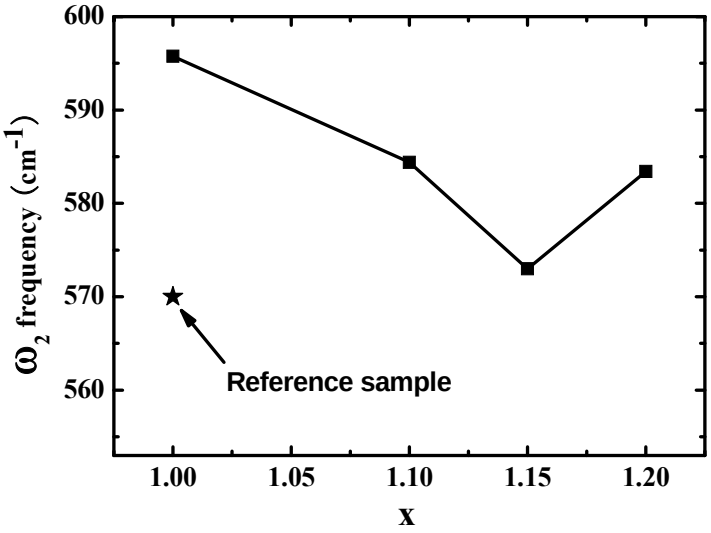

Figure 4.9 ω_2 peak frequency against x.

For the strong electron-phonon coupling superconductors, T_c can be predicted from the McMillan equation [244], as modified by Allen and Dynes [247]:

$$T_c = \frac{\langle\omega\rangle}{1.2}\exp\left(\frac{-1.04(1+\lambda)}{\lambda-\mu^*(1+0.62\lambda)}\right) \quad (4.1)$$

where $\langle\omega\rangle$ is the averaged phonon frequency, λ is the e-ph coupling constant, and μ^* is the Coulomb pseudopotential. It can be seen from Eqn. (4.1) that T_c increases with both $\langle\omega\rangle$ and λ for the commonly-used μ^* of about 0.13 in MgB_2 [248]. In addition, we know that $\langle\omega\rangle$ decreases as λ increases. Therefore, if the e-ph coupling is strengthened, namely, λ is increased, $\langle\omega\rangle$ will be correspondingly reduced. The increased λ and the decreased $\langle\omega\rangle$ have opposite effects on T_c. The former enhances T_c while the latter depresses T_c. Therefore, T_c will increase to a maximum and then decrease as the e-ph coupling (λ) increases. However, the λ value, corresponding to the maximum T_c, is much higher than the common range of λ (0.7-1.0) in MgB_2 [40, 241, 242]. This leads to a monotonic increase of T_c with λ in the MgB_2 system. The e-ph coupling in the SiC-doped samples is weaker than in the reference sample due to the carbon substitution. Therefore, the reference sample has the highest T_c. In the doped samples, the vacancy defects significantly affect the e-ph coupling strength. Sample C with fewer vacancies yields a higher e-ph coupling constant, resulting in enhancement of T_c.

4.2.4 Resistivity and connectivity

The resistivities at 40 K (ρ_{40K}) and at 300 K (ρ_{300K}) are listed in Table 4.4. It can be seen that ρ_{40K} and ρ_{300K} in the reference sample are smaller that those in the SiC-doped samples, while sample A with x = 1 exhibits the highest ρ_{40K} and ρ_{300K}. The resistivities decrease as x increases up to 1.15. When x further increases from 1.15 to 1.2, ρ_{40K} and ρ_{300K} are enhanced. The effective cross-sectional area (A_F) is displayed in Table 4.4. It

can be seen that the A_Fs are below 0.18, indicating poor connection in the samples. The poor connectivity is responsible for the high resistivity. Sample A has the smallest A_F, while sample C exhibits the highest value.

4.2.5 SEM observations

Figure 4.10 shows FEG-SEM images of the doped samples. It can be seen that sample C is denser than the other samples. This confirms that sample C has the best connectivity. The densities in the reference sample and in samples A to D are 1.365 g/cm^{-2}, 1.313 g/cm^{-2}, 1.374 g/cm^{-2}, 1.393 g/cm^{-2}, and 1.246 g/cm^{-2}, respectively. Higher density means better connectivity. The density measurements support this estimation of the connectivity. MgB_2 is formed by diffusion of Mg atoms into the boron lattice. Since the impurities profoundly influence the Mg diffusion, the crystallization and connectivity are strongly related to the amount of the impurities. The doping with SiC in sample A introduces a large amount of impurities, such as remnant SiC, as shown in Figure 4.7, and results in the formation of Mg_2Si. Therefore, compared to the reference sample, the connectivity in sample A is reduced. Both the reference sample and sample A have a nominal stoichiometric Mg/B ratio (1:2). This inevitably introduces remnant B due to the formation of MgO. Remnant B as an impurity in MgB_2 will degrade the connectivity. As the nominal Mg/B ratio increases, the remnant B is reduced, leading to improved connectivity in samples B and C. When the nominal Mg/B ratio is further increased, the excess B disappears, whereas excess Mg appears in $Mg_{1.2}B_2$. The remnant Mg impurity in this sample decreases the connectivity, as indicated by A_F in Table 4.4.

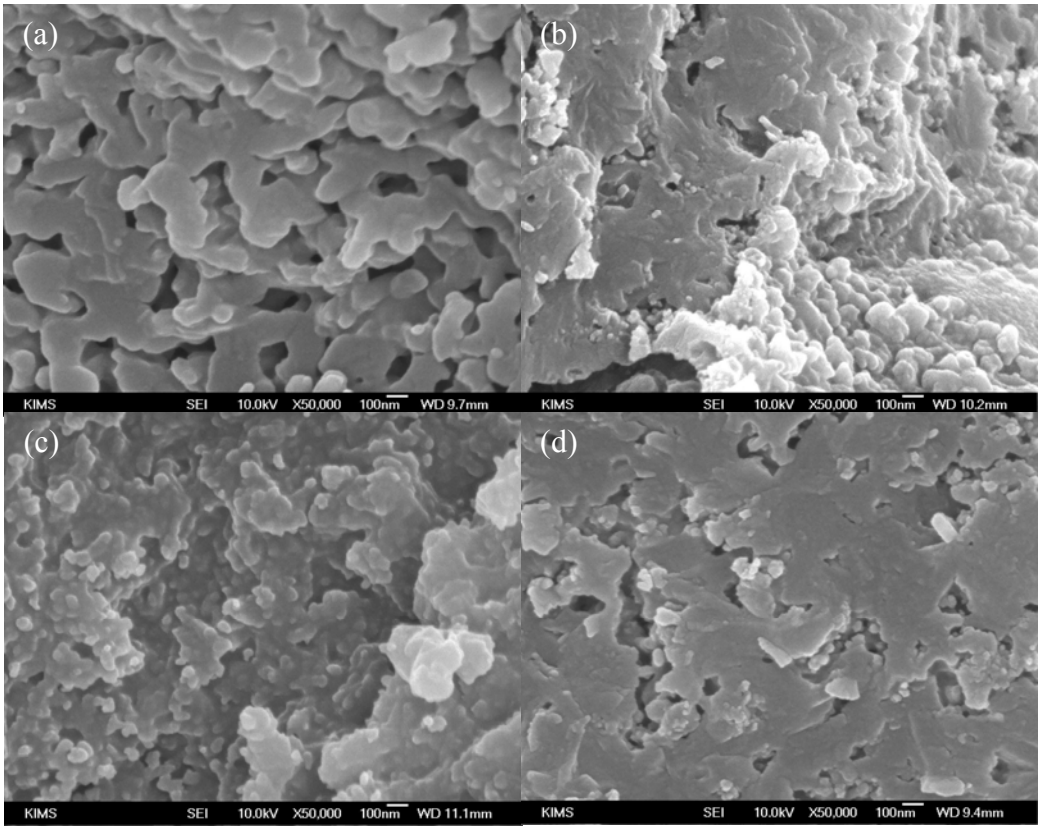

Figure 4.10 FEG-SEM images: (a) sample A; (b) sample B; (c) sample C; (d) sample D.

4.2.6 H_{c2} and J_c

Figure 4.11 demonstrates the temperature dependence of the resistive upper critical magnetic field, H_{c2}, which is defined by 90% of the normal state resistivity. It can be seen that H_{c2} has concave temperature-dependence curves. As the temperature increases, H_{c2} decreases. The reference sample has the lowest H_{c2}. When SiC is doped into MgB_2, H_{c2} is significantly increased. The nominal Mg/B ratio (x:2) also influences H_{c2}. H_{c2} rises from sample A to sample B. Samples B, C, and D have similar H_{c2}, and H_{c2} slightly decreases with x.

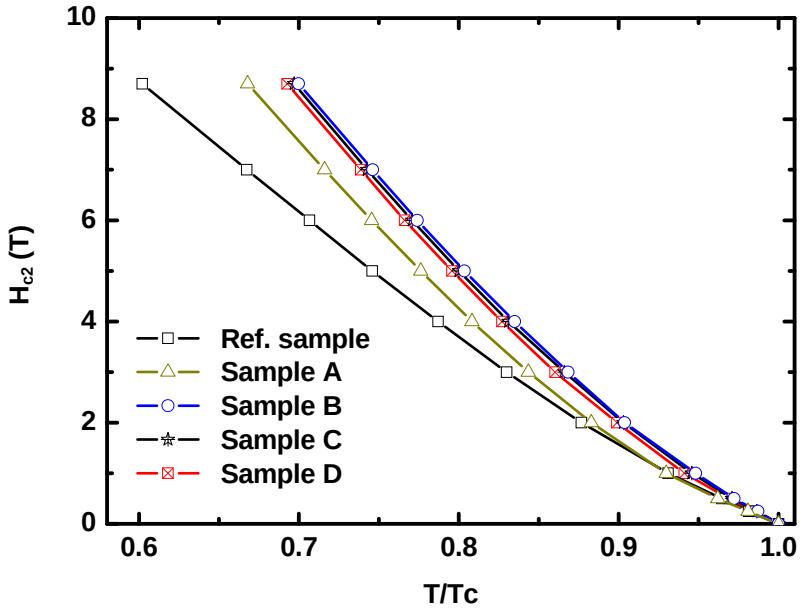

Figure 4.11 Temperature dependence of H_{c2}.

The H_{c2} difference in the samples can be attributed to the variation in the coherence length (ξ) that is caused by the disorder. Figure 4.12 shows H_{c2} at $T/T_c = 0.7$ against microstrain. The solid line is the trend line. It is clear that H_{c2} increases with microstrain. A low microstrain indicates less disorder inside the MgB_2 grains and thus a larger mean free path (l) of the superconducting electrons. This will increase the coherence length (ξ) due to the relation: $\xi^{-1} = \xi_0^{-1} + l^{-1}$, where ξ_0 is the value of ξ for the pure superconductor. According to $H_{c2} = \Phi_0/(2\pi\mu_0\xi^2)$, where Φ_0 is the superconducting flux quantum and μ_0 is the magnetic permeability, H_{c2} decreases with increasing ξ. Therefore, a larger H_{c2} is caused by increased disorder. Figure 4.12 also plots H_{c2} as a function of the intensity ratio of the ω_3 peak to the ω_2 peak ($I_{\omega3}/I_{\omega2}$), which is extracted from Figure 4.8. The dashed line represents its trend line. It can be seen that H_{c2} linearly increases with $I_{\omega3}/I_{\omega2}$. $I_{\omega3}/I_{\omega2}$ is another indicator of disorder. A larger $I_{\omega3}/I_{\omega2}$ means higher disorder. The plot of H_{c2} against $I_{\omega3}/I_{\omega2}$ confirms that the enhanced H_{c2} is due to the increased disorder.

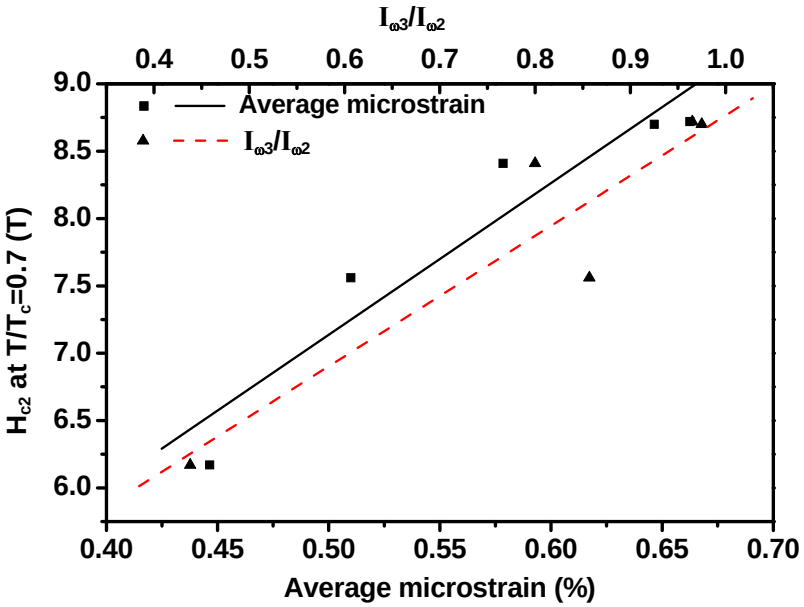

Figure 4.12 H_{c2} against average microstrain and $I_{\omega3}/I_{\omega2}$.

J_c was calculated from the measured magnetization hysteresis loops, with the calculation based on the Bean model. J_c values at 5 K and 20 K are shown in Figure 4.13. At 5 K under low fields, flux jumping exists, as has been explained in the literature [35]. J_c in the flux jumping region is not shown in the figure. At 5 K and high fields, the reference sample has lower J_c than the doped samples, while in the doped samples J_c increases with x up to 1.15 and decreases as x increases from 1.15 to 1.2. J_cs at 20 K under 0 T and 5 T are listed in Table 4.4. Compared to the reference sample, sample A (x = 1) shows an increase in J_c by a factor of 2.5 for high field (5 T), while its self-field J_c is lower than that of the reference sample. In Mg-rich samples ($x \geq 1.1$), J_c can be simultaneously increased for both low fields and high fields. The optimum Mg/B ratio is 1.15:2 in sample C. J_c of sample C at 20 K and 5 T is higher than that of sample A by a factor of 2.3, while its self-field J_c is higher than that of the reference sample by a factor of 1.4. These results clearly show that optimization of the nominal Mg/B mixing ratio can significantly increase J_c for all fields.

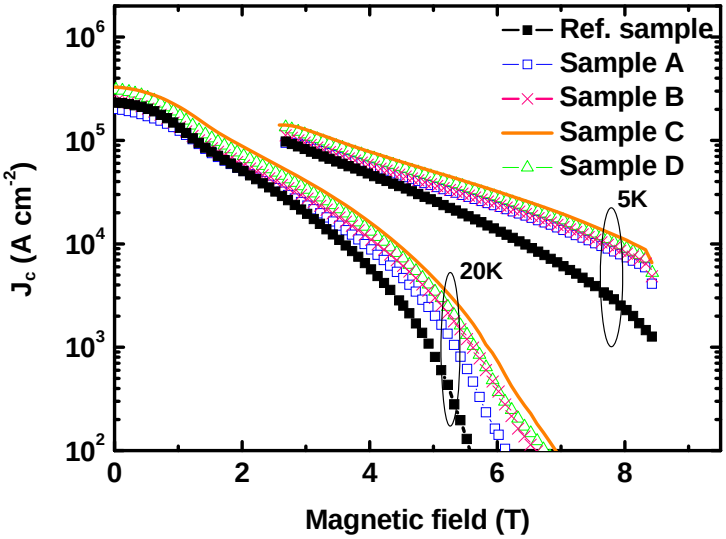

Figure 4.13 Critical current density $J_c(H)$ at 5 K and 20 K.

It is well known that grain boundary pinning is the major pinning mechanism at high fields in MgB_2. The J_c caused by the grain boundary surface pinning can be calculated from $\frac{\mu_0 S_v (H_{c2}-H)^2}{4\kappa^2 H_{c2}^{1/2} H^{1/2}}$ [18], where S_v is the grain boundary surface area per unit volume, κ the Ginzburg-Landau parameter, and H the applied field. In addition, J_c is also proportional to the connectivity [192]. To describe the total influence of H_{c2}, κ, and A_F on J_c at high fields, we define a combined parameter $\alpha_1 = A_F \frac{(H_{c2}-H)^2}{\kappa^2 H_{c2}^{1/2}}$ for H = 5 T. Since it is difficult to determine κ due to the two-band contribution, we calculated an effective κ instead of the real κ by solving the equation: $\frac{\ln(\kappa)+0.5}{2\kappa^2} = \frac{H_{c1}}{H_{c2}}$ [192]. H_{c2} was obtained by extrapolating the curves in Figure 4.11 to T_c = 20 K, and H_{c1} was measured as the field from which the magnetic hysteresis curve starts to deviate from linearity. The calculated effective κs are shown in Table 4.4. κ follows the same trend as microstrain. This implies that κ is also affected by disorder. J_c at 20 K and 5 T versus α_1 is shown in the bottom panel of Figure 4.14. A linear relationship can be observed. J_c

(20 K, 5 T) increases with α_1. At self-field, the inter-flux-line spacing (d) tends to infinity. According to the Dew-Hughes model [18], all the defects act as point pinning centres at zero field, and the self-field J_c linearly increases with H_{c2} and decreases with κ^2. The self-field J_c is also proportional to the connectivity [192]. We define another combined parameter, $\alpha_2 = A_F \frac{H_{c2}}{\kappa^2}$, to represent the total influence of H_{c2}, κ and A_F on the self-field J_c. The self-field J_{c0} at 20 K is shown against α_2 in the top panel of Figure 4.14. J_{c0} linearly increases with α_2. From the above analysis, we can see that J_c is mainly affected by the disorder and the connectivity. The former influences J_c via H_{c2} and κ. As disorder increases, both H_{c2} and κ increase. However, the increased H_{c2} and the increased κ change J_c in opposite directions. J_c increases with H_{c2} and decreases with κ. Since the magnitude of the variation in H_{c2} in the studied samples is larger than that of κ, H_{c2} plays more important role on J_c than κ. The analysis above also shows that H_{c2} affects the high-field J_c and the self-field J_c by different factors. The high-field J_c is proportional to H_{c2} by $J_c \propto H_{c2}^{3/2}$, while the self-field J_c is proportional by $J_c \propto H_{c2}$. It is clear that H_{c2} has more impact on the high-field J_c than on the self-field J_c. Although sample A has a lower connectivity than the reference sample, its higher H_{c2} can increases the high-field J_c over the value of the reference sample. Due to the lesser influence of H_{c2} on the self-field J_c, H_{c2} in sample A is not high enough to induce its self-field J_c to exceed J_{c0} in the reference sample. This is the reason why a crossover is observed between the J_c curves of the reference sample and of sample A. As the Mg excess is increased, the connectivity is improved until x = 1.15, while H_{c2} increases and reaches its maximum at x = 1.1. The increased connectivity and H_{c2} will enhance J_c for all fields. Sample C has the best connectivity, and its H_{c2} is just slightly lower than the maximum value in sample B. Therefore, sample C exhibits the best J_c performance for both low fields and high fields. It is interesting to note that sample C also has an

enhanced T_c. The combination of these excellent superconducting properties in sample C should clearly be attributed to optimization of the nominal Mg/B ratio. The optimized Mg/B ratio equal to 1.15:2 significantly reduces the vacancies caused by Mg deficiency or B deficiency, and correspondingly reduces remnant B or remnant Mg. This leads to lower interband scattering and higher connectivity. Therefore, T_c and J_c for all the fields can be simultaneously improved. In addition, the SiC dopant still gives the samples a high level of disorder, resulting in a high H_{c2} and J_c at higher fields.

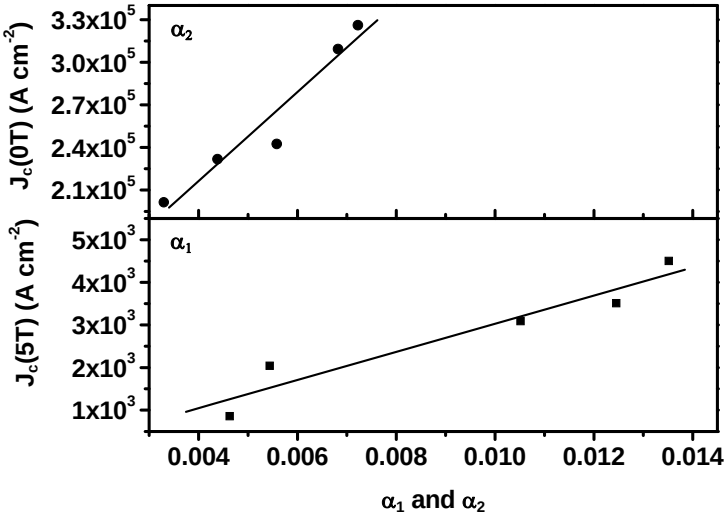

Figure 4.14 J_c at 20 K and 0 T against α_2 (top panel) and J_c at 20 K and 5 T against α_1 (bottom panel).

4.3 Summary

Section 4.1 describes the preparation of undoped Mg_xB_2 samples with x = 0.9, 1, 1.1, 1.2, and 1.3 by solid state reaction. Quantitative X-ray diffraction (XRD) analysis was performed to obtain the lattice constants, microstrain, and weight fraction of impurities using the Rietveld method. It has been found that the fraction of pure MgB_2 phase

increases from x = 0.9 to x = 1.1, and then decreases with further increases in x. The critical temperature (T_c) increases with the lattice parameter *c*. In Mg_xB_2 samples, J_c increases with x to the maximum value at x = 1.1 and then decreases. The higher J_c at x = 1.1 is attributed to the better connectivity caused by smaller amounts of impurities.

Section 4.2 systematically reports on the effects of the nominal Mg/B mixing ratio (x:2) on the superconductivity, Raman spectra, current transport properties, and flux pinning mechanism in MgB_2 with 10 wt.% SiC doping. x varies from 1 to 1.2. It can be seen that compared to MgB_2 without doping, the SiC-doped sample with the stoichiometric nominal Mg/B ratio (1:2) has a significantly increased J_c at high fields. However, its self-field J_c and T_c are depressed. Through the optimization of the nominal Mg/B ratio, we found that the sample with x = 1.15 exhibits the best J_c performance for all fields (0 – 8.5 T), including the self-field, and its T_c is higher than for the sample with x = 1. The enhancement of J_c is attributed to the improved connectivity and the increased disorder, both of which were achieved by the optimization of the Mg/B ratio. The optimized Mg/B ratio (1.15:2) also degrades the interband scattering caused by the Mg or B vacancies and in turn, increases T_c.

5 Sucrose ($C_{12}H_{22}O_{11}$) Doping

Carbon has been proved to be an effective dopant element for improving H_{c2} and J_c of MgB_2 superconductor. Tiny carbon particles and carbon nanotubes have shown a strong enhancing effect on the superconducting properties, although agglomeration is still a problem [134, 143, 188, 249]. Carbohydrate is a very good carbon source for C doping into MgB_2. Carbohydrate materials provide elemental carbon above their decomposition temperature, resulting in C substitution for B, which introduces more disorder. This freshly obtained carbon is distributed more uniformly than with carbon nanotubes. Commercial sugar has been used recently as a dopant in MgB_2 because it is cheap and easy to find. This chapter reports the fabrication and superconducting properties of MgB_2 superconductor using sucrose ($C_{12}H_{22}O_{11}$) as the dopant. The lattice parameters, microstrain, T_c, resistivity, and H_{c2} are presented in comparison with undoped reference MgB_2.

5.1 Influence of carbon doping level [250]

5.1.1 Sample preparation

MgB_2 bulks were prepared by the in-situ solid state sintering method. Powders of Mg (99%), amorphous B (99%), and 98% sucrose were used as starting materials to achieve the formula of $MgB_{2-x}C_x$ (x = 0, 0.08, 0.12, 0.2, 0.3, 0.5). Appropriate amounts of sucrose based on the corresponding carbon content were added into the MgB_2. In order

to investigate the effects of sucrose doping on MgB_2 bulks, B powder with a 100 nm particle size was mixed with sucrose with the help of de-ionized water. The slurry was dried in a vacuum oven. After drying, the B powder was coated with a sucrose layer. The thus obtained B and sucrose mixture was mixed with Mg powder. The powder was ground by hand with a mortar and pestle. Appropriate mixtures of these powders were pressed into pellets and sealed in Fe tubes. This packing process was carried out in air. The samples were heated from room temperature to 780°C-1050°C in a tube furnace under Ar atmosphere at ambient pressure with a 5°C/min heating rate, and kept at the set temperature for 1 hour before being furnace cooled to room temperature.

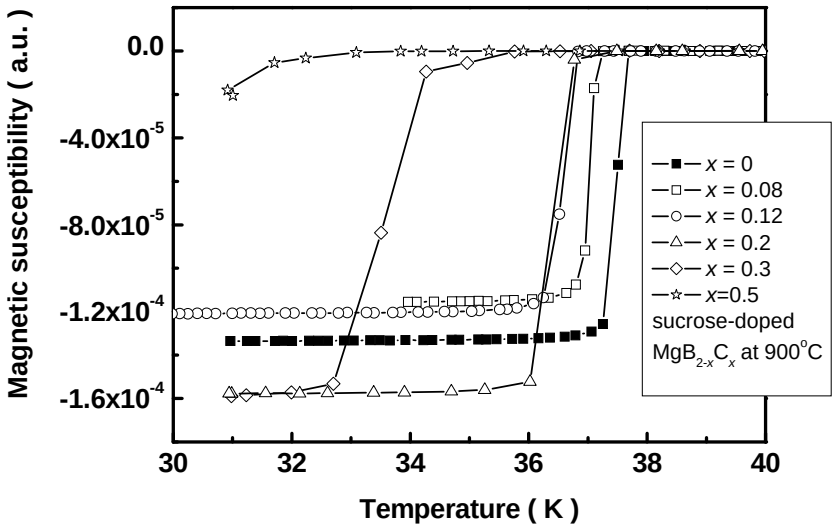

Figure 5.1 Magnetic AC susceptibility for $MgB_{2-x}C_x$ as a function of temperature for different carbon doping content.

5.1.2 Optimization of carbon doping level

Figure 5.1 shows T_c for the doped and undoped samples, as determined by ac susceptibility measurements. T_c noticeably decreases with an increasing sucrose doping

level. The T_c onset for the undoped samples is around 37.7 K. The x = 0.5 doped sample has a T_c of 32.0 K. When x = 0.2, T_c is 36.8 K. The T_c decrease might be a result of increased impurity phases introduced by sucrose doping or as a result of C substitution for B in MgB_2.

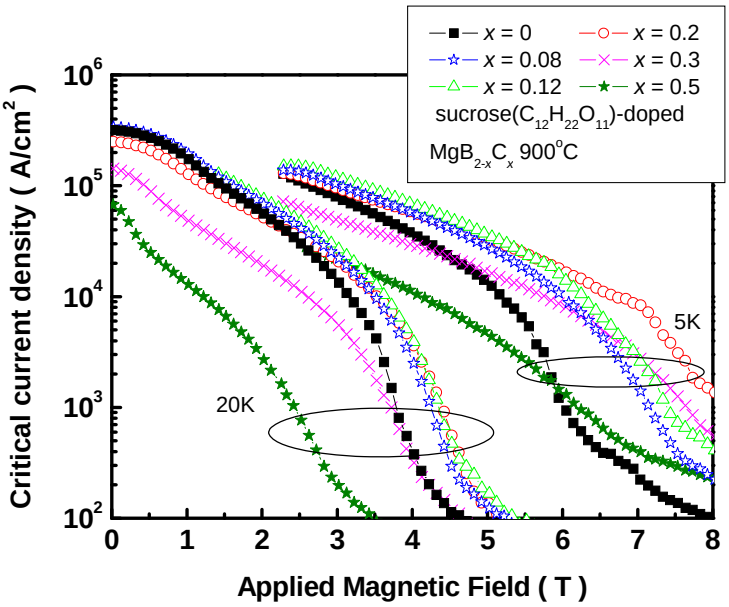

Figure 5.2 J_c as a function of applied magnetic field for all sucrose-doped samples of $MgB_{2-x}C_x$ at 5 K and 20 K.

Figure 5.2 shows the magnetic field dependence of the J_c for these samples. It can be seen the doping has strong effects on the J_c both at 5 K and 20 K. Compared with the undoped sample, samples doped with x = 0.08, 0.12, and 0.2 experience positive effects. At 5 K and 6 T, the x = 0.2 sample shows one order of magnitude improvement. Above the x = 0.2 level, samples such as x = 0.3 and x = 0.5 show less improvement. This can be more clearly shown in Figure 5.3, which contains the J_c performance at 20 K and 4 T. The J_c reaches a peak at x = 0.12. The J_c decrease at higher doping levels is a result of the T_c decrease and also might be related to excessive impurity phase introduced by the sucrose. These impurity phases could block the current path, thus resulting in shrinkage

of the effective current conducting area. Judging from the T_c and J_c performance, we conclude that the doping level of x = 0.2 is the optimized doping level.

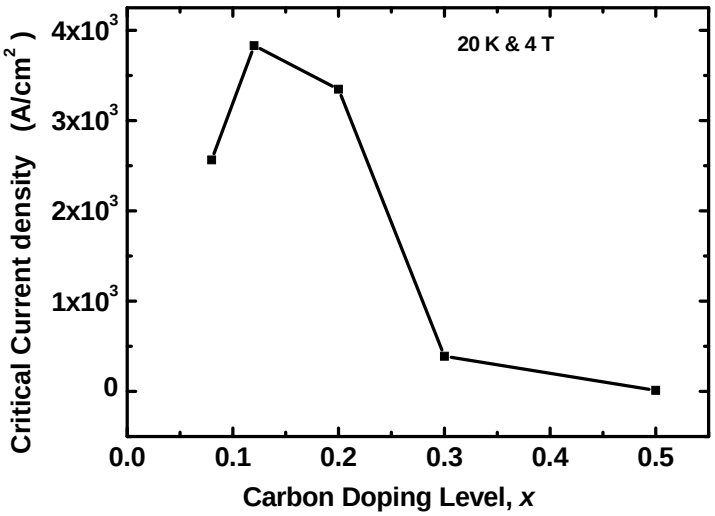

Figure 5.3 Critical current density at 20 K and 4 T as a function of *x*.

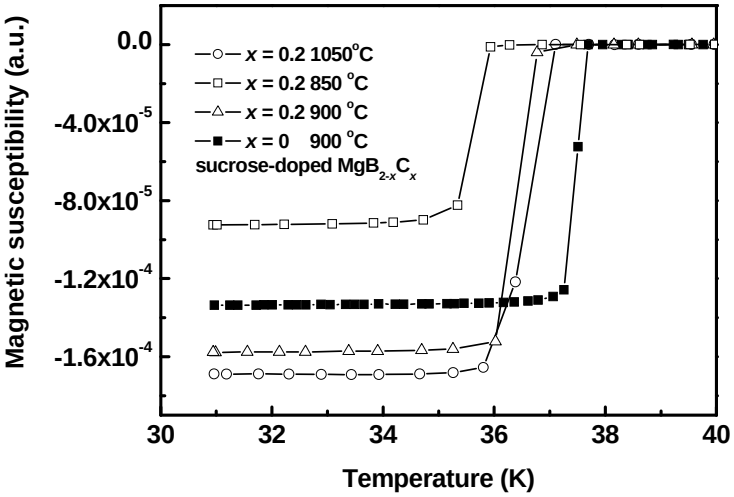

Figure 5.4 Magnetic AC susceptibility as a function of temperature for the pure MgB_2 and sucrose-doped $MgB_{1.8}C_{0.2}$ samples sintered at various temperatures.

5.1.3 Optimization of sintering temperature

In order to optimize the sintering temperature, samples doped at x = 0.2 were sintered at temperatures ranging from 780°C to 1050°C. T_c of these samples is shown in Figure 5.4. A pure sample sintered at 900°C is also included for reference. It was found that the T_c increases with the sintering temperature. This T_c increase is the sign of improved crystallinity.

Figure 5.5 shows the $J_c(H)$ performance for these samples. The sample sintered at 850°C has the best $J_c(H)$ performance. At 20 K, the x = 0.2 sample has higher J_c both at low field and at high field. At 5 K, the sample sintered at 780°C has higher J_c than the 850°C one. Higher sintering temperatures than 850°C results in poorer $J_c(H)$ performance. Judging from the XRD results and $J_c(H)$ performance, J_c is related to the amount of impurity phase and grain boundary pinning. At lower sintering temperatures than 780°C, the doped carbon did not react fully with the MgB_2, so the doping effect of the carbon was not fully utilized, and J_c at higher field is not high. When the sintering temperature is higher than 850°C, the crystal grain size is likely to grow larger due to the thermal effects, which reduce the grain boundary area, thus reducing the grain boundary pinning and decreasing J_c at high field due to the lack of pinning centers, as indicated in reference [251]. The 850°C sintering temperature is a compromise temperature chosen to produce the best overall $J_c(H)$ performance.

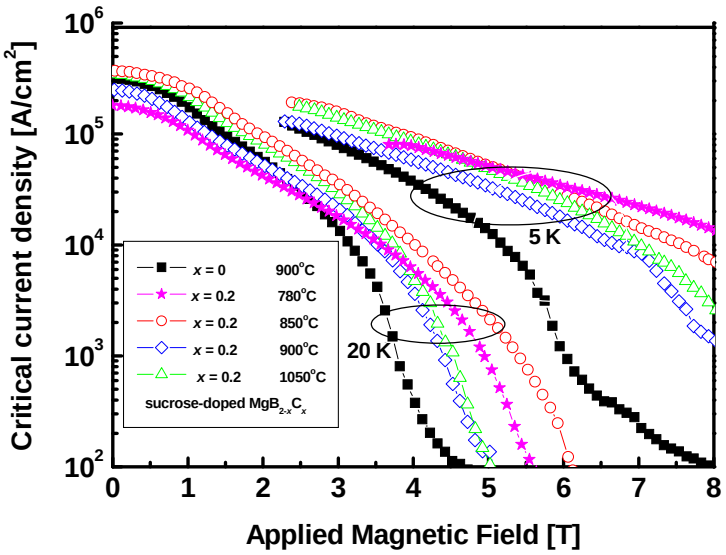

Figure 5.5 $J_c(H)$ curves for pure MgB_2 and sucrose-doped $MgB_{1.8}C_{0.2}$ sintered at various temperatures.

5.2 Analysis of H_{c2} and resistivity [252]

5.2.1 Sample preparation

MgB_2 bulks were prepared by the *in-situ* solid state reaction method. Powders of Mg (99%), amorphous B (99%), and sucrose (98%) were used as starting materials, with the proportions selected to achieve the formula of $MgB_{1.8}C_{0.2}$. B powders and sucrose powders were first mixed together with the help of de-ionized water. The resultant slurry was then dried in a vacuum oven. After drying, the B powder was coated with a sucrose layer. The sucrose-coated B powders were finally mixed with Mg powders, pressed into pellets, and sealed in Fe tubes under air. The samples were heated to the preset temperatures of 850°C and 1050°C in a tube furnace under Ar atmosphere at ambient pressure and kept at the preset temperature for 1 hour before being cooled to room temperature. The sucrose-doped sample sintered at 850°C and the sucrose-doped sample

sintered at 1050°C are defined as sample A and sample B in Section 5.2, respectively. A pure MgB_2 sample without sucrose doping was also fabricated at the sintering temperature of 850°C as a reference sample, by applying the same process.

5.2.2 XRD analysis

Figure 5.6 shows the XRD patterns of the reacted MgB_2 samples with and without sucrose doping. As can be seen, all samples show high-purity MgB_2 phase with MgO as a minor impurity phase. There is a small amount of MgB_4 in sample B, which was sintered at 1050°C. As shown in the inset of Fig. 1, the position of the (002) peak in samples A and B is not changed by sucrose doping, whereas the (110) peak is shifted to a higher 2θ angle. The (110) peak shift is known to be due to the shrinkage of the *a*-axis lattice parameter.

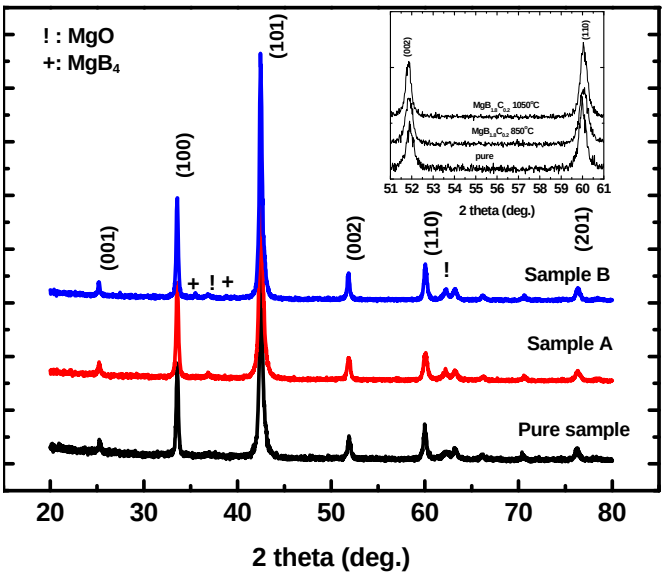

Figure 5.6 Powder XRD patterns of sucrose-doped MgB_2 samples sintered at the temperatures of 850°C (sample A) and 1050°C (sample B). Undoped MgB_2 was sintered

at 850°C as a reference. The inset shows an enlargement of the area containing the (002) and (110) MgB_2 peaks.

Rietveld refinement was performed to analyze the XRD measurements. The refinable parameters include the weight fraction of each phase, the lattice parameters of MgB_2, the grain size, and the degree of microstrain. R_{wp} values for sample A, sample B, and the pure sample are less than 8%, which indicates that the refined results are acceptable. The calculated lattice parameters, grain size, and microstrain are listed in Table 5.1. Lattice parameter *c* is similar for the three samples, while lattice parameter *a* decreases from the pure sample to sample A, and then to sample B. Both the sucrose-doped samples (samples A and B) have smaller lattice parameter *a* values than the ideal value of MgB_2 (3.083 Å). This is consistent with the (110) peak shift mentioned above. The reduced *a* indicates that carbon atoms have replaced boron atoms and/or been squeezed into the MgB_2 lattice as interstitial atoms. It can be seen from Table 5.1 that sample A shows higher strain than the pure sample. Comparing the microstrains of samples A and B indicates that a higher sintering temperature will reduce the microstrain due to the improvement of crystallinity.

Table 5.1 Parameters and properties for all samples.

Sample	Lattice Parameters (Å)		Microstrain (%)	Grain size (Å)	T_c (K)	ρ_{40k} (μΩcm)	ρ_{300k} (μΩcm)	A_F	ρ_{norm}
	a	*c*							
Pure sample	3.085	3.522	0.136	284	38.05	36.11	71.92	0.204	1.008
Sample A	3.079	3.522	0.184	312	37.17	54.51	105.9	0.142	1.061
Sample B	3.080	3.524	0.064	285	37.37	63.04	125.21	0.117	1.014

The XRD refinement shows similar grain sizes in the three samples, although sample A has a slightly larger grain size than the other two. SEM images for the pure sample and sample A are presented in Figure 5.7(a) and (b), respectively. It can be seen that the grain sizes in the two figures are similar, which is in agreement with the XRD refinement results. The pure sample shows a granular microstructure, while the sucrose-doped sample seems to show a change from the granular microstructure to a linear microstructure. This indicates that the sucrose doping has influenced the microstructure of MgB_2.

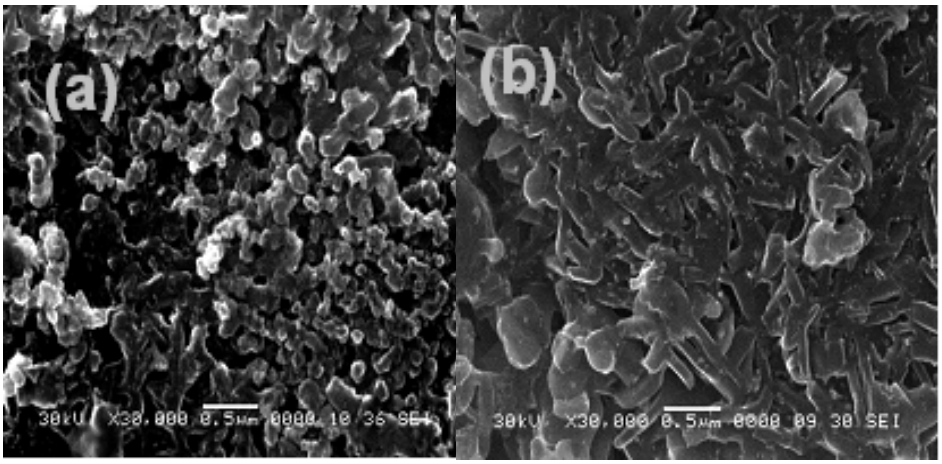

Figure 5.7 SEM images of undoped (a) and sucrose-doped (b) MgB_2 samples.

5.2.3 Resistivity and H_{c2}

The resistivity (ρ) results are shown in Figure 5.8. It can be observed that the two sucrose-doped samples have higher resistivities than the undoped one. The values of ρ_{40K} and ρ_{300K} were collected from Figure 5.8 and are listed in Table 5.1. The pure sample exhibits the smallest ρ_{40K} and ρ_{300K}. With increasing sintering temperature for the doped samples, both ρ_{40K} and ρ_{300K} increase. The increased ρ in the sucrose-doped

samples also indicates increased impurity scattering as a result of C substitution for B and/or C diffusion in the MgB_2 lattice as interstitial atoms. That trend is consistent with other C source doped samples [171, 253, 254]. The calculated A_F is displayed in Table 5.1. It can be seen that the A_Fs of samples A and B are smaller than that of the pure sample, indicating poor connection and high intragrain scattering in samples A and B. The existence of MgB_4 is respossible to the lower A_F in sample B. The poor connectivity and high intragrain scattering are responsible for the high resistivity. ρ_{40K} is plotted against A_F in Figure 5.9(a). It is clear that ρ_{40K} linearly decreases with A_F. Figure 5.9(b) shows the correlation between T_c and the normalized resistivity (ρ_{norm}= $\rho_{40K}/(\rho_{300K} - \rho_{40K})$) [192]. A good linear relationship can be observed. This further indicates that the connectivity and intragrain scattering are responsible for the variations in the resistivity and the transition temperature in the studied samples.

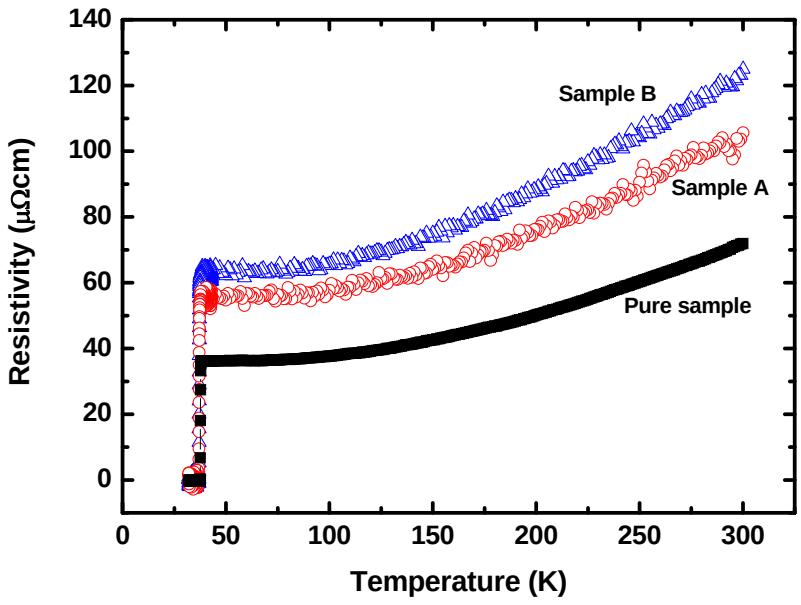

Figure 5.8 Resistivity as a function of temperature for the undoped and doped samples.

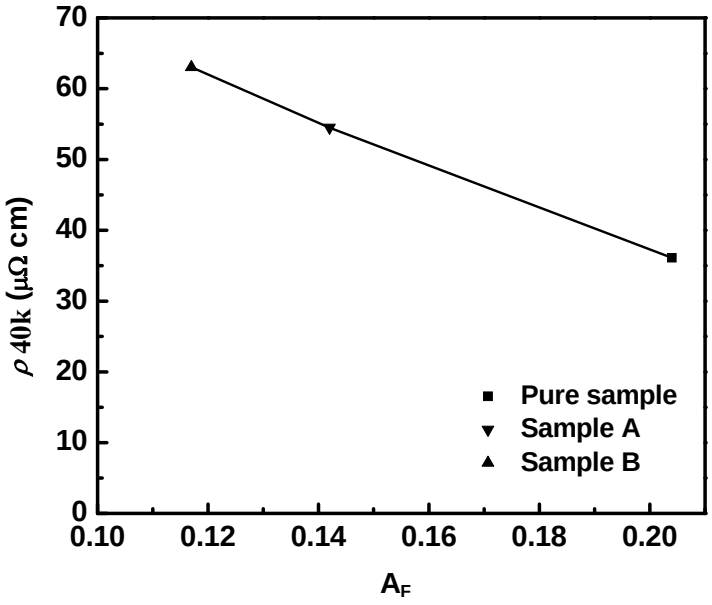

(a)

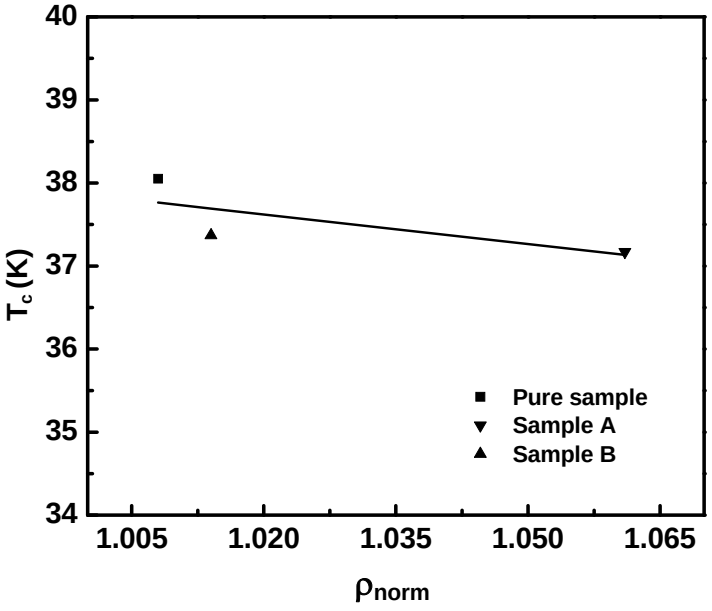

(b)

Figure 5.9 ρ_{40K} vs. A_F (a), and T_c vs. ρ_{norm} (b).

Figure 5.10 demonstrates the normalized temperature dependence of the resistive H_{c2}. It can be seen that H_{c2} has concave temperature-dependence curves. As the temperature increases, H_{c2} decreases. Compared to the pure sample, the two sucrose-doped samples

have higher H_{c2}. According to $H_{c2} = \Phi_0/(2\pi\mu_0\xi^2)$, where ξ is the coherence length, Φ_0 the superconducting flux quantum, and μ_0 the magnetic permeability, H_{c2} is determined by ξ. H_{c2} increases as ξ decreases. Since ξ increases with the mean free path, all the factors influencing the mean free path will change ξ and, in turn, change H_{c2}. There are two major influences that reduce the mean free path. One is the lattice distortion; the other is the scattering from substituting atoms and/or diffused atoms. The former can be estimated from the microstrain, while the latter can be represented by the lattice parameters, especially the *a* parameter.

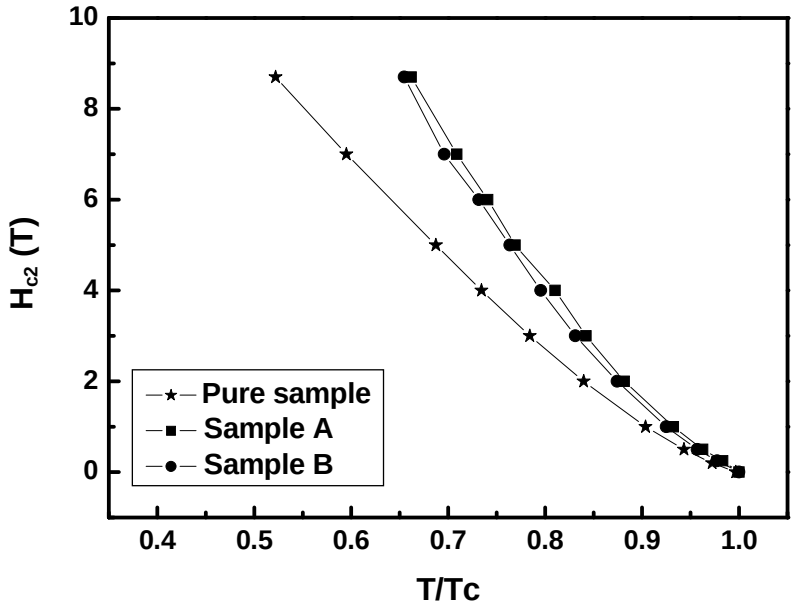

Figure 5.10 Temperature dependence of normalized H_{c2} for the undoped and doped samples.

H_{c2} at $T/T_c = 0.7$ against microstrain and lattice parameter *a* is shown in Figure 5.11(a) and (b), respectively. A clear correlation between H_{c2} and microstrain could not be observed in Figure 5.11(a). However, it can be seen from Figure 5.11(b) that there is a very good linear relationship between H_{c2} and *a*. This strongly indicates that the

scattering from the substituting and/or diffused C atoms is the major source of increased H_{c2}.

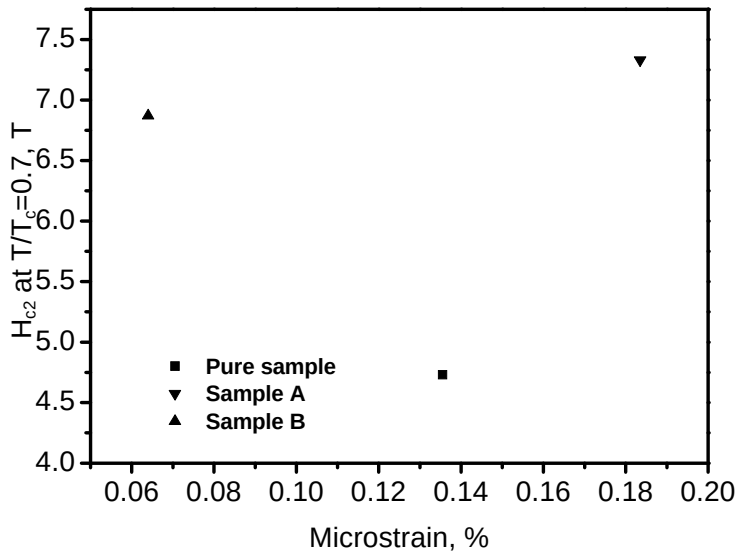

(a)

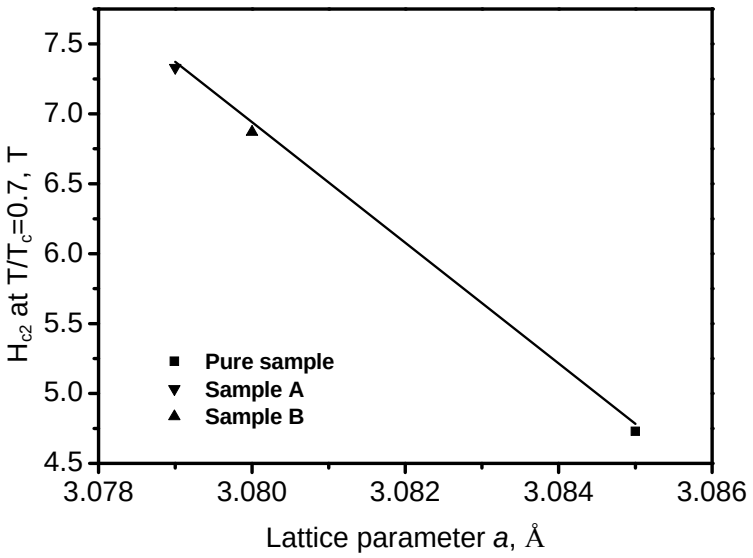

(b)

Figure 5.11 H_{c2} vs. microstrain (a), and H_{c2} vs. lattice parameter *a* (b).

5.3 Summary

In this chapter, MgB_2 bulks are fabricated with/without sucrose doping. The effects of sucrose as a C source on T_c, H_{c2}, and resistivity are investigated. Improved $J_c(H)$ performance is found in sucrose doped MgB_2 superconductor. T_c is reduced by the doping, but can still remain reasonably high (above 34 K at doping levels less than x = 0.2). H_{c2} and H_{irr} both shift towards higher field. It is found that sucrose doping results in a small depression in T_c and high resistivity, while H_{c2} performance is improved. The best performance is shown in the sucrose-doped sample sintered at 850^{o}C. The reason for the enhancement of H_{c2} is likely to be disorder caused by C substitution for B and/or diffusion of C atoms in the MgB_2 lattice as interstitial atoms. This work has opened up a way of improving MgB_2 superconducting properties by doping with a carbohydrate such as sucrose.

6 Co-doping with Nanosized TiO_2/SiO_2 Particles

Since the particular amount of O_2 might play a very important role on J_c improvements, metallic oxides have been attracting more attention than other possible dopants. It has been noted that, under low magnetic field, J_c will be improved by TiO_2 doping, while SiO_2 doping can play a role under high magnetic field [255]. These results particularly attracted our interest towards co-doping with TiO_2 and SiO_2. In this chapter, we report on a systematic study of the effects of the addition of nanoparticle TiO_2 coated with SiO_2 [224, 256].

6.1 Sample preparation

MgB_2 bulks were prepared by the in-situ method. Powders of Mg (99%) and amorphous B (99%) were used as starting materials. The amorphous boron powder was dried for 9 days in an oven at 120^{o}C before mixing with Mg powder. In order to investigate the effects of doping on MgB_2 bulks, we added TiO_2 nanoparticles (15 nm) with a purity of 99.7%. This TiO_2 powder was surface-modified by 5-10% SiO_2. The ratios of TiO_2/SiO_2 to MgB_2 (hereafter termed the doping ratios) were 0, 5, 10, and 15 wt%. The powders were well ground and pressed with a 5 ton press into stainless steel tubes with 10 mm outer diameters and 7 mm inside diameters. This packing process was carried out in air. The samples were heated from room temperature to the sintering temperature, which varied from 650 ^{o}C to 950 ^{o}C for different samples, in a tube furnace under Ar

atmosphere at ambient pressure, and kept at the sintering temperature for 1 hour. The samples were then furnace cooled to room temperature.

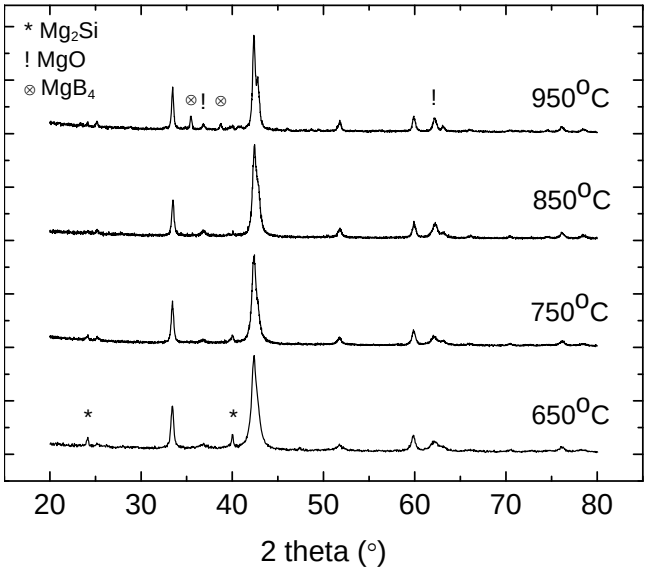

Figure 6.1 Powder XRD patterns of a doped sample (5wt% TiO_2) at various sintering temperatures.

6.2 XRD analysis

Figure 6.1 shows the XRD patterns of a doped sample (5 wt% TiO_2) sintered at temperatures varying from 650 ^oC to 950 ^oC. It can be seen that all the major peaks of the MgB_2 hexagonal structure (space group P6/mmm) can be identified, indicating that the samples mainly consist of the desired MgB_2 phase. Besides MgB_2, the impurity MgO exists in all the samples. MgO impurities could be formed by the reaction of Mg and oxygen during the sintering process. The reacting oxygen could have been introduced from the air trapped in the tubes and from oxygen in the starting boron powder. In addition, Mg_2Si peaks are clearly present at 650 ^oC and 750 ^oC. For the sintering temperature of 850 ^oC, the peaks from the Mg_2Si become weak. This result

indicates that SiO_2, which was used as a coating on TiO_2, had reacted with Mg to form Mg_2Si at low temperature. There are no XRD peaks corresponding to TiO_2 and TiB_2. For the sintering temperature of 950 ^oC, MgB_4 is detected. MgB_4 exists due to a deficiency of magnesium, which is caused by evaporation of the magnesium during the high temperature sintering process.

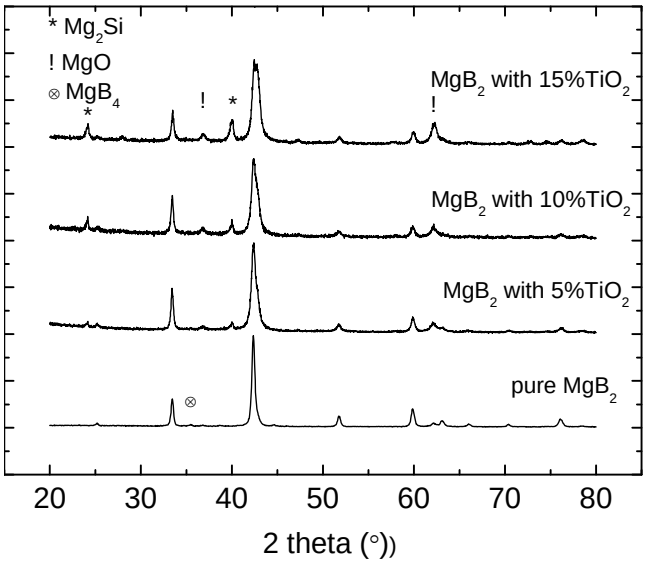

Figure 6.2 Powder XRD patterns of MgB_2 samples with various doping ratios sintered at 750 ^oC.

Figure 6.2 shows powder XRD patterns of MgB_2 samples sintered at a temperature of 750 ^oC with various doping ratios of TiO_2/SiO_2 to MgB_2. MgO is the major impurity in all the samples. As the doping ratio increases from 0 wt% to 15 wt%, the amount of MgO increases. This can be attributed to a reaction between the Mg precursor and the oxygen introduced by the TiO_2/SiO_2 dopant. Mg_2Si can be observed in the samples with TiO_2/SiO_2 doping. It is formed by the reaction of Mg and SiO_2. The amount of Mg_2Si seems to increase with increasing doping ratios. In addition, a small amount of MgB_4 appears in the pure MgB_2 sample. There are no peaks corresponding to TiO_2 (or other

Ti-containing compounds). However, energy dispersive x-ray spectroscopy (EDX) shows that the element Ti exists in the bulk samples. It is therefore suggested that the very weak XRD intensity of TiO_2 nanoparticles (as a second phase) is the main reason for the absence of TiO_2 peaks in the XRD patterns.

Table 6.1 Weight fraction of each phase in the samples.

Doping ratio (wt%)	Sintering temperature (^oC)	Weight fraction (wt%)			
		MgB_2	MgO	Mg_2Si	MgB_4
0	750	90.9	5.7		3.4
5	750	81.6	17.3	1.1	
10	750	70.1	20.6	9.3	
15	750	52.3	35.0	12.7	
5	650	90.6	7.4	2.0	
5	850	80.9	19.1		
5	950	60.2	21.7		18.1

The Rietveld method was used to conduct the quantitative phase analysis. The crystal structures of each component are used to represent the pure component phases as input to the Rietveld method. The XRD pattern is decomposed into a superposition of simulated diffraction patterns generated from these crystal structures The intensity coefficients (*f*), lattice constants (*a* and *c*), and the profile parameters are refined to optimize the agreement between the measured diffraction pattern and the simulated diffraction pattern. The calculated weight fraction of each phase in the samples is listed in Table 6.1. It can be seen from Table 6.1 that the weight fraction of pure MgB_2 phase decreases from 90.9 % to 52.3 %, and the MgO fraction increases as the doping ratio of TiO_2/SiO_2 is increased from 0 wt% to 15 wt%. As the sintering temperature rises from

650 ^{o}C to 950 ^{o}C, the fraction of MgB_2 decreases from 90.6 % to 60.2 %, while the fraction of MgO increases from 7.4 % to 21.7 %. Mg_2Si increases as the doping ratio increases from 5 wt% to 15 wt% for samples produced at the sintering temperature of 750 ^{o}C, but a small amount of Mg_2Si also exists in the sample sintered at low temperature (650 ^{o}C). 3.4 % MgB_4 and 18.1 % MgB_4 were found in the pure sample (0 wt%) and the sample sintered at high temperature (950 ^{o}C), respectively.

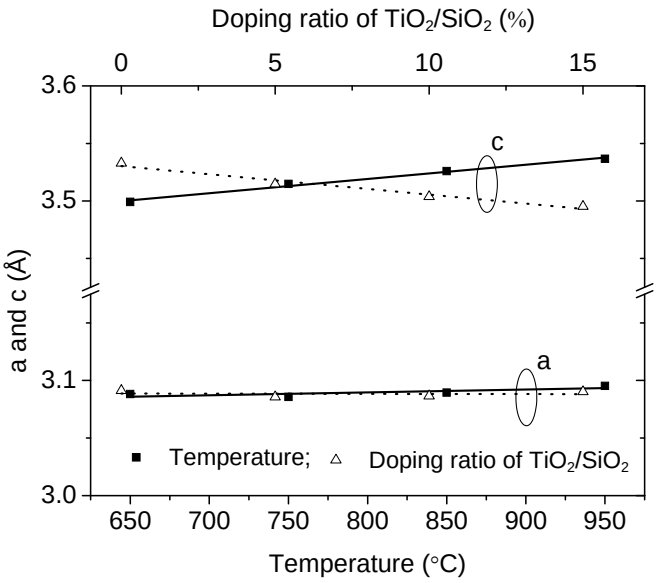

Figure 6.3 Lattice constants of the samples for various sintering temperatures and various doping ratios.

The calculated in-plane lattice constant (*a*) and inter-plane lattice constant (*c*) are plotted in Figure 6.3. The solid square symbols represent the results for various sintering temperatures, while the hollow triangle symbols represent the results for various doping ratios of TiO_2/SiO_2 to MgB_2. The solid lines and the dotted lines indicate the trends of the lattice constants (*a* and *c*) against the sintering temperature and the doping ratio, respectively. It can be seen that the *a* parameter only shows a slight change as the sintering temperature and the doping ratio vary, while the *c* parameter shows a larger

change. This is consistent with the fact that the elastic constant along the inter-plane direction is smaller than that along the in-plane direction.

The constant *c* increases with the sintering temperature in Figure 6.3. This can be explained by the loss of Mg atoms during the high temperature sintering. The melting point of Mg is about 650 ºC. Mg evaporates easily at temperatures over the melting point and reacts with the oxygen. MgO has little influence on the lattice constants because it is mainly located at the grain boundaries. Since the starting Mg powder and B powder were stoichiometrically mixed in this study, the remaining Mg after evaporation was not sufficient to fully react with B to form MgB_2. The loss of Mg atoms increases with the sintering temperature. The deficiency of Mg caused by evaporation will result in vacancies existing in the bulk of the MgB_2, which will relax the MgB_2 lattice and thus enhance the lattice constants. Therefore, the *c* parameter increases with increasing sintering temperature. Figure 6.3 also shows that the *c* parameter decreases with the doping ratio. This can be attributed to the existence of Mg_2Si. Mg_2Si is formed by the reaction of Mg and SiO_2. Since the particles of Mg_2Si are dispersed in the bulk of the MgB_2, the MgB_2 lattice is squeezed. This results in a reduced *c* lattice constant.

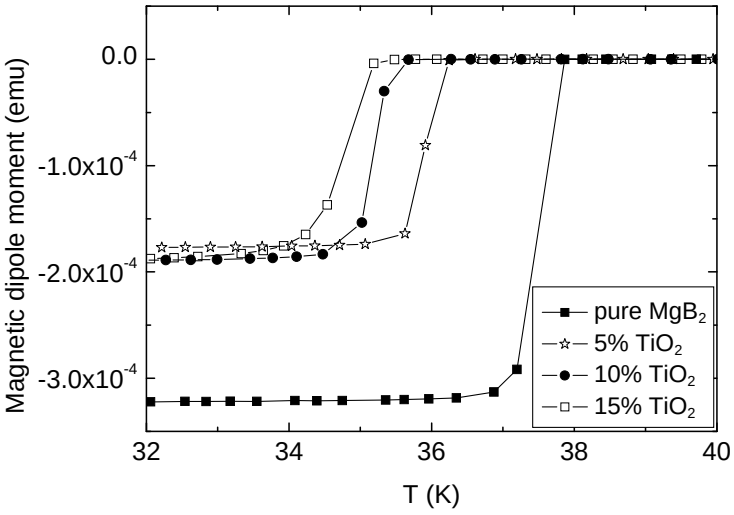

(a)

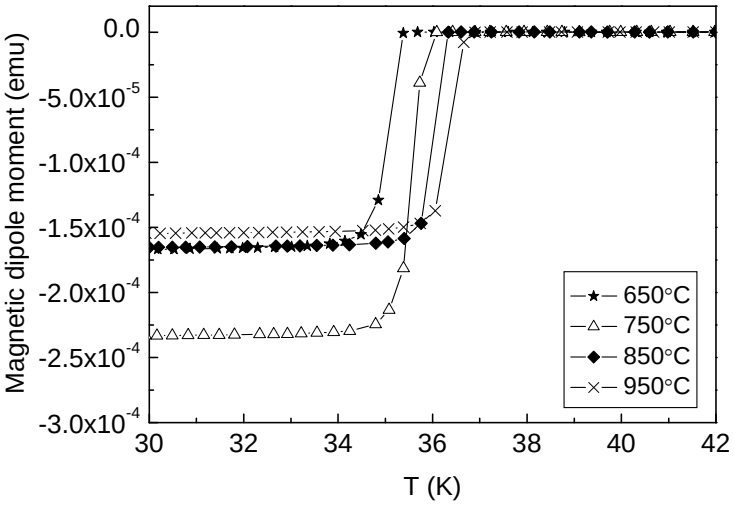

(b)

Figure 6.4 Magnetic susceptibility plotted against temperature for various doping ratios (a) and various sintering temperatures (b).

6.3 T_c and J_c

Figure 6.4 shows the magnetic susceptibility (χ) against the temperature in an applied field of H = 1 Oe for zero field cooled samples. Figure 6.4(a) and (b) gives the results

for various doping ratios and various sintering temperatures, respectively. The magnetic susceptibility for the field cooled condition is not displayed in the figure, since the values are very close to zero. This demonstrates that the flux pinning force in all the samples is quite large. It can be seen that T_c decreases with increasing doping ratio and decreasing sintering temperature.

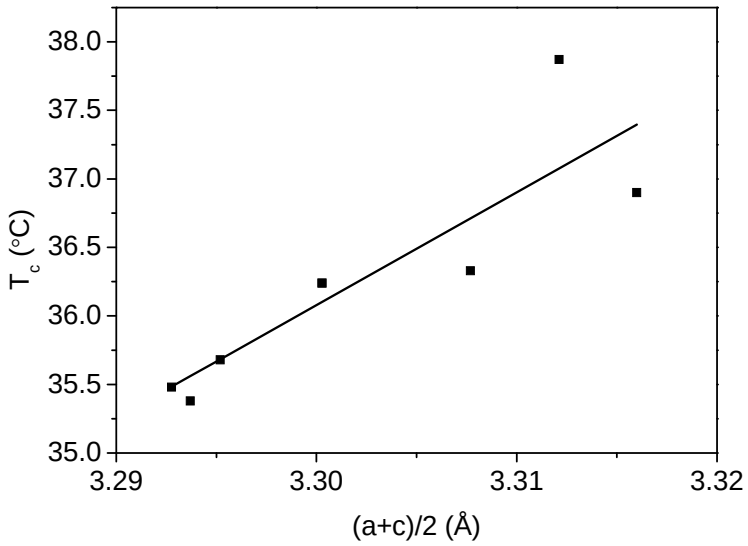

Figure 6.5 T_c as a function of the average lattice constant.

The T_c values were collected from Figure 6.4 and are plotted against the average lattice constant ($(a + c)/2$) in Figure 6.5. The solid line represents the trend line in Figure 6.5. It can be clearly seen that T_c linearly increases with increasing average lattice constant. The contraction of the lattice caused by smaller lattice constants will increase the scattering by the lattice of the superconducting electrons. Therefore, the number of superconducting electrons is reduced, and T_c is suppressed.

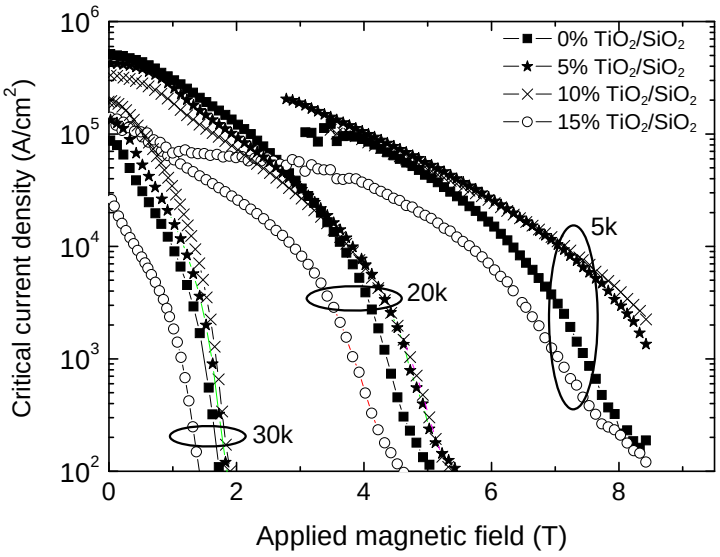

(a)

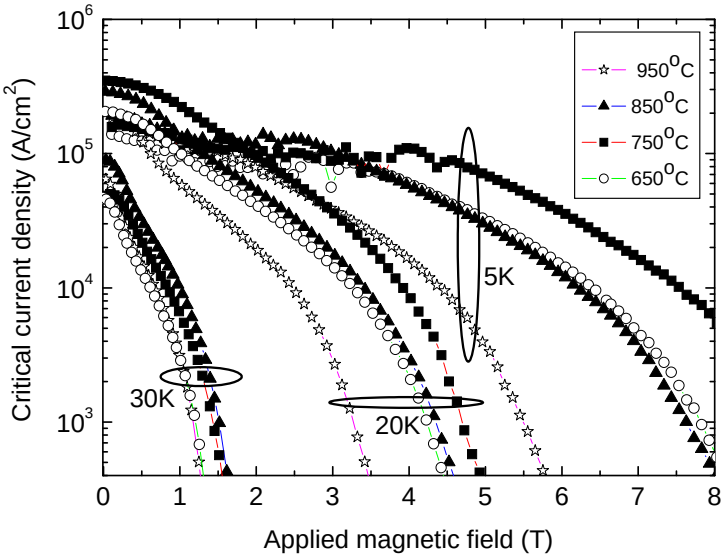

(b)

Figure 6.6 Magnetic field dependence of J_c at the temperatures of 5 K, 20 K, and 30 K for various doping ratios (a) and sintering temperatures (b).

Figure 6.6 (a) illustrates the magnetic field dependence of J_c for 4 different doping levels (0 wt%, 5 wt%, 10 wt%, 15 wt%) at 5 K, 20 K, and 30 K. The sintering temperature is 750 ºC. The results show a significant enhancement of J_c in 5 wt% and 10 wt% TiO_2 doped samples. For example, the J_c value of 3.9×10^3 A/cm^2 at 5 K and 8 T for the

MgB_2 + 10 wt% TiO_2/SiO_2 sample is 18 times that of the pure MgB_2. J_c exhibits the highest value at the doping ratio of 10 wt% for 5 K and 20 K, and at the doping ratio of 5 wt% for 30 K. In addition, there is only slight J_c degradation in self-field for the 5 wt% and 10 wt% samples at 20 K. These findings seem to prove that the flux pinning properties are improved by TiO_2/SiO_2 doping. On the other hand, it can be seen that the J_c values decrease with increasing amounts of TiO_2/SiO_2 addition after the doping ratio is over 10 wt%. MgB_2 + 15 wt% TiO_2/SiO_2 samples at 5 K, 20 K, and 30 K all have bad J_c values. Figure 6.6(b) shows the magnetic field dependence of J_c for 4 different sintering temperatures (650 ºC, 750 ºC, 850 ºC, and 950 ºC) at 5 K, 20 K, and 30 K. The doping ratio is 5 wt%. It is clear that the samples sintered at 750 ºC have the highest J_c for both low applied field and high applied field at 5 K and 20 K, while the sample with the 850 ºC sintering temperature exhibits the best J_c at 30 K.

6.4 Resistivity and H_{c2}

The resistivities, ρ, for the doped and undoped samples sintered at 750^{o}C are shown in Figure 6.7. It can be observed that the resistivity for the doped sample is much higher than for the undoped one. This trend is quite similar to that shown by SiC doped samples.

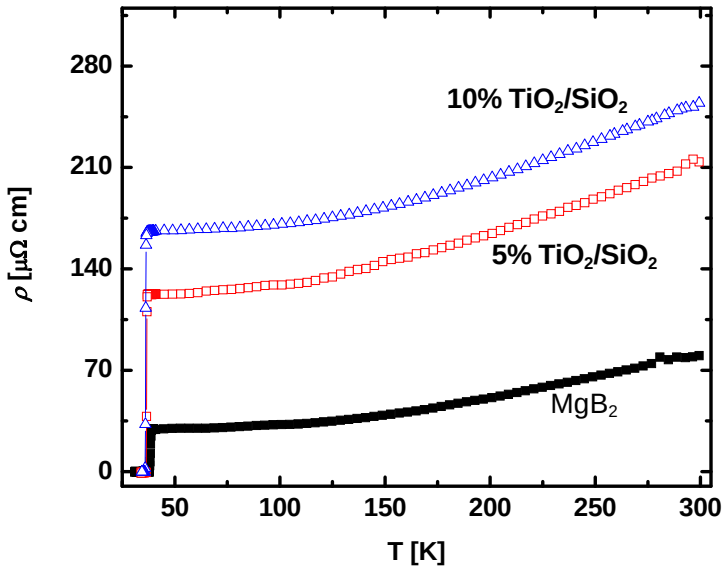

Figure 6.7 Resistivities versus temperature for undoped and doped samples.

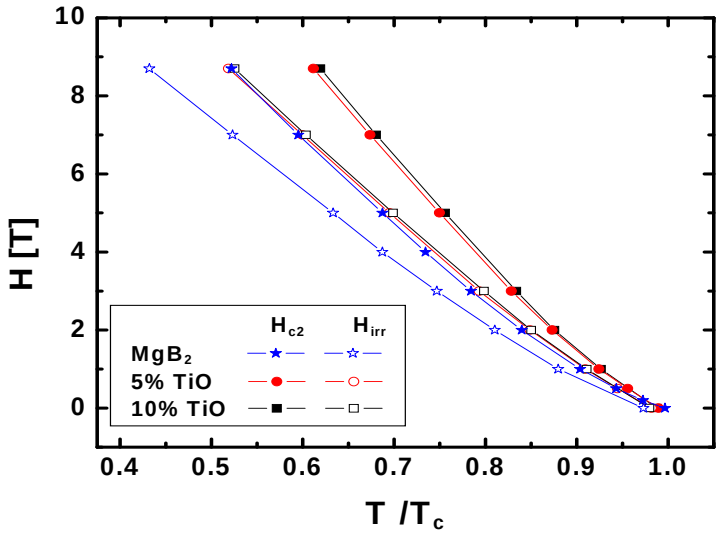

Figure 6.8 Temperature dependence of normalized H_{irr} and H_{c2} for undoped and doped samples.

As ρ increases, H_{c2} and H_{irr} show an increasing trend, as shown in Figure 6.8. The straightforward explanation is that the doped samples are dirty, as the residual resistivity ratio (RRR), defined as ρ(300K)/ ρ(40K), is found in Table 6.2 to also decrease with increasing doping level. Although Klie *et al.* [113] reported that most oxygen doping would result in second phases of MgO or BO_x with large particle size at the grain

boundaries, several other reports [257-259] have revealed that there are nano-$Mg(B,O)_2$ precipitates inside the MgB_2 grains, which have desirable effects on superconducting performance. Our current study on the effects of processing atmosphere on the superconducting properties of MgB_2 has shown that there is a high density of $Mg(B,O)_2$ precipitates and of grain boundaries as a result of oxygen doping. These desirable nanoprecipitates inside the MgB_2 grains result in lattice distortion and shorten the mean free path (ℓ) of the superconducting electrons [257]. Therefore, the coherence length (ξ) is decreased due to the relation: $1/\xi = 1/\xi_0 + 1/l$, where ξ_0 is the value of ξ for the pure superconductor. According to $H_{c2} = \Phi_0/(2\pi\mu_0\xi^2)$, H_{c2} will increase as ξ decreases. Both the H_{irr} and the H_{c2} slopes are found to be significantly higher for the doped samples. The best performance is shown in the 10% TiO_2/SiO_2 doped sample, which has a large FWHM of the (110) peak for the MgB_2 phase and a large ρ value at 40 K, as shown in Table 6.2. This provides direct evidence that the lattice defects and precipitates are essentially beneficial for enhanced H_{irr} and H_{c2} in MgB_2 bulks.

Table 6.2 Resistivity properties.

Samples	Sintering conditions	ρ_{40K} (μΩcm)	ρ_{300K} (μΩcm)	Δρ (μΩcm)	RRR
Undoped MgB_2	750°C 1h	30.1	79.7	49.6	2.7
MgB_2 + 5% TiO_2/SiO_2	750°C 1h	122	215	93.1	1.8
MgB_2 + 10% TiO_2/SiO_2	750°C 1h	166	252.3	86.8	1.5

6.5 Summary

Bulk MgB_2 doped with nanoparticle TiO_2, which has been surface-modified by 5-10% SiO_2, was prepared by solid state reaction. It has been found that T_c increases with the

lattice constants. J_c is affected by the doping ratio and the sintering temperature. J_c exhibits the highest values at the doping ratio of 10 wt% at 5 K and 20 K, and at the doping ratio of 5 wt% at 30 K when the sintering temperature is fixed at 750 ^oC. When the doping ratio is fixed at 5 wt%, the samples with the sintering temperature of 750 ^oC have the best J_c at 5 K and 20 K, while the sample with the sintering temperature of 850 ^oC exhibits the highest J_c at 30 K. In addition, it has been found that the additive TiO_2/SiO_2 nanoparticles result in small depressions in T_c, while the H_{c2} and H_{irr} performances are improved. The enhancement of H_{c2} and H_{irr} can be attributed to the existence of precipitates induced by the TiO_2/SiO_2 doping.

7 Processing Atmosphere

Enormous efforts have been made to improve J_c in MgB_2 through chemical doping [115, 143, 155, 162, 168, 171, 188, 249]. Among these doping elements, oxygen represents a special case, as nearly all types of MgB_2 materials have been sintered in a protective atmosphere such as Ar. It has been well demonstrated that the superconducting properties of MgB_2 are highly sensitive to the processing conditions, which include the precursor powders, the heating rate, and the processing temperature and duration, as well as the atmosphere. Oxygen alloying into MgB_2 reduces T_c, but improves flux pinning in thin films [259-262] and bulks [257]. Recently, Senkowicz *et al.* have reported the effects of different amounts of exposure to air during the ball-milling process for pre-reacted MgB_2 powder, which was used to prepare MgB_2 bulk or wires by the *ex situ* method [263]. In this case, the effects of atmosphere are limited to effects on the mature MgB_2 at room temperature. As for the *in situ* process, there has been no systematic study of the effects of processing atmosphere on the superconducting properties of MgB_2 during high temperature fabrication. It is expected that the processing atmosphere would have a more significant effect on the superconducting properties in the *in situ* processed samples, as reactive components in the atmosphere can easily participate in the MgB_2 formation process from a mixture of Mg and B powders.

Our research group has proposed a dual reaction model to evaluate and explain the effect of a broad range of dopants in MgB_2 [129]. According to this model, the optimal

doping effect can be achieved when the reaction or substitution between the dopants and precursor components takes place simultaneously with the MgB_2 formation. Motivated by this finding, in this chapter three different purity argon atmospheres have been adopted to process MgB_2 pellets using the reaction *in situ* method, in order to examine the effects of oxygen doping. This will create a condition where the MgB_2 formation and the reaction between oxygen/moisture and the precursor powder components take place at the same time. The results in Section 7.1 show that a modest oxidising atmosphere, provided by welding grade argon, gives a rise to a noticeable enhancement in J_c performance in high fields, accompanied by a small decrease in T_c and an increase in resistivity. Section 7.2 shows the effect of the optimal sintering time in flowing welding grade Ar atmosphere.

7.1 Optimal processing atmosphere

7.1.1 Sample preparation

MgB_2 pellet samples were prepared by a reaction *in-situ* method. Powders of magnesium (99%) and amorphous boron (99%) with the stoichiometry of MgB_2 were well mixed. The mixed powder was pressed under a pressure of 5 tonnes in a hydraulic press, packed into a Fe tube without sealing, heated at a preset rate to 700^{o}C, and then held for 30 minutes in flowing Ar. The Fe tube was only used as sample holder. It had a diameter of 12 mm and a length of 20 mm, with the two ends open so Ar could freely flow through the samples. This was followed by furnace cooling to room temperature. Samples from the same batch were heat-treated under three different Ar gases: ultra-high purity Ar (UA), high purity Ar (HA), and welding grade Ar (WA). The total

impurities are given by the specifications of the gas supply as 10 ppm, 30 ppm, and 50 ppm for UA, HA, and WA, respectively. Approximately half of these impurities are oxygen and moisture.

7.1.2 Superconducting properties

Table 7.1 lists the basic parameters, including the T_c, the resistivity, ρ, at 300 K and 40 K, the residual resistivity ratio (RRR), and the *a*-axis and *c*-axis lattice parameters for the samples treated under the three Ar atmospheres. The lattice parameters show little difference among the three samples. The T_c for the WA sample is lower than for the UA and HA samples by 0.5 K. The resistivity values for the three samples are in the range of 30 μΩcm to 70 μΩcm, the same as what has been reported for pure MgB_2 bulk [112, 151]. However, a clear trend exists for the resistivity in relation to the processing atmosphere, that is, a sample has a lower resistivity when processed in high and ultra-high purity Ar than in welding grade Ar.

Table 7.1 Basic parameters of samples sintered under different Ar atmospheres at 700°C for 30 min.

Sample	T_c (K)	ΔT_c (K)	ρ_{40K} (μΩcm)	ρ_{300K} (μ Ωcm)	RRR	*a* (Å)	*c* (Å)	FWHM (101)	FWHM (110)
UA	37.6	0.9	32.9	68.5	2.08	3.083	3.520	0.31	0.37
HA	37.6	0.9	29.4	61.1	2.08	3.083	3.527	0.31	0.36
WA	37.1	0.9	38	72.3	1.90	3.081	3.525	0.35	0.41

From Table 7.1, it can be seen that there is little change in the lattice parameters for the three samples UA, HA, and WA. The MgO content shows some increase from 8.2% for

the UA to 9.4% for the HA and 10.7% for the WA sample. Since the three samples were formed from the same precursor powders the increase in MgO is attributable to the oxidising components such as O_2 and H_2O from the processing atmosphere. In addition to the MgO, there is another impurity phase, MgB_4, which can be detected in the HA and UA samples but is under the detection limit for WA.

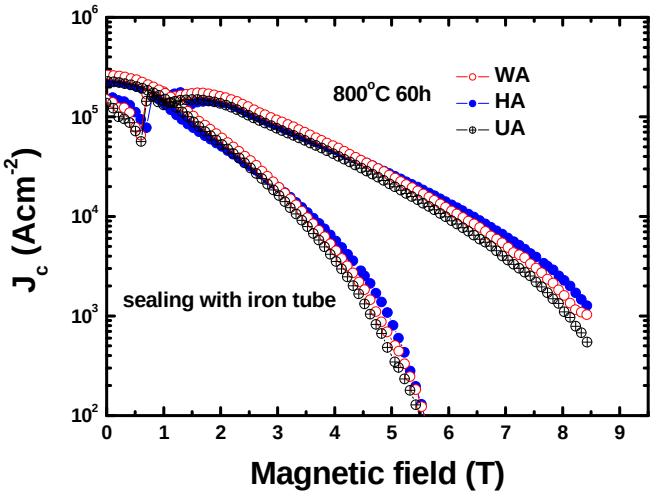

Figure 7.1 The J_c – H dependence at 5 K and 20 K for MgB_2 pellet samples processed at 800 ^oC under three different Ar atmospheres in sealed Fe tubes.

It is a common practice to use an Fe tube to seal a sample during high temperature processing. It is important to examine the effects of the different atmospheres when the Fe tube is sealed. Figure 7.1 shows the $J_c(H)$ curves for the MgB_2 samples, UA, HA, and WA, at 5 and 20 K, which were fabricated in the three different Ar atmospheres at 800 ^oC for 60 hours in an Fe tube sealed at both ends. It is clear that there is no noticeable difference in $J_c(H)$ behaviour for the three samples. As the oxygen diffusion through Fe is rather slow, the sealing of the Fe tube is sufficient to protect the sample from oxidation. From the available data on the oxygen diffusion coefficient in iron: $D_o = 1.3 \times 10^{-}4 \exp(-166 kJMol^{-1}/RT)$ [264]. As the commonly used processing conditions for

MgB_2 are 30 minutes to two hours, the current finding demonstrates that Fe tube sealing can provide very secure protection of MgB_2 from oxidation in large-scale production.

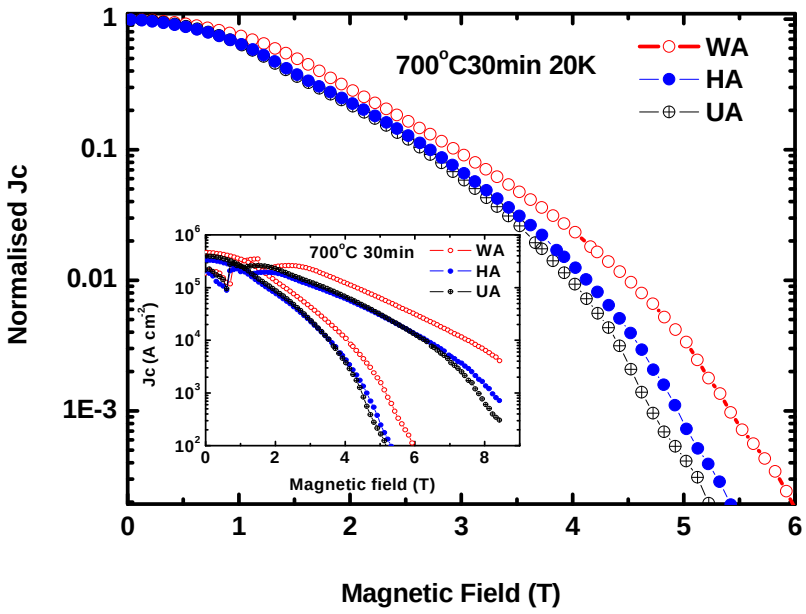

Figure 7.2 Normalised J_c versus H at 20 K for MgB_2 pellet samples processed at 700 °C under three different Ar atmospheres: UA, HA, and WA samples. The inset contains the J_c – H curves at 5 K and 20 K for these three corresponding samples.

Figure 7.2 shows the normalised $J_c(H)$ curves for the MgB_2 samples: UA, HA, and WA at 20 K. It should be noted that the normalised $J_c(H)$ curve for the WA sample processed under welding grade Ar shows a slower drop with increasing field than those for the other two samples, UA and HA. The $J_c(H)$ for the UA and HA samples are consistent with previous reported results on pure MgB_2 materials [151], as the samples in most published works were processed in high purity Ar. In order to avoid possible variation in self-field J_c for the three samples, the $J_c(H)$ behaviour for the three samples is better compared with normalised J_c vs. H. It is clear that the WA sample shows a slower drop in J_c with increasing field than the other two. The H_{irr} for the WA sample was

determined by the criterion of 100 A/cm^2, which is to be found at 6 T on the J_c(H) curve. This is considered to be a high value for undoped MgB_2, although it is lower than for some other dopants such as SiC, which reached an H_{irr} of 7.3 T [115] with about the same sample size as in this work.

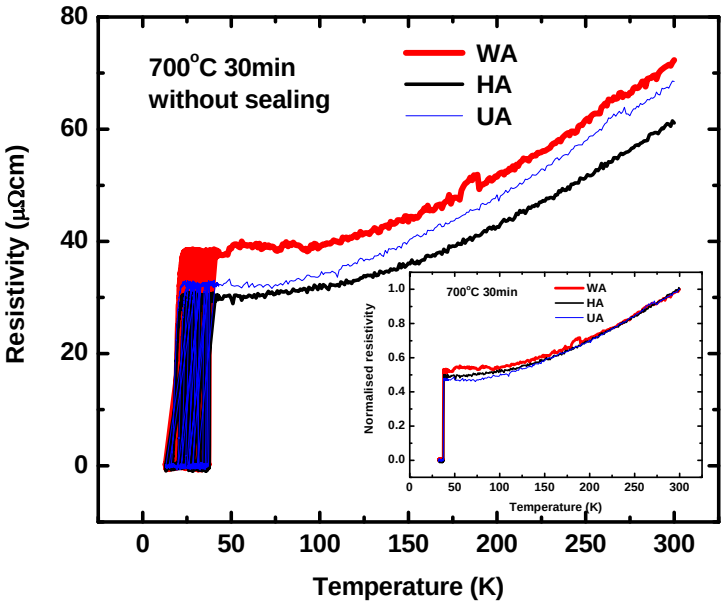

Figure 7.3 Resistivity versus temperature for samples UA, HA, and WA. The inset shows the resistivity normalised to the room temperature resistivity versus temperature.

To consider the mechanism behind the enhancement of J_c at higher fields for the WA sample, it is necessary to examine the phase composition and microstructure of samples treated under different Ar atmospheres. Upon analysis of all the parameters listed in Table 7.1, we can propose that the oxygen doping is responsible for the different J_c(H) performance in fields of the three samples processed under different Ar atmospheres. This argument is supported by the following evidence. Figure 7.3 shows the resistivity-temperature curves for the three samples. The resistivity for WA is larger than for the other two. Although the resisitivity values for UA and HA do not follow the expected

sequence (since ρ of HA is assumed to be larger than ρ of UA), the normalized resistivity (ρ) of WA is larger than that of HA, which is, in turn, larger than ρ of UA, as shown in Figure 7.3. From the resistivity curves under different magnetic fields the H_{irr} and H_{c2} can be derived using the 10% and 90% of transition criteria. The results are shown in Figure 7.4.

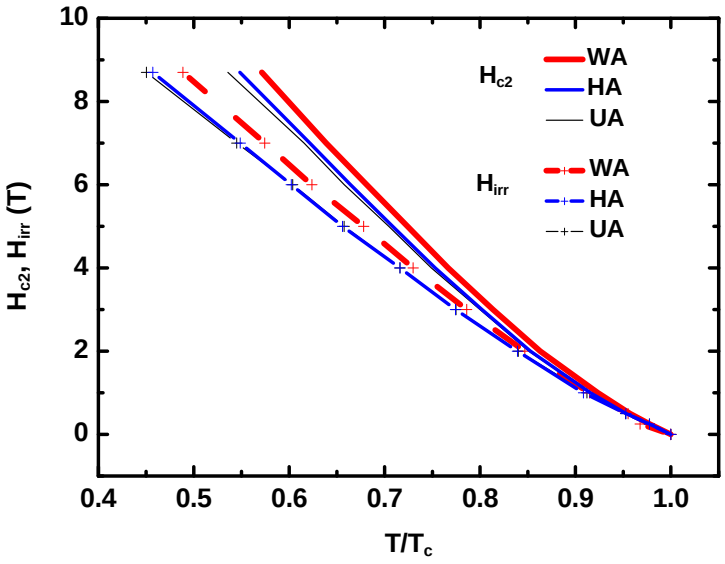

Figure 7.4 The H_{irr} and H_{c2} curves determined from resistivity measurements for the samples UA, HA, and WA.

It is evident that the WA sample has improved H_{irr} and H_{c2} in the limited field regime measured. This improvement in H_{irr} and H_{c2} is quite similar to the case of C-doped samples although it shows a smaller extent of improvement. Secondly, the T_c for WA is decreased by 0.5 K compared to UA and HA. These results suggest that there is scattering as a result of either oxygen incorporation into the lattice or lattice strain caused by inclusions in the grains. Furthermore, the FWHM of the XRD peaks shows the same trend as resistivity and T_c, that is, the WA sample has a larger FWHM, while the UA sample has a smaller FWHM, indicating that the grain size in WA is smaller

than in UA and HA (Table 7.1). It has been established that grain boundaries are effective pinning sites. Thus, the WA sample, owing to the smaller grain size, has stronger pinning than the HA and UA samples. This is further supported by the field-emission SEM and TEM observations.

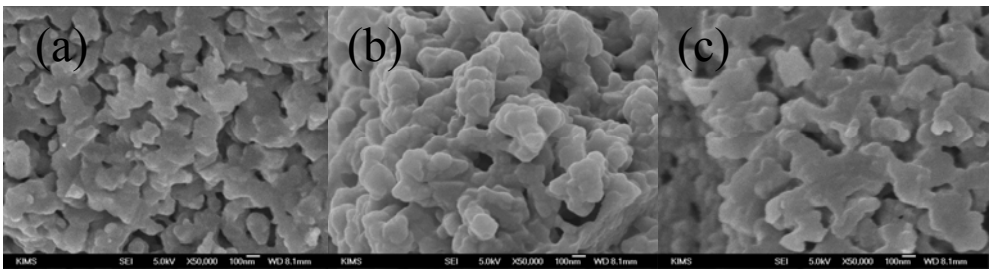

Figure 7.5 FEG-SEM images for samples WA (a), HA (b), and UA (c), which were processed at 700 °C for 30 min.

FEG-SEM images for these three samples are shown in Figure 7.5. It can be seen that the grain size of WA is smaller than that of HA, which is in turn smaller than that of UA. Figure 7.6 shows the TEM images for the samples HA and WA processed under high purity Ar and welding grade Ar, respectively. It is evident that the grain sizes in the WA sample are much smaller than in the HA sample. The grains for sample HA are several hundred nanometers long and approximately 100 nm wide (Figure 7.6(a)), while the WA sample has average grains that are several tens of nanometers wide and up to 100 nm long (Figure 7.6(b)). Furthermore, the WA sample contains a high density of defects such as dislocations and heavy strains in the lattice, as shown in the high resolution image in Figure 7.6(c). The strong contrast variation within the grains shown in (c) is clear evidence of strain in the grains. The strain results in a high density of lattice defects in the grains. To see the defects clearly, the area marked with a black square in Figure 7.6(c) was analysed using Fourier transformation-inverse Fourier transformation

to obtain one-dimensional lattice fringes. The results are shown in Figure 7.6(d). Lattice distortion and a high density of dislocations, as marked with white arrows, are seen in the area. In addition to the white arrows, there is a black arrow in the middle of the image that marks an extra lattice plane. These defects indicate the presence of strain as a consequence of the oxygen alloying.

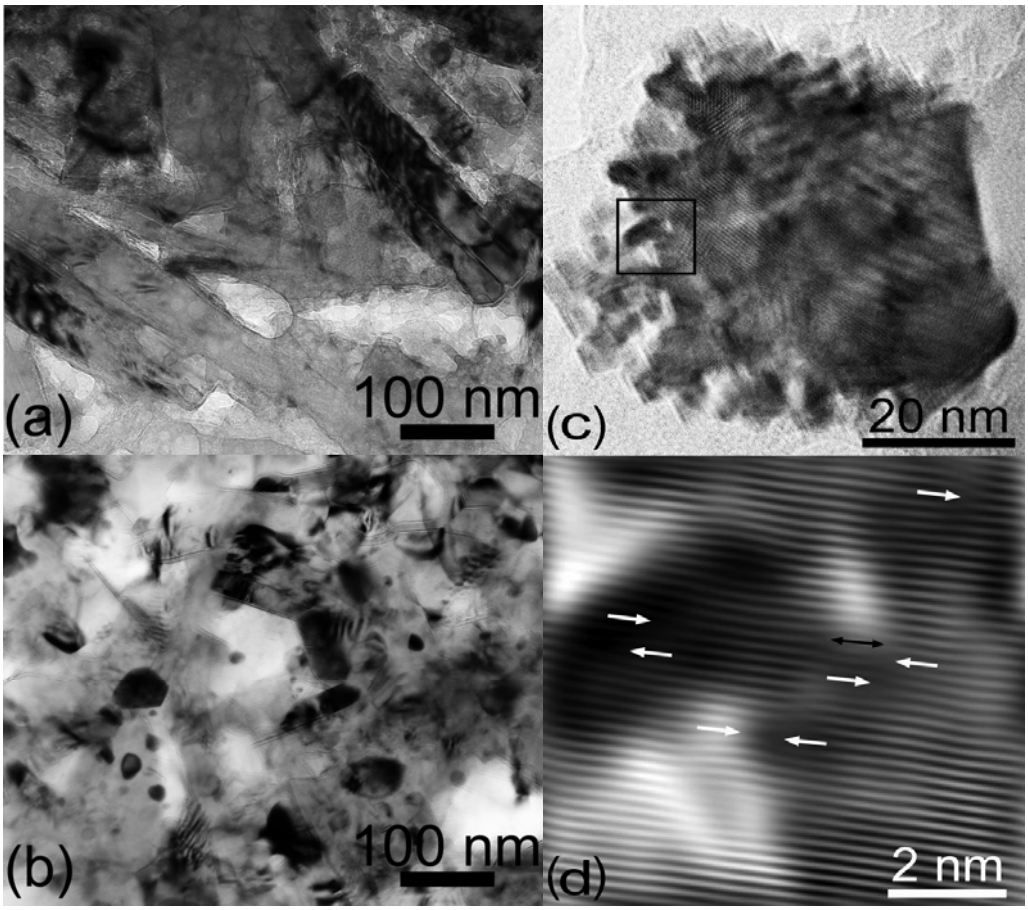

Figure 7.6 TEM images from the samples HA (a) and WA (b), and high resolution TEM images showing the high density of defects in sample WA (c) and the lattice distortion in WA (d) of the marked area in (b). The white arrows mark lattice distortion and the black arrow an extra lattice plane.

According to the dual reaction model proposed by our group for the interpretation of the enhancement in electromagnetic properties in nanoscale SiC doped MgB_2 [129], the optimal doping effect can be achieved when the C substitution and MgB_2 formation take place at the same time at low sintering temperatures. Even for the cases without substitution, for example, Si and silicide doping, because a reaction of Si with Mg takes place during MgB_2 formation, the reaction product Mg_2Si can be easily incorporated into the MgB_2 grains as nano-inclusions. Si and silicide doping have been shown to improve the flux pinning in previous work [162, 265, 266]. Following the dual reaction model, in the present work, the reactive O_2 from the protective atmosphere can be incorporated either within grains as precipitated nano-inclusions or can alloy into the lattice. The latter case has been reported in the form of oxygen alloying at B sites in films [259] and the precipitation of nanometer-sized coherent Mg(B,O) with the same basic structure as MgB_2 [257, 267]. This phase has been found to be unstable and decompose to MgB_2 and MgO as nano-inclusions in oxidising atmosphere [257, 267]. These alloyed phases and nano-inclusions may act as nucleation centres during the formation of MgB_2 to reduce the grain size of the MgB_2. This explains why processing in welding grade Ar atmosphere resulted in small grains. The presence of Mg(B,O) phase or MgO within the grains results in the lattice strains. The high density of defects and strains causes them to act as effective pinning centres, to which the improvement in the high field J_c of the sample processed in welding Ar can be attributed.

7.2 Optimal sintering time in MgB_2 bulk sintered in welding grade Ar [268]

7.2.1 Sample preparation

MgB_2 pellet samples were prepared by a reaction *in-situ* method, which has been previously described in detail. Magnesium (99%) and amorphous boron (99%) powders were well mixed with the stoichiometry of MgB_2. The mixed powder was pressed under a pressure of 5 tons in a hydraulic press, packed into Fe tubes without sealing, heated to 700^{o}C, and then held for 10 minutes, 30 minutes, or 3 hours in flowing welding grade Ar (> 99.995%). The samples sintered for 10 min, 30 min, and 3 h are respectively termed samples A, B, and C in Section 7.2. The reason for the use of the processing temperature of 700^{o}C and the other parameters is because these are optimal conditions to achieve the best $J_c(H)$ performance, based on our previous study [65]. Although heat treatment at 900 ^{o}C or higher can achieve optimal T_c [65, 112, 151, 264], this does not provide optimal conditions for $J_c(H)$ performance [65]. The Fe tubes were only used as sample holders. They had a diameter of 12 mm and a length of 20 mm, with the two ends open so that Ar could freely flow through the samples. The sintering was followed by furnace cooling to room temperature.

7.2.2 XRD analysis

The XRD patterns for MgB_2 samples processed with different sintering times are shown in Figure 7.7. As can be seen, all samples show high-purity MgB_2 phase with MgO as a minor impurity phase. There is a small amount of MgB_4 in sample A. The Rietveld refinement method was used to analyze the XRD measurements. The refinable parameters include the weight fraction of each phase, the lattice parameters of MgB_2, and the microstrain. The calculated results for the refinable parameters are shown in Table 7.2.

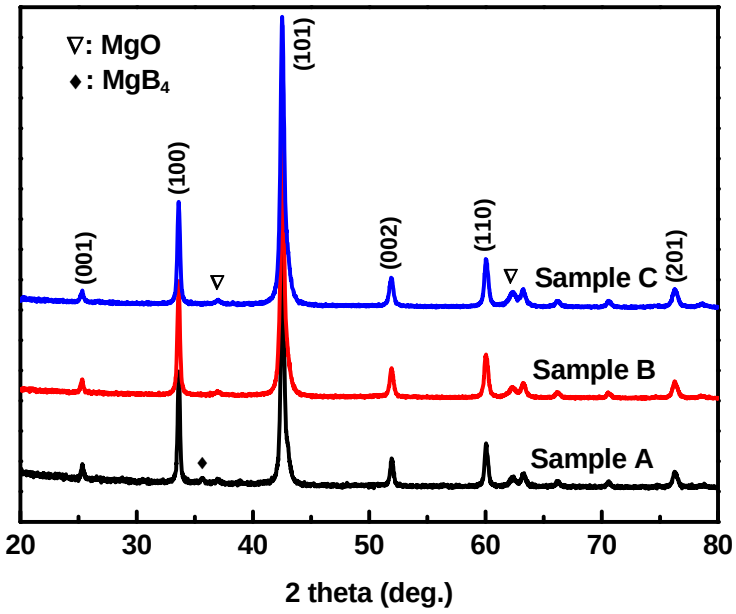

Figure 7.7 Powder XRD patterns of MgB_2 samples.

Table 7.2 Parameters for the three samples.

Samples	Sintering time	MgO (%)	MgB_4 (%)	Lattice parameters	
				a (Å)	c (Å)
A	10 min	4.75	5.82	3.083	3.524
B	30 min	6.44		3.082	3.522
C	3 h	8.5		3.085	3.526

Samples	Microstrain (%)	T_c (K)	ρ_{300K} (μΩcm)	ρ_{40k} (μΩcm)	A_F
A	0.348	37.48	97.55	41.99	0.13
B	0.426	37.09	72.16	37.45	0.21
C	0.456	37.24	122.67	73.59	0.15

From Table 7.2 it can be seen that as the sintering time increases from 10 min to 30 min, lattice parameters *a* and *c* decrease. Lattice parameter *a* of sample B has been reduced below the ideal value (*a* = 3.083 Å). This indicates that oxygen atoms have diffused into

the MgB_2 lattice. They may squeeze into the lattice as interstitial atoms or replace the boron atoms to form $MgB_{2-x}O_x$ precipitates [258], leading to the reduced lattice parameters. Since the diffusion density of the oxygen atoms increases with the sintering time, the lattice parameters decrease from sample A to sample B. However, when the sintering time is further increased, the diffused oxygen atoms saturate, and part of them react with Mg atoms to form MgO after long sintering times (3 hours in sample C). Table 7.2 shows that the MgO fraction increases when the sintering time increases from 30 min to 3 hours. The reaction of the diffused oxygen atoms and Mg atoms reduces the concentration of interstitial oxygen atoms and induces Mg deficiency, both of which result in the increased lattice parameters in sample C, as shown in Table 7.2. T_cs are listed in Table 7.2. Sample B has the smallest value, but T_c only varies within a small range of 0.5 K. This indicates that the sintering time does not significantly affect T_c.

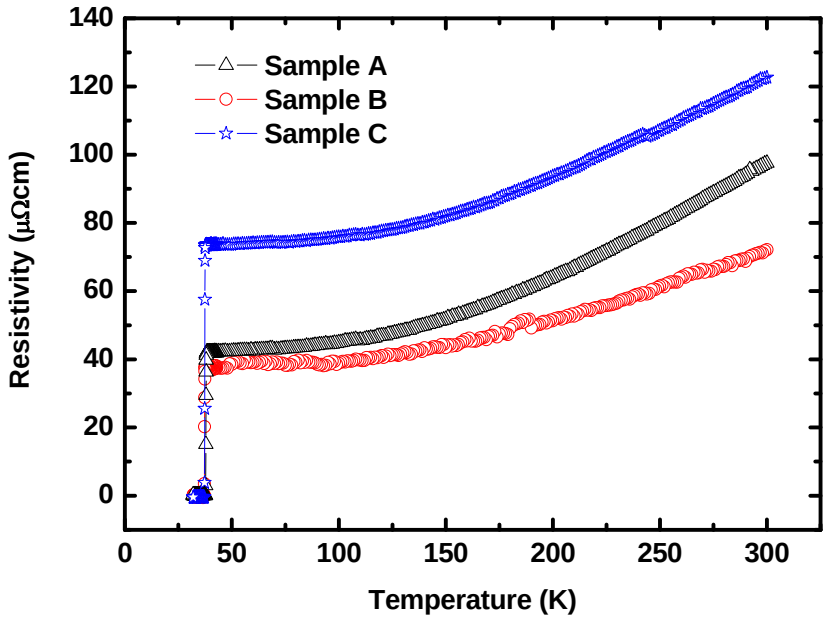

Figure 7.8 Resistivity versus temperature.

Figure 7.8 shows the resistivity-temperature curves for the three samples. The resistivity (ρ) for sample C is larger than for the other two samples. The values of ρ_{40K} and ρ_{300K} were collected from Figure 7.8 and are listed in Table 7.2. Sample B exhibits the smallest ρ_{40K} and ρ_{300K}, whereas sample A has larger values. The calculated A_F is displayed in Table 7.2. It can be seen that all the samples have low A_Fs, indicating poor connection in the samples. Sample B has a larger A_F than sample A. This may be due to the improved crystallinity and the disappearance of MgB_4 with increased sintering time. However, A_F in sample C is smaller than in sample B. The reason can be attributed to the larger amount of MgO in sample C, which obstructs the flow of the current and increases the resistivity.

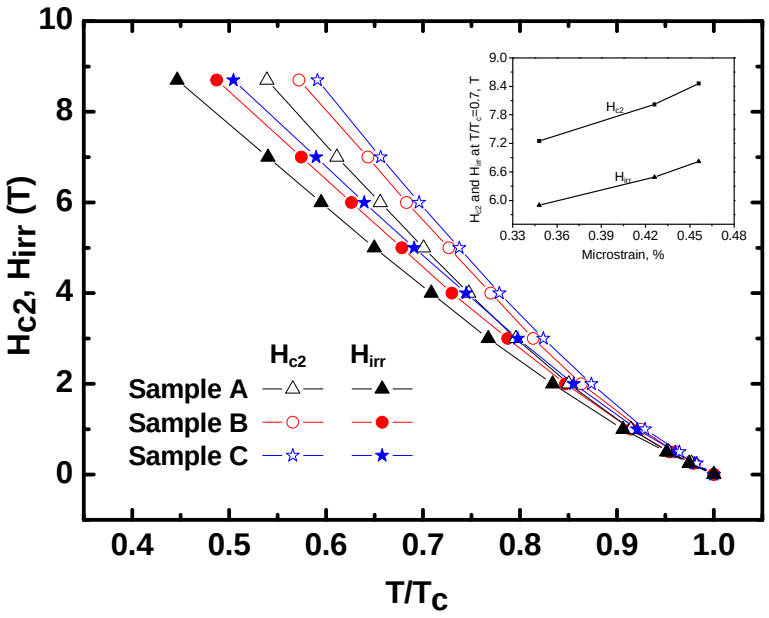

Figure 7.9 Temperature dependence of H_{c2} and H_{irr}. The inset shows the dependence of H_{c2} and H_{irr} on the microstrain.

From the resistivity curves under different magnetic fields, H_{irr} and H_{c2} can be derived, using the criteria of 10% and 90% of the normal state resistivity. The results are shown

in Figure 7.9. It can be seen that H_{c2} has concave temperature-dependence curves. As the temperature increases, H_{c2} and H_{irr} decrease. It is evident that H_{c2} and H_{irr} in the limited field regime measured increase with the sintering time. H_{c2} and H_{irr} values at $T/T_c = 0.7$ for the three samples are collected from Figure 7.9 and plotted against microstrain in the inset of Figure 7.9. It is clear that both H_{c2} and H_{irr} linearly increase with microstrain. A low microstrain indicates less lattice distortion inside the MgB_2 grains and thus a larger mean free path (l) of the superconducting electrons. This will increase the coherence length (ξ) due to the relation: $1/\xi = 1/\xi_0+1/l$, where ξ_0 is the value of ξ for the pure superconductor. According to $H_{c2} = \Phi_0/(2\pi\mu_0\xi^2)$, where Φ_0 is the superconducting flux quantum and μ_0 is the magnetic permeability, H_{c2} will decrease as ξ increases.

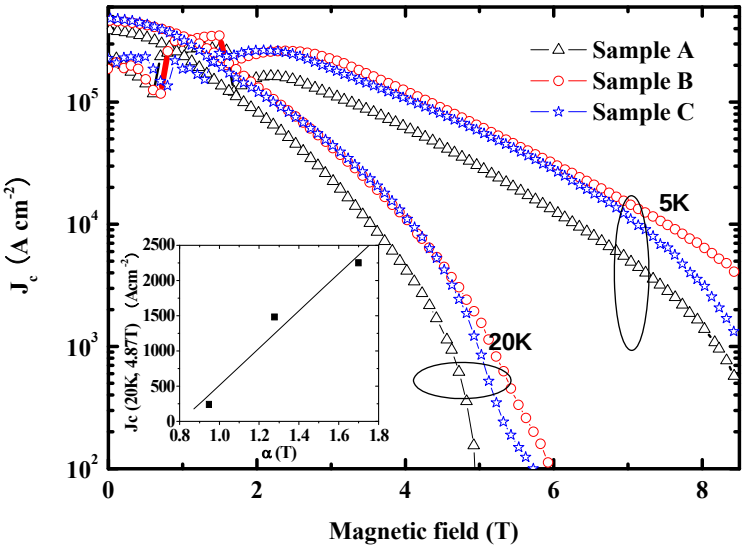

Figure 7.10 $J_c(H)$ curves at 5 K and 20 K for MgB_2 samples. The inset shows J_c at 20 K and 4.87 T as a function of $A_F \cdot H_{c2}$ for the three samples.

Figure 7.10 shows the $J_c(H)$ curves for the three samples at 5 K and 20 K. It can be seen that the J_c performance in sample B shows a significant improvement under high fields at both 5 K and 20 K. Sample B exhibits the highest J_c of ~ 6722 Acm^{-2} at 5 K and 8 T, which is more than five times higher than that of sample A and almost 2 times higher than that of sample C. The J_c values at 20 K and 4.87 T follow the same trend, namely 360 Acm^{-2}, 2450 Acm^{-2}, and 1840 Acm^{-2} for samples A, B, and C, respectively. It is well known that grain boundary pinning is the major pinning mechanism at high fields in MgB_2. The J_c caused by the grain boundary surface pinning can be calculated from $\frac{\mu_0 S_v (H_{c2} - H)^2}{4\kappa^2 H_{c2}^{1/2} H^{1/2}}$ [18], where S_v is the grain boundary surface area per unit volume, κ the Ginzburg-Landau parameter, and H the applied field. It can be concluded from this equation that J_c at high fields near H_{c2} is predominantly determined by H_{c2} and S_v [192]. In addition, the connectivity (A_F) also affects J_c. Figure 7.11 shows FEG-SEM images of samples A, B, and C. It can be seen that the grain size shows no significant change between samples. Therefore, the J_c difference is not caused by any change in S_v. the H_{c2} values at 20 K could not be obtained, so H_{c2} at 22.5 K is roughly used to replace H_{c2} at 20 K. A combined parameter $\alpha = A_F H_{c2}$ (22.5 K) is calculated and the J_c values at 20 K and 4.87 T for the three samples are plotted against α in the inset of Figure 7.9. This figure is evidence for a very good linear relationship between α and J_c. It clearly indicates that the improved J_c is mainly caused by the improved connectivity and the increased H_{c2}.

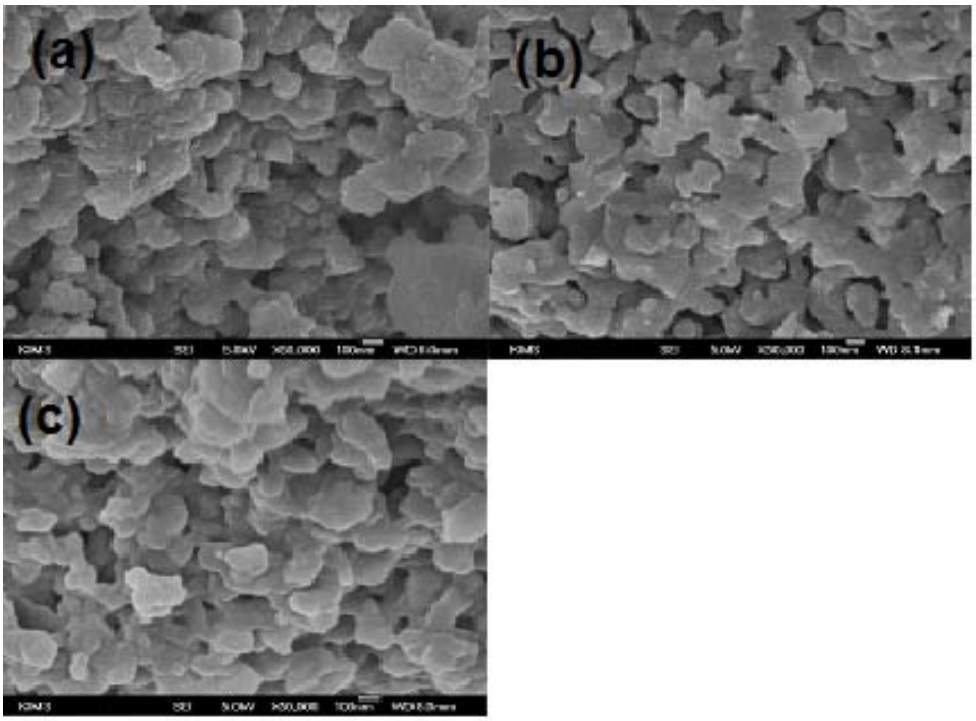

Figure 7.11 FEG-SEM images for (a) sample A, (b) sample B, and (c) sample C.

7.3 Summary

In this chapter, it has been found that the $J_c(H)$ for a sample processed under welding grade argon show a stronger pinning in high fields than samples sintered in ultra-high and high purity argon. This is consistent with the increase in resistivity, FWHM, and H_{irr} and H_{c2}, and the decrease in T_c in the WA sample. TEM examination revealed that the sample processed in welding grade argon possessed fine MgB_2 grains, a high density of defects, and large crystalline strains, which act as effective pinning centres, to which the improvement in high field J_c of this sample can be attributed. These results verify the dual reaction model that the MgB_2 formation and the reaction between oxygen and precursor need to take place simultaneously in order to result in an optimal doping effect. Fe tubing as a protective sheath material is sufficient to protect the precursor materials and resultant MgB_2 from oxidation in large-scale production.

The effect of the sintering time on the superconductivity of MgB_2 has been investigated. The sintering times were set at 10 minutes, 30 minutes, and 3 hours for the three samples. It was found that the amount of MgO increases with the sintering time and that the sample with 30 minutes sintering time has the smallest lattice parameters. H_{c2} and H_{irr} increase with the sintering time and have a linear relationship with the microstrain. The sample sintered for 30 min exhibits the highest J_c at high fields. The reason can be attributed to the improved connectivity and the increased H_{c2}.

8 Conclusions

In order to increase J_c of bulk polycrystalline MgB_2, this thesis has systematically investigated the influence of the boron precursor powder, the nominal Mg/B mixing ratio, and how to further enhance J_c by doping with two types of sources: a carbon source (such as SiC or sucrose) and an oxygen source (such as from TiO_2/SiO_2 and different levels of oxygen in the processing atmosphere). The major conclusions include:

(1) On the influence of boron precursor on the superconducting properties of MgB_2, J_c values for the MgB_2 made from ball-milled, high purity boron powders with crystalline phase are at least two times higher than for an MgB_2 sample made from ball-milled amorphous boron powder, and a factor of 40 higher than typical values for standard MgB_2 samples. The possible mechanism proposed to account for this difference is the H_{c2} enhancement caused by the increased disorder.

(2) The influence of Mg content was investigated in a series of undoped and SiC-doped MgB_2 samples with systematic variation of the nominal Mg/B ratio (x:2). It has been found that in the undoped MgB_2 samples, J_c increases with x to its maximum value at x = 1.1 and then decreases. The higher J_c at x = 1.1 is attributed to the better connectivity caused by smaller amounts of impurities. In the SiC-doped samples, it has been found that the sample with x = 1.15 exhibits the best J_c performance for all the fields (0 – 8.5 T), including the self-field, and

its T_c is higher than for the sample with x = 1. The enhancement of J_c is attributed to the improved connectivity and the increased disorder. The optimized Mg/B ratio (1.15:2) also reduces the interband scattering caused by the Mg or B vacancies and, in turn, increases T_c.

(3) Doping with sucrose at varying levels and annealing temperatures results in an optimal J_c value in $MgB_{2-x}C_x$ at x = 0.2 and 850 ^oC. At 5 K and 6 T, the x = 0.2 sample shows one order of magnitude improvement. It has been found that sucrose doping causes a small depression in T_c and high resistivity, while H_{c2} performance is improved. The reason for the enhancement of H_{c2} is likely to be increased disorder caused by C substitution for B and/or diffusion of C atoms in the MgB_2 lattice as interstitial atoms.

(4) TiO_2/SiO_2 addition leads to improved J_c values. J_c exhibits the highest value at the doping ratio of 10 wt% at 5 K and 20 K, and at the doping ratio of 5 wt% at 30 K, when the sintering temperature is fixed at 750 ^oC. When the doping ratio is fixed at 5 wt%, the sample with the sintering temperature of 750 ^oC has the best J_c for 5 K and 20 K, while the sample with the sintering temperature of 850 ^oC exhibits the highest J_c at 30 K. In addition, it has been found that the added TiO_2/SiO_2 nanoparticles result in small depressions in T_c, while H_{c2} and H_{irr} performances are improved. The enhancement of H_{c2} and H_{irr} can be attributed to the existence of precipitates induced by the TiO_2/SiO_2 doping.

(5) Additions of O_2 from different processing atmospheres produce the optimal J_c and flux pinning properties in MgB_2 when readily available and economical

welding grade Ar is used as the protective atmosphere instead of ultra-high or high purity Ar. The effect of the sintering time on the superconductivity of MgB_2 in welding grade Ar atmosphere has been investigated. The sample sintered for 30 min exhibits the highest J_c at high fields. The reason can be attributed to the improved connectivity and the increased H_{c2}.

References

1. Onnes, H.K., Communications Leiden, 1911. **120b**: p. 3.
2. Bednorz, J.G. and K.A. Müller, *Possible high Tc superconductivity in the Ba-La-Cu-O system.* Zeitschrift für Physik B Condensed Matter, 1986. **64**(2): p. 189-193.
3. Wu, M.K., et al., *Superconductivity at 93 K in a new mixed-phase Yb-Ba-Cu-O compound system at ambient pressure.* Physical Review Letters, 1987. **58**(9): p. 908-910.
4. Sheng, Z.Z. and A.M. Hermann, *Superconductivity in the rare-earth-free Tl-Ba-Cu-O system above liquid-nitrogen temperature.* Nature, 1988. **332**(6159): p. 55-58.
5. Maeda, H., et al., Japanese Journal of Applied Physics, Part 2: Letters, 1988. **27**: p. L209.
6. Schilling, A., et al., *Superconductivity above 130 K in the Hg-Ba-Ca-Cu-O system.* Nature, 1993. **363**(6424): p. 56-58.
7. Nagamatsu, J., et al., *Superconductivity at 39 K in magnesium diboride.* Nature, 2001. **410**(6824): p. 63-64.
8. W.Meissner and R. Ochsenfeld, Naturwissenschaften, 1933. **21**: p. 787.
9. Fishlock, D., *A Guide to Superconductivity*. 1969, London: MacDonald & Co. Ltd.
10. London, F. and H. London, *Supraleitung und diamagnetismus.* Physica, 1935. **2**(1-12): p. 341-354.
11. Ginzburg, V.L. and L.D. Landau, Zh. Eksp. Teor. Fiz., 1950. **20**: p. 1064.

12. Bardeen, J., L.N. Cooper, and J.R. Schrieffer, *Theory of superconductivity.* Physical Review, 1957. **108**(5): p. 1175-1204.

13. Frohlich, H., *Theory of the superconducting state. I. The ground state at the absolute zero of temperature.* Physical Review, 1950. **79**(5): p. 845-856.

14. Abrikosov, A.A., Sov. Phys. JETP, 1957. **5**: p. 1174.

15. Rose-Innes, A.C. and E.H. Rhoderick, *Introduction to Superconductivity*. 1994: 2nd (Revised) ed (Oxford, U.K.: Pergamon Press).

16. Kim, Y.B., C.F. Hempstead, and A.R. Strnad, *Critical persistent currents in hard superconductors.* Physical Review Letters, 1962. **9**(7): p. 306-309.

17. Campbell, A.M. and J.E. Evetts, *Flux vortices and transport currents in type II superconductors.* Advances in Physics, 1972. **21**(90 March): p. 199-428.

18. Dew-Hughes, D., *Flux pinning mechanisms in type II superconductors.* Philosophical Magazine, 1974. **30**: p. 293-305.

19. Yamamoto, A., et al., *Crystallinity and flux pinning properties of MgB_2 bulks.* Physica C: Superconductivity and its Applications, 2006. **445-448**(1-2): p. 806-810.

20. Keshavarzi, S., et al., *Vortex dynamics in pure and SiC-doped MgB_2.* Physica C: Superconductivity and its Applications, 2004. **408-410**(1-4): p. 601-602.

21. http://www.istec.or.jp/Isis/E2summit.html.

22. Seeber, B., *commercially available superconducting wires.* Handbook of applied superconductivity, Bristol, U.K.: Inst. of Physics, 1998: p. 397.

23. Vinod, K., R.G. Abhilash Kumar, and U. Syamaprasad, *Prospects for MgB_2 superconductors for magnet application.* Superconductor Science and Technology, 2007. **20**(1): p. R1-R13.

24. Larbalestier, D., et al., *High-Tc superconducting materials for electric power applications.* Nature, 2001. **414**(6861): p. 368-377.

25. Zheng, D.N., N.J.C. Ingle, and A.M. Campbell, *Irreversibility fields of superconducting niobium alloys.* Physical Review B, 2000. **61**(22): p. 15429.

26. Li, C. and D.C. Larbalestier, *Development of high critical current densities in niobium 46.5 wt% titanium.* Cryogenics, 1987. **27**(4): p. 171-177.

27. Lee, P.J., et al., *Development of high performance Nb-Ti(Fe) multifilamentary superconductor for the LHC insertion quadrupoles.* Applied Superconductivity, IEEE Transactions on, 1999. **9**(2): p. 1559-1562.

28. Lee, P.J., et al., *Development of high performance multifilamentary Nb-Ti-Ta superconductor for LHC insertion quadrupoles.* Applied Superconductivity, IEEE Transactions on, 1999. **9**(2): p. 1571-1574.

29. Godeke, A., *A review of the properties of Nb_3Sn and their variation with A15 composition, morphology and strain state.* Superconductor Science and Technology, 2006. **19**(8): p. R68-R80.

30. Godeke, A., et al., *The upper critical field of filamentary Nb_3Sn conductors.* Journal of Applied Physics, 2005. **97**(9): p. 1-12.

31. Suenaga, M., et al., *Superconducting critical temperatures, critical magnetic fields, lattice parameters, and chemical compositions of "bulk" pure and alloyed Nb_3Sn produced by the bronze process.* Journal of Applied Physics, 1986. **59**(3): p. 840-853.

32. Cooley, L.D., Y.F. Hu, and A.R. Moodenbaugh, *Enhancement of the upper critical field of Nb_3Sn utilizing disorder introduced by ball milling the elements.* Applied Physics Letters, 2006. **88**(14): p. 142506.

33. Parrell, J.A., et al., *Advances in Nb_3Sn strand for fusion and particle accelerator applications.* IEEE Transactions on Applied Superconductivity, 2005. **15**(2 PART II): p. 1200-1204.

34. Vostner, A. and E. Salpietro, *Enhanced critical current densities in Nb_3Sn superconductors for large magnets.* Superconductor Science and Technology, 2006. **19**(3): p. S90-S95.

35. Seeber, B., *Power applications of superconductivity*, in *Handbook of applied superconductivity*. 1998, Bristol, U.K. : Inst. of Phys.,. p. 1485-1756.

36. Jones, M.E. and R.E. Marsh, *The preparation and structure of magnesium boride, MgB_2.* Journal of the American Chemical Society, 1954. **76**(5): p. 1434-1436.

37. Buzea, C. and T. Yamashita, *Review of the superconducting properties of MgB_2.* Superconductor Science and Technology, 2001. **14**(11): p. R115 - R146.

38. Bordet, P., et al., *Absence of a structural transition up to 40 GPa in MgB_2 and the relevance of magnesium nonstoichiometry.* Physical Review B - Condensed Matter and Materials Physics, 2001. **64**(17): p. 1725021-1725024.

39. Tinkham, M., *Introduction to Superconductivity.* 1975(New York: McGraw-Hill).

40. Kortus, J., et al., *Superconductivity of metallic Boron in MgB_2.* Physical Review Letters, 2001. **86**(20): p. 4656-4659.

41. Canfield, P.C. and G.W. Crabtree, *Magnesium diboride: Better late than never.* Physics Today, 2003. **56**(3): p. 34-40.

42. Choi, H.J., et al., *The origin of the anomalous superconducting properties of MgB_2.* Nature, 2002. **418**(6899): p. 758-760.

43. Iavarone, M., et al., *Two-band superconductivity in MgB_2.* Physical Review Letters, 2002. **89**(18): p. 187002.

44. Fujii, H., H. Kumakura, and K. Togano, *Influence of MgB_2 powder quality on the transport properties of Cu-sheathed MgB_2 tapes.* Physica C: Superconductivity and its Applications, 2001. **363**(4): p. 237-242.

45. Birkedal, H., et al., *Thermal expansion and phase purity of commercial MgB_2.* Journal of Materials Science Letters, 2003. **22**(15): p. 1069-1071.

46. Kovac, P., et al., *The role of MgO content in ex situ MgB_2 wires.* Superconductor Science and Technology, 2004. **17**(10): p. L41.

47. Yamada, H., et al., *Critical current densities of powder-in-tube MgB_2 tapes fabricated with nanometer-size Mg powder.* Applied Physics Letters, 2004. **84**(10): p. 1728-1730.

48. Hinks, D.G., et al., *Synthesis and stoichiometry of MgB_2.* Physica C: Superconductivity and its Applications, 2002. **382**(2-3): p. 166-176.

49. Ribeiro, R.A., et al., *Effects of boron purity, Mg stoichiometry and carbon substitution on properties of polycrystalline MgB_2.* Physica C: Superconductivity, 2003. **385**(1-2): p. 16-23.

50. Chen, S.K., et al., *Strong influence of boron precursor powder on the critical current density of MgB_2.* Superconductor Science and Technology, 2005. **18**(11): p. 1473-1477.

51. Prikhna, T.A., et al., *High-pressure synthesis of a bulk superconductive MgB_2-based material.* Physica C: Superconductivity and its Applications, 2003. **386**: p. 565-568.

52. Pan, A.V., et al., *Properties of superconducting MgB_2 wires: In situ versus ex situ reaction technique.* Superconductor Science and Technology, 2003. **16**(5): p. 639-644.

53. Schlachter, S.I., et al., *Influence of the preparation process on microstructure, critical current density and Tc of MgB_2 powder-in-tube wires.* IEEE Transactions on Applied Superconductivity, 2003. **13**(2 III): p. 3203-3206.

54. Flukiger, R., et al., *Improved transport critical current and irreversibility fields in mono- and multifilamentary Fe/MgB_2 tapes and wires using fine powders.* Superconductor Science and Technology, 2003. **16**(2): p. 264-270.

55. Zhou, S., et al., *Effects of precursor powders and sintering processes on the superconducting properties of MgB_2.* Superconductor Science and Technology, 2004. **17**(9): p. S583.

56. Margadonna, S., et al., *Phase inhomogeneities and lattice expansion near T_c in the $Mg_{11}B_2$ superconductor.* Journal of Physics Condensed Matter, 2001. **13**(35): p. L795-L802.

57. Xue, Y.Y., et al., *Nonstoichiometry, defects and transport properties in MgB_2.* Physica C: Superconductivity and its Applications, 2002. **377**(1-2): p. 7-14.

58. Sharma, P.A., et al., *Percolative superconductivity in $Mg_{1-x}B_2$.* Physical Review Letters, 2002. **89**(16): p. 167003.

59. Urbano, R.R., et al., *Electronic phase-separation in $Mg_{1-x}B_2$ probed by CESR.* Physica C: Superconductivity and its Applications, 2004. **408-410**(1-4): p. 832-833.

60. Serquis, A., et al., *Effect of lattice strain and defects on the superconductivity of MgB_2.* Applied Physics Letters, 2001. **79**(26): p. 4399-4401.

61. Mori, H., et al., *Electron density distribution in a single crystal of $Mg_{1-x}B_2$ [x=0.045(5)]*. Physical Review B - Condensed Matter and Materials Physics, 2002. **65**(9): p. 925071-925074.

62. Lee, S., *Crystal growth of MgB_2.* Physica C: Superconductivity and its Applications, 2003. **385**(1-2): p. 31-41.

63. Yamamoto, A., et al., *Improved critical current properties observed in MgB_2 bulks synthesized by low-temperature solid-state reaction.* Superconductor Science and Technology, 2005. **18**(1): p. 116-121.

64. Yamamoto, A., et al., *Effects of sintering conditions on critical current properties and microstructures of MgB_2 bulks.* Physica C: Superconductivity and its Applications, 2005. **426-431**(II): p. 1220-1224.

65. Kim, J.H., et al., *The effects of sintering temperature on superconductivity in MgB_2/Fe wires.* Superconductor Science & Technology, 2007. **20**(5): p. 448-451.

66. Canfield, P.C., et al., *Superconductivity in dense MgB_2 wires.* Physical Review Letters, 2001. **86**(11): p. 2423-2426.

67. Glowacki, B.A., et al., *Superconductivity of powder-in-tube MgB_2 wires.* Superconductor Science and Technology, 2001. **14**(4): p. 193-199.

68. Goldacker, W., et al., *High transport currents in mechanically reinforced MgB_2 wires.* Superconductor Science and Technology, 2001. **14**(9): p. 787-793.

69. Glowacki, B.A. and M. Majoros, *MgB_2 conductors for dc and ac applications.* Physica C: Superconductivity and its Applications, 2002. **372-376**(PART 2): p. 1235-1240.

70. Flukiger, R., et al., *Superconducting properties of MgB_2 tapes and wires.* Physica C: Superconductivity and its Applications, 2003. **385**(1-2): p. 286-305.

71. Zhou, S.H., et al., *Effect of various mechanical deformation processes on critical current density and microstructure in MgB_2 tapes and wires.* Superconductor Science & Technology, 2002. **15**(11): p. 1490-1493.

72. Zhou, S., et al., *Single- and multi-filamentary Fe-sheathed MgB_2 wires.* Physica C: Superconductivity and its Applications, 2002. **382**(4): p. 349-354.

73. Zhou, S., et al., *Effect of Ti doping on the superconductivities of MgB_2/Fe wires.* Journal of Low Temperature Physics, 2003. **131**(3-4): p. 687-692.

74. Zhou, S.H., et al., *Effect of the processing parameters of $MgB_{1.8}(SiC)_{0.1}$/Fe tapes on the critical current density.* Physica C: Superconductivity and its Applications, 2003. **387**(3-4): p. 321-327.

75. Collings, E.W., et al., *Continuous- and batch-processed MgB_2/Fe strands - Transport and magnetic properties.* Physica C: Superconductivity and its Applications, 2003. **386**: p. 555-559.

76. Dou, S.X., et al., *Transport critical current density in Fe-sheathed nano-SiC doped MgB_2 wires.* IEEE Transactions on Applied Superconductivity, 2003. **13**(2 III): p. 3199-3202.

77. Fabbricatore, P., et al., *Influence of the sintering process on critical currents, irreversibility lines and pinning energies in multifilamentary MgB_2 wires.* Superconductor Science and Technology, 2003. **16**(3): p. 364-370.

78. Feng, Y., et al., *Superconducting properties of MgB_2 wires and tapes with different metal sheaths.* Physica C: Superconductivity and its Applications, 2003. **386**: p. 598-602.

79. Feng, Y., et al., *High critical current density in MgB_2/Fe wires.* Superconductor Science and Technology, 2003. **16**(6): p. 682-684.

80. Flukiger, R., et al., *Erratum: Superconducting properties of MgB_2 tapes and wires (Physica C (2003) 385 (286-305) PII: S0921453402023079).* Physica C: Superconductivity and its Applications, 2003. **387**(3-4): p. 419.

81. Glowacki, B.A., et al., *MgB_2 superconductors for applications.* Physica C: Superconductivity and its Applications, 2003. **387**(1-2): p. 153-161.

82. Goldacker, W., et al., *Mechanical properties of reinforced MgB_2 wires.* IEEE Transactions on Applied Superconductivity, 2003. **13**(2 III): p. 3261-3264.

83. Horvat, J., et al., *Magnetic shielding in MgB_2/Fe superconducting wires.* IEEE Transactions on Applied Superconductivity, 2003. **13**(2 III): p. 3324-3327.

84. Suo, H., et al., *Large transport critical currents in dense Fe- and Ni-clad MgB_2 superconducting tapes.* Applied Physics Letters, 2001. **79**(19): p. 3116-3118.

85. Kumakura, H., et al., *Fabrication and properties of powder-in-tube processed MgB_2 tapes and wires.* Journal of Low Temperature Physics, 2003. **131**(5-6): p. 1085-1094.

86. Glowacki, B.A., et al., *Superconducting properties of the powder-in-tube Cu-Mg-B and Ag-Mg-B wires.* Physica C: Superconductivity and its Applications, 2002. **372-376**(PART 2): p. 1254-1257.

87. Eisterer, M., et al., *Enhanced transport currents in Cu-sheathed MgB_2 wires.* Superconductor Science and Technology, 2002. **15**(7): p. 1088-1091.

88. Pradhan, A.K., et al., *Transport behavior and critical current densities in MgB_2 wires.* Applied Physics Letters, 2001. **79**(11): p. 1649-1651.

89. Beilin, V., et al., *Critical current anisotropy in non-sintered metal-clad MgB_2 tapes.* Physica C: Superconductivity and its Applications, 2002. **377**(1-2): p. 15-20.

90. Majoros, M., B.A. Glowacki, and M.E. Vickers, *50 K anomalies in superconducting MgB_2 wires in copper and silver tubes.* Superconductor Science and Technology, 2002. **15**(2): p. 269-275.

91. Pachla, W., et al., *Structural inhomogeneity of superconducting ex situ MgB_2/Cu wires made by the powder-in-tube technique.* Superconductor Science and Technology, 2002. **15**(9): p. 1281-1287.

92. Soltanian, S., et al., *Transport critical current of solenoidal MgB_2/Cu coils fabricated using a wind-reaction in situ technique.* Superconductor Science & Technology, 2003. **16**(1): p. L4-L6.

93. Soltanian, S., et al., *Improvement of critical current density in the Cu/MgB_2 and Ag/MgB_2 superconducting wires using the fast formation method.* Physica C: Superconductivity and its Applications, 2002. **382**(2-3): p. 187-193.

94. Strickland, N.M., R.G. Buckley, and A. Otto, *High critical current densities in Cu-sheathed MgB_2 formed from a mechanically-alloyed precursor.* Applied Physics Letters, 2003. **83**(2): p. 326-328.

95. Grasso, G., et al., *Large transport critical currents in unsintered MgB_2 superconducting tapes.* Applied Physics Letters, 2001. **79**(2): p. 230-232.

96. Grasso, G., et al., *Transport properties of powder-in-tube processed MgB_2 tapes.* Physica C: Superconductivity and its Applications, 2002. **378-381**(PART 2): p. 899-902.

97. Malagoli, A., et al., *Magnetic field dependence of the critical current in MgB_2 and Bi-2223 superconducting tapes fabricated by the powder-in-tube method.* IEEE Transactions on Applied Superconductivity, 2003. **13**(2 III): p. 3328-3331.

98. Tanaka, K., et al., *Fabrication and transport properties of MgB_2 wire and coil.* Physica C: Superconductivity and its Applications, 2002. **382**(2-3): p. 203-206.

99. Giunchi, G., et al., *High performance new MgB_2 superconducting hollow wires.* Superconductor Science and Technology, 2003. **16**(2): p. 285-291.

100. Xu, J.D., et al., *Preparation of MgB_2 superconducting tapes using electrophoresis.* Superconductor Science and Technology, 2002. **15**(8): p. 1190-1192.

101. Matsumoto, A., et al., *Effect of SiO_2 and SiC doping on the powder-in-tube processed MgB_2 tapes.* Superconductor Science and Technology, 2003. **16**(8): p. 926-930.

102. Serquis, A., et al., *Microstructure and high critical current of powder-in-tube MgB_2.* Applied Physics Letters, 2003. **82**(11): p. 1754-1756.

103. Kitaguchi, H., H. Kumakura, and K. Togano, *Strain effect in MgB_2/stainless steel superconducting tape.* Physica C: Superconductivity and its Applications, 2001. **363**(3): p. 198-201.

104. Kumakura, H., et al., *High transport critical current density obtained for powder-in-tube-processed MgB_2 tapes and wires using stainless steel and Cu-Ni tubes.* Applied Physics Letters, 2001. **79**(15): p. 2435-2437.

105. Feng, Y., et al., *High critical current density in powder-in-tube processed MgB_2/Ta/Cu wire.* Chinese Science Bulletin, 2002. **47**(3): p. 251-252.

106. Feng, Y., et al., *Fabrication and superconducting properties of MgB_2 composite wires by the PIT method.* Superconductor Science and Technology, 2002. **15**(1): p. 12-15.

107. Grovenor, C.R.M., et al., *Interfacial reactions and oxygen distribution in MgB_2 wires in Fe, stainless steel and Nb sheaths.* Superconductor Science and Technology, 2004. **17**(3): p. 479-484.

108. Mannhart, J., et al., *Critical currents in [001] grains and across their tilt boundaries in $YBa_2Cu_3O_7$ Films.* Physical Review Letters, 1988. **61**(21): p. 2476-2479.

109. Ekin, J.W., et al., *Evidence for weak link and anisotropy limitations on the transport critical current in bulk polycrystalline $Y_1Ba_2Cu_3O$ x.* Journal of Applied Physics, 1987. **62**(12): p. 4821-4828.

110. Larbalestier, D.C., et al., *Strongly linked current flow in polycrystalline forms of the superconductor MgB_2.* Nature, 2001. **410**(6825): p. 186-189.

111. Kambara, M., et al., *High intergranular critical currents in metallic MgB_2 superconductor.* Superconductor Science and Technology, 2001. **14**(4): p. L5-L7.

112. Rowell, J.M., *The widely variable resistivity of MgB_2 samples.* Superconductor Science and Technology, 2003. **16**(6): p. R17-R27.

113. Klie, R.F., et al., *Direct observation of nanometer-scale Mg- and B-oxide phases at grain boundaries in MgB_2.* Applied Physics Letters, 2001. **79**(12): p. 1837-1839.

114. Zhu, Y., et al., *Microstructure and structural defects in MgB_2 superconductor.* Physica C: Superconductivity and its Applications, 2001. **356**(4): p. 239-253.

115. Dou, S.X., et al., *Enhancement of the critical current density and flux pinning of MgB_2 superconductor by nanoparticle SiC doping.* Applied Physics Letters, 2002. **81**(18): p. 3419-3421.

116. Serquis, A., et al., *Influence of microstructures and crystalline defects on the superconductivity of MgB_2.* Journal of Applied Physics, 2002. **92**(1): p. 351.

117. Handstein, A., et al., *Fully dense MgB_2 superconductor textured by hot deformation.* Journal of Alloys and Compounds, 2001. **329**(1-2): p. 285-289.

118. Gümbel, A., et al., *Improved superconducting properties in nanocrystalline bulk MgB_2.* Applied Physics Letters, 2002. **80**(15): p. 2725-2727.

119. Pradhan, A.K., et al., *Electrical transport and anisotropic superconducting properties in single crystalline and dense polycrystalline MgB_2.* Physical Review B - Condensed Matter and Materials Physics, 2001. **64**(21): p. 2125091-2125094.

120. Takano, Y., et al., *Superconducting properties of MgB_2 bulk materials prepared by high-pressure sintering.* Applied Physics Letters, 2001. **78**(19): p. 2914-2916.

121. Muranaka, T., et al., *Superconductivity in MgB_2, in Frontiers in Superconductifng Materials*, ed. A.V. Narlikar. 2005: Springer Berlin heidelberg: New York. p. 937-981.

122. Berenov, A., et al., *Enhancement of critical current density in low level Al-doped MgB_2.* Superconductor Science and Technology, 2004. **17**(10): p. 1093-1096.

123. Zhao, Y., et al., *High critical current density of MgB_2 bulk superconductor doped with Ti and sintered at ambient pressure.* Applied Physics Letters, 2001. **79**(8): p. 1154-1156.

124. Feng, Y., et al., *Enhanced flux pinning in Zr-doped MgB_2 bulk superconductors prepared at ambient pressure.* Journal of Applied Physics, 2002. **92**(5): p. 2614-2619.

125. Zhao, Y., et al., *Doping effect of Zr and Ti on the critical current density of MgB_2 bulk superconductors prepared under ambient pressure.* Physica C: Superconductivity and its Applications, 2002. **378-381**(PART 1): p. 122-126.

126. Yamamoto, A., et al., *Effects of B_4C doping on critical current properties of MgB_2 superconductor.* Superconductor Science and Technology, 2005. **18**(10): p. 1323-1328.

127. Yamamoto, A., et al., *Universal relationship between crystallinity and irreversibility field of MgB_2.* Applied Physics Letters, 2005. **86**(21): p. 212502.

128. Lezza, P., C. Senatore, and R. Flu?kiger, *Improved critical current densities in B4C doped MgB_2 based wires.* Superconductor Science and Technology, 2006. **19**(10): p. 1030-1033.

129. Dou, S.X., et al., *Mechanism of enhancement in electromagnetic properties of MgB_2 by nano SiC doping.* Physical Review Letters, 2007. **98**(9): p. 097002.

130. Shen, T.M., et al., *Doping effects of carbon and titanium on the critical current density of MgB_2.* Superconductor Science and Technology, 2006. **19**(11): p. 1219-1224.

131. Zhao, Y., et al., *Cooperative doping effects of Ti and C on critical current density and irreversibility field of MgB_2.* Journal of Applied Physics, 2006. **100**(12): p. 123902.

132. Ma, Y., et al., *Large irreversibility field in nanoscale C-doped MgB_2/Fe tape conductors.* Superconductor Science and Technology, 2007. **20**(3): p. L5.

133. Yeoh, W.K., et al., *Control of nano carbon substitution for enhancing the critical current density in MgB_2.* Superconductor Science & Technology, 2006. **19**(6): p. 596-599.

134. Ma, Y., et al., *Significantly enhanced critical current densities in MgB_2 tapes made by a scaleable nanocarbon addition route.* Applied Physics Letters, 2006. **88**(7): p. 072502.

135. Yan, S.C., et al., *Enhancement of the upper critical field in sub-micron carbon-doped MgB_2 by two-step reaction method.* Superconductor Science and Technology, 2007. **20**(4): p. 377-380.

136. Chen, S.K., et al., *Effect of heating rates on superconducting properties of pure MgB_2, carbon nanotube- and nano-SiC-doped in situ MgB_2 Fe wires.* Applied Physics Letters, 2005. **87**(18): p. 182504.

137. Kim, J.H., et al., *Superconductivity of MgB_2 with embedded multiwall carbon nanotube.* Physica C: Superconductivity and its Applications, 2006. **449**(2): p. 133-138.

138. Kim, J.H., et al., *The doping effect of multiwall carbon nanotube on MgB_2/Fe superconductor wire.* Journal of Applied Physics, 2006. **100**(1): p. 013908.

139. Dou, S.X., et al., *Magnetic field processing to enhance critical current densities of MgB_2 superconductors.* Applied Physics Letters, 2006. **89**(20): p. 097002.

140. Yeoh, W.K., et al., *Strong pinning and high critical current density in carbon nanotube doped MgB_2.* Superconductor Science & Technology, 2004. **17**(9): p. S572-S577.

141. Serquis, A., et al., *Correlated enhancement of H_{c2} and Jc in carbon nanotube doped MgB_2.* Superconductor Science and Technology, 2007. **20**(4): p. L12-L15.

142. Yeoh, W.K., et al., *Improving flux pinning of MgB_2 by carbon nanotube doping and ultrasonication.* Superconductor Science & Technology, 2006. **19**(2): p. L5-L8.

143. Dou, S.X., et al., *Effect of carbon nanotube doping on critical current density of MgB_2 superconductor.* Applied Physics Letters, 2003. **83**(24): p. 4996-4998.

144. Kim, J.H., et al., *Enhancement of in-field Jc in MgB_2/Fe wire using single- And multiwalled carbon nanotubes.* Applied Physics Letters, 2006. **89**(12): p. 122510.

145. Cheng, C.H., et al., *Comparison between nano-diamond and carbon nanotube doping effects on critical current density and flux pinning in MgB_2.* Superconductor Science and Technology, 2007. **20**(3): p. 296-301.

146. Cheng, C.H., et al., *Doping effect of nano-diamond on superconductivity and flux pinning in MgB_2.* Superconductor Science and Technology, 2003. **16**(10): p. 1182-1186.

147. Gao, Z., et al., *Effects of NbC addition on the critical current density of MgB_2 tapes.* Superconductor Science and Technology, 2007. **20**(1): p. 57-61.

148. Eisterer, M., et al., *Universal influence of disorder on MgB_2 wires.* Superconductor Science & Technology, 2007. **20**(3): p. 117-122.

149. Matsumoto, A., et al., *Effect of impurity additions on the microstructures and superconducting properties of in situ-processed MgB_2 tapes.* Superconductor Science and Technology, 2004. **17**(5): p. S319.

150. Matsumoto, A., et al., *Evaluation of connectivity, flux pinning, and upper critical field contributions to the critical current density of bulk pure and SiC-alloyed MgB_2.* Applied Physics Letters, 2006. **89**(13): p. 132508.

151. Soltanian, S., et al., *High transport critical current density and large $H\text{-}_{c2}$ and $H\text{-}_{irr}$ in nanoscale SiC doped MgB_2 wires sintered at low temperature.* Superconductor Science & Technology, 2005. **18**(5): p. 658-666.

152. Kumakura, H., et al., *Upper critical field, irreversibility field, and critical current density of powder-in-tube-processed MgB_2/Fe tapes.* Superconductor Science and Technology, 2005. **18**(8): p. 1042-1046.

153. Nakane, T., et al., *Effect of SiC nanoparticle addition on the critical current density of MgB_2 tapes fabricated from MgH_2, B and MgB_2 powder mixtures.* Superconductor Science and Technology, 2005. **18**(10): p. 1337-1341.

154. Wang, X.L., Z.X. Cheng, and S.X. Dou, *Silicon oil: A cheap liquid additive for enhancing in-field critical current density in MgB_2.* Applied Physics Letters, 2007. **90**(4): p. 042501.

155. Dou, S.X., et al., *Nanoscale-SiC doping for enhancing J_c and H_{c2} in superconducting MgB_2.* Journal of Applied Physics, 2004. **96**(12): p. 7549-7555.

156. Hata, S., et al., *Microstructures of MgB_2/Fe tapes fabricated by an in situ powder-in-tube method using MgH_2 as a precursor powder.* Superconductor Science and Technology, 2006. **19**(2): p. 161-168.

157. Jiang, C.H., H. Hatakeyama, and H. Kumakura, *Preparation of MgB_2/Fe tapes with improved Jc property using MgH_2 powder and a short pre-annealing and intermediate rolling process.* Superconductor Science and Technology, 2005. **18**(5): p. L17.

158. Dou, S.X., et al., *Substitution-induced pinning in MgB_2 superconductor doped with SiC nano-particles.* Superconductor Science & Technology, 2002. **15**(11): p. 1587-1591.

159. Eisterer, M., et al., *Neutron irradiation of sic doped and magnesium rich MgB_2 wires.* IEEE Transactions on Applied Superconductivity, 2007. **17**(2): p. 2814-2817.

160. Kovac, P., T. Melisek, and I. Husek, *Ic anisotropy of in situ made MgB_2 tapes.* Superconductor Science and Technology, 2005. **18**(7): p. L45.

161. Jiang, C.H., et al., *Enhanced Jc property in nano-SiC doped thin MgB_2/Fe wires by a modified in situ PIT process.* Physica C: Superconductivity and its Applications, 2005. **422**(3-4): p. 127-131.

162. Ma, Y., et al., *The effect of $ZrSi_2$ and SiC doping on the microstructure and Jc-B properties of PIT processed MgB_2 tapes.* Superconductor Science and Technology, 2006. **19**(1): p. 133-137.

163. Yamada, H., et al., *The excellent superconducting properties of in situ powder-in-tube processed MgB_2 tapes with both ethyltoluene and SiC powder added.* Superconductor Science and Technology, 2007. **20**(6): p. L30-L33.

164. Zhang, X., et al., *The effect of different nanoscale material doping on the critical current properties of in situ processed MgB_2 tapes.* Superconductor Science and Technology, 2006. **19**(6): p. 479-483.

165. Shcherbakova, O., et al., *The effect of doping level and sintering temperature on $J_c(H)$ performance in nano-SiC doped and pure MgB_2 wires.* Journal of Applied Physics, 2006. **99**(8): p. 08M510.

166. Sumption, M.D., et al., *Transport and magnetic Jc of MgB_2 strands and small helical coils.* Applied Physics Letters, 2005. **86**(10): p. 102501.

167. Kovac, P., et al., *Transport current improvements of in situ MgB_2 tapes by the addition of carbon nanotubes, silicon carbide or graphite.* Superconductor Science and Technology, 2007. **20**(1): p. 105-111.

168. Kumakura, H., et al., *Upper critical fields of powder-in-tube-processed MgB_2/Fe tape conductors.* Applied Physics Letters, 2004. **84**(18): p. 3669-3671.

169. Li, S., et al., *Intense vortex pinning enhanced by semicrystalline defect traps in self-aligned nanostructured MgB_2.* Applied Physics Letters, 2003. **83**(2): p. 314-316.

170. Sumption, M.D., et al., *Irreversibility field and flux pinning in MgB_2 with and without SiC additions.* Superconductor Science & Technology, 2004. **17**(10): p. 1180-1184.

171. Sumption, M.D., et al., *Large upper critical field and irreversibility field in MgB_2 wires with SiC additions.* Applied Physics Letters, 2005. **86**(9): p. 092507.

172. Wang, X.L., et al., *Significant improvement of critical current density in coated MgB_2/Cu short tapes through nano-SiC doping and short-time in situ reaction.* Superconductor Science and Technology, 2004. **17**(3): p. L21.

173. Gao, Z., et al., *Strongly enhanced critical current density in MgB_2/Fe tapes by stearic acid and stearate doping.* Superconductor Science and Technology, 2007. **20**(5): p. 485-489.

174. Hossain, M.S.A., et al., *Enhancement of flux pinning in a MgB_2 superconductor doped with tartaric acid.* Superconductor Science & Technology, 2007. **20**(1): p. 112-116.

175. Kim, J.H., et al., *Carbohydrate doping to enhance electromagnetic properties of MgB_2 superconductors.* Applied Physics Letters, 2006. **89**(14): p. 142505.

176. Xu, X., et al., *Improved J(c) of MgB_2 superconductor by ball milling using different media.* Superconductor Science & Technology, 2006. **19**(11): p. L47-L50.

177. Yamada, H., et al., *Effect of aromatic hydrocarbon addition on in situ powder-in-tube processed MgB_2 tapes.* Superconductor Science and Technology, 2006. **19**(2): p. 175-177.

178. Dou, S.X., et al., *Superconductivity, critical current density, and flux pinning in $MgB_{2-x}(SiC)_{x/2}$ superconductor after SiC nanoparticle doping.* Journal of Applied Physics, 2003. **94**(3): p. 1850-1856.

179. Kumakura, H., et al., *Improved superconducting properties of in-situ PIT-processed MgB_2 tapes.* IEEE Transactions on Applied Superconductivity, 2005. **15**(2 PART III): p. 3184-3187.

180. Zhou, S., et al., *Sugar coating of boron powder for efficient carbon doping of MgB_2 with enhanced current-carrying performance.* Advanced Materials, 2007. **19**(10): p. 1373-1376.

181. Gao, Z., et al., *Enhancement of the critical current density and the irreversibility field in maleic anhydride doped MgB_2 based tapes.* Journal of Applied Physics, 2007. **102**(1): p. 013914.

182. Gao, Z., et al., *Influence of oxygen contents of carbohydrate dopants on connectivity and critical current density in MgB_2 tapes.* Applied Physics Letters, 2007. **91**(16): p. 162504.

183. Kim, J.H., et al., *Influence of disorder on the in-field Jc of MgB_2 wires using highly active pyrene.* Applied Physics Letters, 2008. **92**(4): p. 042506.

184. Ueda, S., et al., *Flux pinning properties of impurity doped MgB_2 bulks synthesized by diffusion method.* Physica C: Superconductivity and its Applications, 2005. **426-431**(II): p. 1225-1230.

185. Yamamoto, A., et al., *Doping effects on critical current properties of MgB_2 bulks synthesized by modified powder-In-tube method.* IEEE Transactions on Applied Superconductivity, 2005. **15**(2 PART III): p. 3292-3295.

186. Soltanian, S., et al., *Effect of nano-carbon particle doping on the flux pinning properties of MgB_2 superconductor.* Physica C: Superconductivity and its Applications, 2003. **390**(3): p. 185-190.

187. Senkowicz, B.J., et al., *Improved upper critical field in bulk-form magnesium diboride by mechanical alloying with carbon.* Applied Physics Letters, 2005. **86**(20): p. 1-3.

188. Dou, S.X., et al., *Alignment of carbon nanotube additives for improved performance of magnesium diboride superconductors.* Advanced Materials, 2006. **18**(6): p. 785-788.

189. Yeoh, W.K., et al., *Effect of carbon nanotube size on superconductivity properties of MgB_2.* IEEE Transactions on Applied Superconductivity, 2005. **15**(2 PART III): p. 3284-3287.

190. Hossain, M.S.A., et al., *Significant enhancement of $H\text{-}_{c2}$ and $H\text{-}_{irr}$ in $MgB_2+C_4H_6O_5$ bulks at a low sintering temperature of 600 degrees C.* Superconductor Science & Technology, 2007. **20**(8): p. L51-L54.

191. Jiang, C.H., et al., *Light carbon doping by oxygen-free paraffin wax to enhance the current density of MgB_2 in the entire field regime.* Superconductor Science & Technology, 2008. **21**(6): p. 065017.

192. Eisterer, M., *Magnetic properties and critical currents of MgB_2.* Superconductor Science and Technology, 2007. **20**(12): p. R47-R73.

193. Soltanian, S., et al., *High-transport critical current density above 30 K in pure Fe-clad MgB_2 tape.* Physica C: Superconductivity and its Applications, 2001. **361**(2): p. 84-90.

194. Jiang, C.H., H. Hatakeyama, and H. Kumakura, *Effect of nanometer MgO addition on the in situ PIT processed MgB_2/Fe tapes.* Physica C: Superconductivity and its Applications, 2005. **423**(1-2): p. 45-50.

195. Delfany, M., et al., *Nano-sized Al_2O_3 doping effects on the critical current density of MgB_2 superconductors.* Ceramics International, 2004. **30**(7): p. 1581-1583.

196. Rui, X.F., et al., *Doping effect of nano-alumina on MgB_2.* Physica C: Superconductivity and its Applications, 2004. **412-414**(SPEC. ISS.): p. 312-315.

197. Prozorov, T., et al., *Sonochemical modification of the superconducting properties of MgB_2.* Applied Physics Letters, 2003. **83**(10): p. 2019-2021.

198. Rui, X.F., et al., *Improved flux pinning behaviour in bulk MgB_2 achieved by nano-SiO_2 addition.* Superconductor Science and Technology, 2004. **17**(4): p. 689-691.

199. Xu, G.J., et al., *Enhancement of the irreversibility field in bulk MgB_2 by TiO_2 nanoparticle addition.* Physica C: Superconductivity and its Applications, 2004. **406**(1-2): p. 95-99.

200. Chen, S.K., et al., *Influence of in situ and ex situ ZrO_2 addition on the properties of MgB_2.* Superconductor Science and Technology, 2004. **17**(2): p. 243-248.

201. Wang, J., et al., *High critical current density and improved irreversibility field in bulk MgB_2 made by a scaleable, nanoparticle addition route.* Applied Physics Letters, 2002. **81**(11): p. 2026.

202. Qu, B., et al., *Significant improvement of critical current density in MgB_2 doped with ferromagnetic Fe_3O_4 nanoparticles.* Superconductor Science and Technology, 2009. **22**(1): p. 015027.

203. Chen, S.K., M. Wei, and J.L. MacManus-Driscoll, *Strong pinning enhancement in MgB_2 using very small Dy_2O_3 additions.* Applied Physics Letters, 2006. **88**(19): p. 192512.

204. Ma, Y., et al., *Improvement of critical current density in Fe-sheathed MgB_2 tapes by $ZrSi_2$, ZrB_2 and WSi_2 doping.* Superconductor Science and Technology, 2003. **16**(8): p. 852-856.

205. Shen, T.M., et al., *Magnetic properties and critical current density of bulk MgB_2 polycrystalline with Bi-2212 addition.* Superconductor Science and Technology, 2005. **18**(8): p. L49.

206. Yamamoto, A., et al., *High-pressure synthesis of superconducting $Nb_{1-x}B_2$ (x = 0-0.48) with the maximum T_c = 9.2 K.* Physica C: Superconductivity and its Applications, 2002. **383**(3): p. 197-206.

207. Kikuchi, A., et al., *Microstructure and J_c - B performance of powder-in-tube MgB_2 wire made by using Mg_2Cu powders with low melting point.* IEEE Transactions on Applied Superconductivity, 2005. **15**(2 PART III): p. 3207-3210.

208. Iwasa, Y., et al., *A round table discussion on MgB_2 toward a wide market or a niche production? - A summary.* IEEE Transactions on Applied Superconductivity, 2006. **16**(2): p. 1457-1464.

209. Scanlan, R.M., A.P. Malozemoff, and D.C. Larbalestier, *Superconducting materials for large scale applications.* Proceedings of the IEEE, 2004. **92**(10): p. 1639-1654.

210. Bugoslavsky, Y., et al., *Vortex dynamics in superconducting MgB_2 and prospects for applications.* Nature, 2001. **410**(6828): p. 563-565.

211. Braccini, V., et al., *High-field superconductivity in alloyed MgB_2 thin films.* Physical Review B - Condensed Matter and Materials Physics, 2005. **71**(1): p. 012504.

212. Chen, J., et al., *Enhancement of flux pinning and high-field critical current density in carbon-alloyed MgB_2 thin films.* Physical Review B - Condensed Matter and Materials Physics, 2006. **74**(17): p. 174511.

213. Rowell, J., *Magnesium diboride: Superior thin films.* Nature Materials, 2002. **1**(1): p. 5-6.

214. Brinkman, A. and J.M. Rowell, *MgB_2 tunnel junctions and SQUIDs.* Physica C: Superconductivity and its Applications, 2007. **456**(1-2): p. 188-195.

215. Ter Brake, H.J.M. and G.F.M. Wiegerinck, *Low-power cryocooler survey.* Cryogenics, 2002. **42**(11): p. 705-718.

216. Ishida, T., et al., *Superconducting MgB_2 thin film detector for neutrons.* Journal of Low Temperature Physics, 2008. **151**(3-4 PART 2): p. 1074-1079.

217. http://chem.ch.huji.ac.il/~porath/NST2/Lecture%202b.pdf.

218. Fang, H., et al., *High critical current density in iron-clad MgB_2 tapes.* Applied Physics Letters, 2003. **82**(23): p. 4113-4115.

219. Matsumoto, A., et al., *The microstructures and superconducting properties of MgB_2 tapes processed in-situ by a ball-milling method.* IEEE Transactions on Applied Superconductivity, 2005. **15**(2 PART III): p. 3333-3336.

220. Haßler, W., et al., *MgB_2 bulk and tapes prepared by mechanical alloying: Influence of the boron precursor powder.* Superconductor Science and Technology, 2006. **19**(6): p. 512-520.

221. Ribeiro, R.A., et al., *Effects of stoichiometry, purity, etching and distilling on resistance of MgB_2 pellets and wire segments.* Physica C: Superconductivity, 2002. **382**(2-3): p. 194-202.

222. Xu, X., et al., *Phase transformation and superconducting properties of MgB_2 using ball-milled low purity boron.* Journal of Applied Physics, 2008. **103**(2): p. 023912.

223. Dou, S.X., et al., *Effect of nano-particle doping on the upper critical field and flux pinning in MgB_2.* IEEE Transactions on Applied Superconductivity, 2005. **15**(2 PART III): p. 3219-3222.

224. Zhang, Y., et al., *Effect of addition of nanoparticle TiO_2/SiO_2 on the superconducting properties of MgB2.* Physica C: Superconductivity, 2008. **468**(15-20): p. 1383-1386.

225. Zhang, Y., et al., *Significant improvement of J(c) in MgB_2 bulk superconductor using ball-milled high-purity crystalline boron.* Superconductor Science & Technology, 2008. **21**(11): p. 115004.

226. Islam, A.K.M.A. and F.N. Islam, *Ab initio investigation of elastic constants of superconducting MgB_2.* Physica C: Superconductivity, 2001. **363**(3): p. 189-193.

227. Tarantini, C., et al., *Effects of neutron irradiation on polycrystalline Mg_{11} B_2.* Physical Review B - Condensed Matter and Materials Physics, 2006. **73**(13): p. 134518.

228. Jiang, J., et al., *Influence of boron powder purification on the connectivity of bulk MgB_2.* Superconductor Science and Technology, 2006. **19**(8): p. L33-L36.

229. Zhang, Y., et al., *Effects of sintering temperature on the superconductivity of MgB_2 made with high-purity crystalline B precursor.* Proceedings of the Twenty-Second International Cryogenic Engineering Conference and International Cryogenic Materials Conference, 2008. p. 977-982.

230. Eltsev, Y., et al., *Anisotropic superconducting properties of MgB_2 single crystals probed by in-plane electrical transport measurements.* Physical Review B - Condensed Matter and Materials Physics, 2002. **65**(14): p. 1405011-1405014.

231. Jiang, C.H., T. Nakane, and H. Kumakura, *Superior high-field current density in slightly Mg-deficient MgB_2 tapes.* Applied Physics Letters, 2005. **87**(25): p. 252505.

232. Perner, O., et al., *Stoichiometry dependence of superconductivity and microstructure in mechanically alloyed MgB_2.* Journal of Applied Physics, 2005. **97**(5): p. 056105.

233. Chen, S.K., et al., *Structural and superconducting property variations with nominal Mg non-stoichiometry in Mg_xB_2 and its enhancement of upper critical field.* Advanced Functional Materials, 2008. **18**(1): p. 113-120.

234. Susner, M.A., et al., *Influence of Mg/B ratio and SiC doping on microstructure and high field transport Jc in MgB_2 strands.* Physica C: Superconductivity and its Applications, 2007. **456**(1-2): p. 180-187.

235. Zeng, R., et al., *Significant improvement in the critical current density of in situ MgB_2 by excess Mg addition.* Superconductor Science & Technology, 2007. **20**(8): p. L43-L47.

236. Zhang, Y., et al., *Optimization of Nominal Mixing Ratio of Mg to B in Fabrication of Magnesium Diboride bulk.* IEEE Transactions on Applied Superconductivity, 2009. **19**: p. 2775-2779.

237. Zhang, Y., et al., *Effect of Mg/B ratio on the superconductivity of MgB_2 bulk with SiC addition.* Phys. Rev. B, 2009. **submitted**.

238. Moudden, A.H., *Ab initio study of C-substituted MgB_2.* Journal of Physics and Chemistry of Solids, 2006. **67**(1-3): p. 115-119.

239. Lee, S., et al., *Carbon-substituted MgB_2 single crystals.* Physica C: Superconductivity and its Applications, 2003. **397**(1-2): p. 7-13.

240. Kazakov, S.M., et al., *Carbon substitution in MgB_2 single crystals: Structural and superconducting properties.* Physical Review B - Condensed Matter and Materials Physics, 2005. **71**(2): p. 024533.

241. An, J.M. and W.E. Pickett, *Superconductivity of MgB_2: Covalent bonds driven metallic.* Physical Review Letters, 2001. **86**(19): p. 4366-4369.

242. Kong, Y., et al., *Electron-phonon interaction in the normal and superconducting states of MgB_2.* Physical Review B - Condensed Matter and Materials Physics, 2001. **64**(2): p. 020501.

243. Bohnen, K.P., R. Heid, and B. Renker, *Phonon dispersion and electron-phonon coupling in MgB_2 and AlB_2.* Physical Review Letters, 2001. **86**(25): p. 5771-5774.

244. McMillan, W.L., *Transition temperature of strong-coupled superconductors.* Physical Review, 1968. **167**(2): p. 331-344.

245. Masui, T., S. Lee, and S. Tajima, *Carbon-substitution effect on the electronic properties of MgB_2 single crystals.* Physical Review B - Condensed Matter and Materials Physics, 2004. **70**(2): p. 024504.

246. Di Castro, D., et al., *Raman spectra of neutron-irradiated and Al-doped MgB_2.* Physical Review B - Condensed Matter and Materials Physics, 2006. **74**(10): p. 100505.

247. Allen, P.B. and R.C. Dynes, *Transition temperature of strong-coupled superconductors reanalyzed.* Physical Review B, 1975. **12**(3): p. 905-922.

248. Brinkman, A., et al., *Multiband model for tunneling in MgB_2 junctions.* Physical Review B - Condensed Matter and Materials Physics, 2002. **65**(18): p. 1805171-1805174.

249. Wilke, R.H.T., et al., *Systematic effects of carbon doping on the superconducting properties of $Mg(B_{1-x}C_x)_2$.* Physical Review Letters, 2004. **92**(21): p. 217003-1.

250. Zhang, Y., et al., *Effect of sucrose ($C_{12}H_{22}O_{11}$) doping on the critical current density of MgB_2.* IEEE Transactions on Applied Superconductivity, 2007. **17**(2): p. 2933-2936.

251. Katsura, Y., et al., *Improved critical current properties of MgB_2 bulks by controlling microstructures.* Journal of Physics: Conference Series, 2006. **43**(1): p. 119-122.

252. Zhang, Y., et al., *The effect of carbon doping on the upper critical field (H_{c2}) and resistivity of MgB_2 by using sucrose ($C_{12}H_{22}O_{11}$) as the carbon source.* Superconductor Science and Technology, 2009. **22**(1): p. 015025.

253. Yeoh, W.K. and S.X. Dou, *Enhancement of H_{c2} and Jc by carbon-based chemical doping.* Physica C: Superconductivity and its Applications, 2007. **456**(1-2): p. 170-179.

254. Yan, S.C., et al., *The upper critical field in micro-SiC doped MgB_2 fabricated by a two-step reaction method.* Superconductor Science and Technology, 2007. **20**(6): p. 549-553.

255. Perner, O., et al., *Effects of oxide particle addition on superconductivity in nanocrystalline MgB_2 bulk samples.* Physica C: Superconductivity and its Applications, 2005. **432**(1-2): p. 15-24.

256. Zhang, Y., et al., *Effect of addition of TiO2/SiO2 nano-particles on H_{c2} and Hirr in MgB_2 bulks.* Proceedings of the 2008 International Conference on Nanoscience and Nanotechnology, 2008. **art. no. 4639255**: p. 97-100

257. Liao, X.Z., et al., *Controlling flux pinning precipitates during MgB_2 synthesis.* Applied Physics Letters, 2002. **80**(23): p. 4398.

258. Liao, X.Z., et al., *Mg(B,O)2 precipitation in MgB_2.* Journal of Applied Physics, 2003. **93**(10 1): p. 6208-6215.

259. Eom, C.B., et al., *High critical current density and enhanced irreversibility field in superconducting MgB_2 thin films.* Nature, 2001. **411**(6837): p. 558-560.

260. Yates, K.A., et al., *The effect of oxygenation on the superconducting properties of MgB_2 thin films.* Applied Physics Letters, 2005. **86**(2): p. 022502.

261. Singh, R.K., et al., *Effect of stoichiometry on oxygen incorporation in MgB_2 thin films.* Superconductor Science and Technology, 2008. **21**(1): p. 015018.

262. Singh, R.K., et al., *Effect of oxygen incorporation on normal and superconducting properties of MgB_2 films.* Applied Physics Letters, 2008. **93**(24): p. 242504.

263. Senkowicz, B.J., et al., *Atmospheric conditions and their effect on ball-milled magnesium diboride.* Superconductor Science and Technology, 2006. **19**(11): p. 1173-1177.

264. Takada, J., et al., D*etermination of diffusion coeffficient of oxygen in gamma - iron from measurements of internal oxidation in fe-al alloys.* Metallurgical transactions. A, Physical metallurgy and materials science, 1986. **17 A**(2): p. 221-229.

265. Wang, X.L., et al., *Significant enhancement of critical current density and flux pinning in MgB_2 with nano-SiC, Si, and C doping.* Physica C: Superconductivity and its Applications, 2004. **408-410**(1-4): p. 63-67.

266. Wang, X.L., et al., *Very fast formation of superconducting MgB_2/Fe wires with high J_c.* Physica C: Superconductivity and its Applications, 2001. **361**(3): p. 149-155.

267. Klie, R.F., et al., *Observation of coherent oxide precipitates in polycrystalline MgB_2.* Applied Physics Letters, 2002. **80**(21): p. 3970.

268. Zhang, Y., et al., *Influence of heat treatment on the superconductivity of MgB_2 bulk sintered in flowing welding grade Ar atmosphere.* IEEE Trans. Magn., 2009. **45**: p.2626-2629.

Publications

1. ***Y. Zhang***, S. H. Zhou, C. Lu, K. Konstantinov and S. X. Dou, "Effect of carbon doping on the H_{c2} and resistivity of MgB_2 by using sucrose ($C_{12}H_{22}O_{11}$) as the carbon source," Supercond. Sci. Technol., Vol. 22, p. 015025, 2009.

2. ***Y. Zhang***, C. Lu, S. H. Zhou, K. C. Chung, Y. K. Kim and S. X. Dou, "Influence of heat treatment on the superconductivity of MgB_2 bulk sintered in flowing welding grade Ar atmosphere," IEEE Trans. Magn., Vol. 45, p. 2626, 2009.

3. ***Y. Zhang*,** C. Lu, S. H. Zhou, and J. B. Joo, "Influence of nanocrystalline boron precursor powder on superconductivity in MgB_2 bulk," *J. Nanosci. Nanotechnol.*, Vol. 9, p. 7402, 2009.

4. ***Y. Zhang*,** C. Lu, S. H. Zhou, K. K. Chung, and W. X. Li, "Optimization of Nominal Mixing Ratio of Mg to B in Fabrication of Magnesium Diboride bulk," IEEE Trans. Appl. Supercond., Vol. 19, p. 2775, 2009**.**

5. ***Y. Zhang***, S. H. Zhou, C. Lu, K. C. Chung and S. X. Dou, "Effect of sintering time on the superconductivity in MgB_2," Int. J. Mod. Phys. B, Vol. 23, p. 3476, 2009.

6. ***Y. Zhang***, S. H. Zhou, W. X. Li, X. L. Wang, and S. X. Dou, "High critical current density of MgB_2 bulks sintered in flowing welding grade Ar atmosphere," Int. J. Mod. Phys. B, Vol. 23, p. 3538, 2009.

7. ***Y. Zhang*,** S. H. Zhou, Y. Zhao, C. Lu, K. K. Chung, Y. K. Kim, J. M. Yoo, "Effects of sintering temperature on the superconductivity of MgB_2 made with high-purity crystalline B precursor," Proceedings of the Twenty-Second International Cryogenic

Engineering Conference and International Cryogenic Materials Conference 2008, p.977, 2008.

8. ***Y. Zhang***, S. Soltanian, Y. Zhao, S. H. Zhou, X. L. Wang, S. X. Dou "Effect of addition of TiO_2/SiO_2 nano-particles on H_{c2} and H_{irr} in MgB_2 bulks,**"** Proceedings of the 2008 International Conference on Nanoscience and Nanotechnology, International Conference On Nanoscience and Nanotechnology (ICONN 2008), Melbourne, Victoria, Australia (Feb. 2008), p. 97, 2008.

9. ***Y. Zhang***, X. Xu, Y. Zhao, J. H. Kim, C. Lu, S. H. Zhou and S. X. Dou, "Significant improvement of J_c in MgB_2 bulk superconductor using ball-milled high purity crystalline boron," Supercond. Sci. Technol., Vol. 21, p. 115004, 2008.

10. ***Y. Zhang***, S. H. Zhou, X. L. Wang and S. X. Dou "Effect of addition of nanoparticle TiO_2/SiO_2 on the superconducting properties of MgB_2," Physica C, Vol. 468, p.1383, 2008.

11. ***Y. Zhang***, S. H. Zhou, A. V. Pan, and S. X. Dou "Effect of sucrose ($C_{12}H_{22}O_{11}$) Doping on the critical current density of MgB_2," IEEE Trans. Appl. Supercond., Vol. 17, No. 2, p. 2933, 2007**.**

12. S. H. Zhou, ***Y. Zhang***, A. Pan, S. H. Dou, K. K. Chung, J. M. Yoo, "Preparing MgB_2 with excessive Mg environment sintering and two-step sintering approach," IEEE Trans. Appl. Supercond., Vol. 19, p. 2748, 2009.

13. S. H. Zhou, ***Y. Zhang***, A. Pan, S. X. Dou, K. Chung, J. Yoo, "Effects of sintering atmosphere on the superconductivity of MgB_2," Supercond. Sci. Technol., Vol. 22, p. 045018, 2009.

14. W. X. Li, Y. Li, R. H. Chen, R. Zeng, L. Lu, ***Y. Zhang***, M. Tomsic, M. Rindfleisch, and S. X. Dou "Increased superconductivity for CNT doped MgB_2 sintered in 5T pulsed magnetic field," IEEE Trans. Appl. Supercond., Vol. 19, p. 2752, 2009.

15. W. X. Li, R. Zeng, L. Lu, ***Y. Zhang***, S.X. Dou, Y. Li, R.H. Chen, M.Y. Zhu, "Improved superconducting properties of in situ powder-in-tube processed $Mg_{1.15}B_2$/Fe wires with nano size SiC addition," Physica C, Vol. 469, p. 1519, 2009.

16. W. X. Li, Y. Li, R. H. Chen, M. Y. Zhu, H. M. Jin, R. Zeng, L. Lu, ***Y. Zhang*** and S. X. Dou, "T_c enhancement for nano-SiC doped Mgb_2 superconductors sintered in 5T pulsed magnetic field," Int. J. Mod. Phys. B, Vol. 23, p. 3482, 2009.

17. X. Xu, J, H, Kim, ***Y. Zhang***, E. Babic, "Critical current density performance of malic acid doped magnesium diboride wires at different operating temperatures," Int. J. Mod. Phys. B, Vol. 23, p. 3497, 2009.

18. X. Xu, J. H. Kim, ***Y. Zhang***, Y. Zhao, M. Rindfleisch, and M. Tomsic, "Superconducting Properties of MgB_2 Wire Using Ball-milled Low Purity Boron," IEEE Trans. Appl. Supercond., Vol. 19, p. 2714, 2009.

19. S. Zhou, A. V. Pan, ***Y. Zhang*****,** and S. X. Dou, *"*Effects of sintering atmosphere on the superconducting properties of SiC doped bulk MgB_2 superconductor," Journal of Physics: Conference Series 97 (1), 012081, 2008.

20. X. Xu, J. H. Kim, W. K. Yeoh, ***Y. Zhang*** and S. X. Dou "Improved J_c of MgB_2 superconductor by ball milling using different media," Supercond. Sci. Technol., Vol. 19, p. L47, 2006**.**

21. S. X. Dou**,** S. Soltanian, W. K. Yeoh, and ***Y. Zhang*** "Effect of Nano-Particle Doping on the Upper Critical Field and Flux Pinning in MgB_2," IEEE Trans. Appl. Supercond., Vol. 15, No. 2, p. 3219, 2005.